

## Graphene: a two type charge carrier system

*Magdalena Wojtaszek*  
(Master Thesis)



**rijksuniversiteit  
groningen**

**Research group:** Physics of Nanodevices  
**Group Leader :** Prof. Dr. Ir. Bart J. van Wees  
**Supervisor:** Msc. Alina Veligura  
**Referent:** Dr. Harry Jonkman



# Contents

<b>Contents</b>	<b>i</b>
<b>1 Introduction: electronic transport in graphene</b>	<b>1</b>
1.1 The electronic band structure . . . . .	1
1.2 Transport measurements in graphene . . . . .	3
1.2.1 Finite minimum conductivity . . . . .	6
1.3 Graphene corrugations - broadening of the Dirac point . . . . .	7
1.4 Formation of hole-electron puddles . . . . .	10
1.5 Short range and long range scattering mechanisms in graphene . . . . .	11
1.6 Initial molecular doping . . . . .	14
1.7 Hall effect: determination of charge carrier concentration . . . . .	16
1.8 Positive magnetoresistance in graphene . . . . .	17
1.8.1 Classical origins of magnetoresistance . . . . .	18
1.8.2 Magnetoresistance due to quantum localisation effects . . . . .	19
<b>2 Transport in one vs two charge carrier system. Magnetoresistance.</b>	<b>23</b>
2.1 Carriers in ideal graphene at room temperature. . . . .	23
2.2 Carriers in graphene with electron and hole puddles. . . . .	26
2.3 Resistivity in one vs two charge type carrier system. Magnetoresistance.	29
2.4 Resistivity in ideal graphene and graphene with puddles. . . . .	32
<b>3 Device preparation and measurement setup</b>	<b>39</b>
3.1 Deposition of Kish graphite . . . . .	39
3.2 Preparation of the device . . . . .	41

3.2.1	Deposition of gold contacts . . . . .	42
3.2.2	Shaping graphene: oxygen plasma etching. . . . .	45
3.3	Measurement setup . . . . .	48
<b>4</b>	<b>Experimental part</b>	<b>53</b>
4.1	The influence of device preparation on contact resistance . . . . .	53
4.2	Electrical characterisation of the device - Dirac curve. . . . .	54
4.2.1	Tracing the charge neutrality point . . . . .	55
4.2.2	Influence of magnetic field on the graphene resistivities . . . . .	58
4.2.3	Hall effect measurements . . . . .	58
4.2.4	Dirac curve under different magnetic fields . . . . .	61
4.3	Relation between obtained experimental results and proposed theoretical model. . . . .	62
4.3.1	Comparison of the measurements with the model for the non-etched device D2 . . . . .	63
4.3.2	Comparison of the measurements with the model for the etched device C5 . . . . .	66
<b>5</b>	<b>Conclusions</b>	<b>69</b>
	<b>Bibliography</b>	<b>73</b>

# Abstract

Graphene as a 2 dimensional material with an unique conical band structure and high carrier velocities holds enormous potential for nanoelectronics. Understanding the electronic band structure of graphene and its relation to the electronic transport properties is the starting point for optimising the performance of graphene devices and their technological application. The description of electronic transport in graphene, widely used by the graphene research community, is based on semiclassical Drude model. This model treats graphene like a system with a single type of carriers: holes or electrons, depending on the position of the Fermi level. It well describes the measurements at high charge carrier concentrations ( $n \gtrsim 10^{12} \text{cm}^{-2}$ ), in the so called *metallic regime*. However it does not explain the experimental observations in the vicinity of charge neutrality point, particularly: the finite maximum of longitudinal resistance  $\rho_{xx}$  and the zero transversal resistance  $\rho_{xy}$  at charge neutrality point and also the magnetoresistance of graphene. In this master thesis I propose the extension of the Drude model for the system with two types of charge carriers. Within the semiclassical framework I describe the graphene's carrier density in the vicinity of charge neutrality point, taking into account thermal equilibrium at room temperature and fluctuations of the electric potential. I explain the origin of these potential variations and their influence on the modelled resistivities of graphene. The important part of these thesis is the comparison of the predictions from the model with the experimental observations. For that purpose I fabricated graphene devices and measured electronic transport with and without magnetic field. In the final part I show that although the proposed model is very simple, it reproduces well the measurements and can serve as a tool for sample characterisation.



## Introduction: electronic transport in graphene

Graphene, a monolayer of carbon atoms, is a truly 2-dimensional structure stable under ambient conditions. It was firstly obtained by micromechanical cleavage of graphite in 2004 [1] and, since then activated an enormous research interest as it showed outstanding mechanical, structural and electronic properties. The most important graphene properties originates from its very unusual electronic structure. While in standard conductors charge carriers are described by quantum mechanics as the electron waves obeying the Schrödinger effective-mass equation, graphene electrons move according to the laws of relativistic quantum physics - the mass-free Dirac equation. In the following chapter I present the electronic band structure and its relation to the extraordinary electronic transport features in graphene. Later on I describe the scattering mechanisms and the influence of environment, like presence of substrate or adsorption of molecules, on electronic performance of graphene devices. The detailed understanding of the influence from surrounding is crucial in characterisation of the initial state of the device, to which the experimental part of this thesis is dedicated.

### 1.1 The electronic band structure

Graphene is a planar sheet of carbon atoms arranged in hexagonal rings, which form a honey-comb lattice (see Fig. 1.1). One can also describe it as a system of connected benzene rings stripped out from their hydrogen atoms. In terms of Molecular Orbital Theory its atomic structure is characterised by two types of C-C bonds ( $\sigma$ ,  $\pi$ ), constructed from the four valence orbitals of carbon atom ( $2s, 2p_x, 2p_y, 2p_z$ ), where a  $z$  direction is perpendicular to the sheet of graphene. Each carbon atom bonds to the 3 carbon neighbours via in-plane  $\sigma$ -bonds formed from  $sp^2$  hybridized orbitals (orbitals formed from one  $s$ -orbital and two  $p$ -orbitals), while the fourth, remaining  $p_z$ -orbital give rise to a highly delocalised  $\pi$ -orbital and its electron is free to move. The bonding  $\pi$ - and antibonding  $\pi^*$ -orbitals form the wide electronic valence and conduction bands.

Graphene has two identical carbon atoms in each unit cell and thus two equivalent atom sublattices: A and B (indicated by different colours in Fig. 1.1). This gives rise to an extra degree of freedom, pseudospin, absent in conventional two-dimensional (2D) systems, and leads to the exceptional electronic properties [2]. Electrons in graphene have to be described by the relativistic Dirac equation and

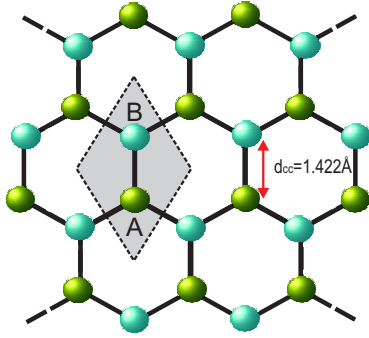


**Figure 1.1:** A hexagonal lattice of graphene. Different colours of carbon atoms indicate the two identical sublattices, labeled A and B. The grey area marks an unit cell,  $d_{C-C}$  describes the distance between neighbouring carbons.

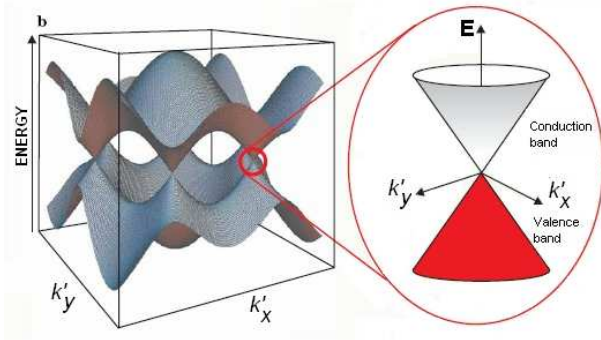


**Figure 1.2:** The band structure of graphene. The zoomed region present the linear shape of conduction and valence band connected through the Dirac point.

their wave function poses additional phase shift of  $\pi$ , known as Berry's phase [3]. The projection of the pseudospin on the direction of the momentum defines the chirality of the electron. As a consequence of the high lattice symmetry the band structure for graphene at low energies has the linear conical shape (Fig. 1.2). This is a remarkable difference from the usual parabolic energy-momentum relation in conventional semiconductors. In graphene the conduction and valence band touch each other in one point at 6 corners of the two-dimensional hexagonal Brillouin zone and create the zero band gap. Due to symmetry only two out of six points,  $(k, k')$ , are essentially different, while the rest four are equivalent to them. This leads to the so called *valley degeneracy*. The residual point, where the conduction and the valence band touches, is called the Dirac point.

The dispersion relation  $E(\mathbf{k})$  in the vicinity of Dirac points  $(k, k')$  fulfil the following equation:

$$E(\mathbf{k}) = \pm \hbar v_F \sqrt{k_x^2 + k_y^2}. \quad (1.1)$$

where a + sign corresponds to the conduction band and a - sign to the valence band. The group velocity around the Dirac point (the Fermi velocity) is  $v_F = 1 \times 10^6 m/s$ . The described conical electronic band-structure has a direct correspondence to the electronic transport measurements, which are described in the following sections.

## 1.2 Transport measurements in graphene

The standard way to modify electronic properties of a material is by exploring the electric field effect. There, by applying an external voltage, one can vary the carrier concentration in the material and therefore its resistance. The basic graphene device resembles a field-effect transistor (FET) and is schematically drawn in Fig. 1.3(a). In it graphene is deposited on a silicon dioxide ( $\text{SiO}_2$ ) layer, with a heavily doped silicon substrate and then a gate electrode (back-gate) beneath. Applying a gate voltage creates the potential drop across the  $\text{SiO}_2$  insulating layer. Like in the case of capacitor the gate voltage induces the surface charge density, according to the equation:

$$n = \frac{\epsilon_0 \epsilon_r V_g}{te} = \alpha V_g \quad (1.2)$$

where  $\epsilon_0$  is the permittivity of free space ( $\epsilon_0 \cong 8.854 \times 10^{-12} \text{ F/m}$ ),  $\epsilon_r$  is the relative permittivity of  $\text{SiO}_2$  (the literature value is  $\epsilon_r = 3.9$ ),  $t$  is the thickness of  $\text{SiO}_2$  layer (in our case  $t = 300 \text{ nm}$ ) and  $e$  is the electron charge ( $e \cong 1.602 \times 10^{-19} \text{ C}$ ). After substituting the values we find the proportionality coefficient  $\alpha$  between induced charge carriers and the applied gate voltage:  $\alpha \cong 7.2 \times 10^{10} \text{ cm}^{-2} \text{ V}^{-1}$ . Additionally, the Fig. 1.3(a) presents the scheme for two types of resistivity measurements: one, when we measure the voltage drop between parallel contacts,  $V_{xx}$ , to determine the longitudinal resistivity  $\rho_{xx}$  (also referred as a graphene resistivity), the other one, when we measure voltage drop between opposite contacts,  $V_{xy}$ , to determine the transversal resistivity  $\rho_{xy}$  (also referred as Hall resistivity) at non-zero magnetic field. The thick black arrows mark how the current is sent while the bottom electrode (back-gate) is connected to the voltage source so that both resistivities can be measured as a function of gate voltage.

With changing the gate voltage we modify the charge carrier density in the graphene (graphene acts as a second parallel plate of capacitor) and therefore we can tune its Fermi level. In neutral graphene the Fermi level lays at the Dirac point. Because it is a single point in the band structure, it generates zero density of states. This means that there are no states to occupy and hence there are no carriers, which could contribute to the electronic transport (at the Dirac point carrier concentration vanishes,  $n = 0$ ). As a result, for the Fermi level at the Dirac point graphene exhibit a large resistivity ( $\sim 6k\Omega$ ). The Dirac point separates the region of conduction by electrons (when the Fermi level lies within the conduction band) from the region where transport is governed by holes (when Fermi level lies within the valence band). When, with the back-gate voltage, we shift the Fermi level away from the Dirac point (into hole or electron conduction regime) the resistance decreases with the increase of gate voltage. This is related to the increase of carrier concentration, which contributes to the transport. The described behaviour of the graphene resistance at different gate voltages and its schematic relation to the position of Fermi level in the band structure is presented in Fig. 1.3(b).

The Dirac voltage  $V_{Dirac}$  is identified as a gate voltage for which the maximum

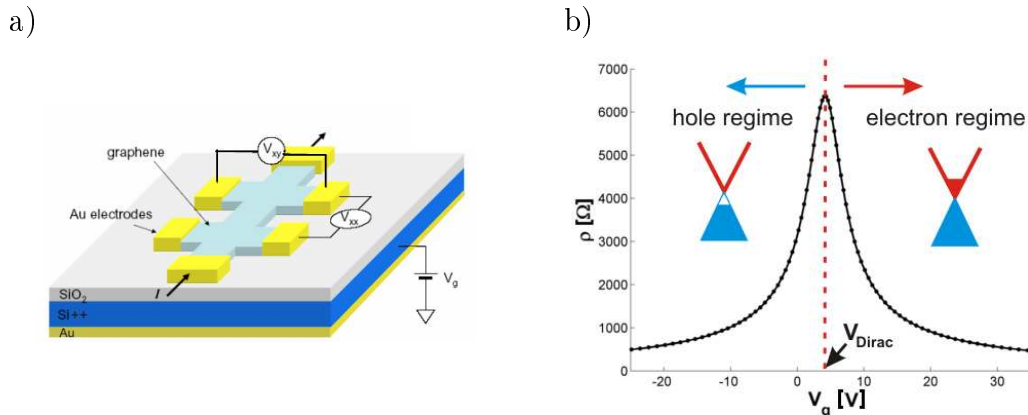


**Figure 1.3:** Structure and geometry of basic graphene device (a). The thick black arrows mark the current path, while the connections between the contacts  $V_{xx}$  and  $V_{xy}$  indicate measuring scheme for longitudinal resistivity  $\rho_{xx}$  and transversal resistivity  $\rho_{xy}$  (also referred as Hall resistivity) respectively. In (b) a typical graphene resistivity  $\rho_{xx}$  dependence as a function of gate voltage  $V_g$  is presented. Maximum of resistivity occurs when Fermi level lies at the Dirac point, for which in principle charge carrier concentration  $n = 0$ . Away from the Dirac point  $\rho_{xx}$  decreases rapidly, as  $|V_g - V_{Dirac}|$  increases.

of longitudinal resistivity  $\rho_{xx}$  occurs. In neutral graphene  $V_{Dirac} = 0$  V, but for doped graphene it is shifted from the zero voltage, depending on the doping level. Dopants shift the Fermi level out from the Dirac neutrality point and hence the maximum of the resistance occurs not at  $V_g = 0$  V, but at the gate voltage which compensates the charges of dopants. In neutral graphene the charge carrier density at various gate voltages can be calculated from Eq. 1.2, however for doped graphene we have to take into account that the charge carrier density induced by the gate voltage is different from the actual charge carrier density in graphene. The equation Eq. 1.2 needs to be shifted by the voltage corresponding to the charge of dopants already present in graphene. Here, the Dirac voltage  $V_{Dirac}$  serves as an offset value. In doped graphene the charge carrier density as a function of gate voltage can be obtained from the relation:

$$n = \alpha(V_g - V_{Dirac}) \quad (1.3)$$

The symmetrical shape of the energy dispersion relation  $E(k)$  for the conduction and valence band implies equal group velocities for electrons and for holes  $v_F$ . In ideal graphene (no defects or impurities) or in graphene with isotropic scattering (e.g. white-noise disorder or phonons), when scattering mechanisms affect the carriers (electrons or holes) with the same strength, no matter of their charge sign, the drift velocity of carriers  $v_{drift}$  (the average velocity that a carrier attains due to an electric field,  $v_{drift} = \mu_i E$ ) is the same for electrons and for holes. As a consequence the electron mobility  $\mu_e$  is equal to the hole mobility  $\mu_h$ .

This can be directly verified experimentally by measuring the electrical condu-

ctivity (which is the inverse of the electrical resistivity  $\sigma = 1/\rho$ ) as a function of gate voltage.

$$\sigma(V_g) = n_i(V_g)e\mu_i \quad (1.4)$$

where  $n_i(V_g)$  is the concentration of carriers of type  $i$  ( $i = \textit{electrons}, \textit{holes}$ ), calculated from Eq. 1.3. An example of conductivity measurements is presented in Fig. 1.4). There, away from the Dirac point we can see a linear dependence of the conductivity from the gate voltage. The slope of the linear fit for holes ( $\alpha$ ) and for electrons ( $\beta$ ) is different, here  $|\textit{ctg}(\beta)/\textit{ctg}(\alpha)| \cong 0.6$ . The ratio between mobilities of electrons and holes is not universal and depends on the quality of graphene. Reported values scatter between  $0.5 \div 1$ , see [23].

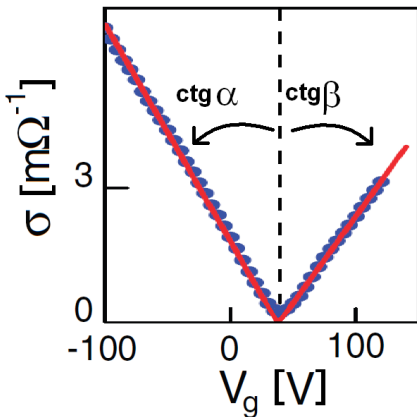


**Figure 1.4:** Graphene conductivity measured as a function of gate voltage. The red lines represent the linear fit of the conductivity in the hole and in the electron conduction regime. The observed difference in the slope of the linear fits indicates that in this sample  $\mu_e \neq \mu_h$ . Adapted from [1].

Mobility reflects the strength of scattering mechanisms, which includes the intrinsic scattering (like scattering on phonons) and extrinsic (scattering on defects, impurities or adsorbates). The last one is directly related to the sample purity and can be increased with technological improvement. Mobility is determined from the electrical measurements of resistivity in the high carrier density regime (so called metallic regime), where induced charges don't change the resistivity essentially, according to the formula:

$$\mu_i = \frac{1}{en_i\rho} \quad (1.5)$$

where  $i = \textit{electrons}, \textit{holes}$ , as before.

The values of the reported mobilities in graphene at room temperature show large scattering (from 1000 up to 70 000  $cm^2/Vs$ , when deposited on  $SiO_2$  [4], and exceed 200 000  $cm^2/Vs$  for suspended graphene [5]). This value is higher compared to the value of mobility for the fastest present inorganic semiconductors (InSb, 78 000  $cm^2/Vs$  [6]) or semiconducting carbon nanotubes ( $1 \cdot 10^5 cm^2/Vs$ , [7]). As the high mobility of carriers is a desired property in electronic technology, naturally comes the questions about the factors limiting its value: scattering mechanisms, intrinsic limits and about the reason for large scattering in the values of the obtained mobilities. Scattering on phonons, which is inevitably present at finite temperature measurements, in graphene is extremely weak and mobilities higher than

200 000  $cm^2/Vs$  are predicted, when the extrinsic disorder is eliminated [8]. It was confirmed experimentally for suspended graphene [5] .

### 1.2.1 Finite minimum conductivity

Despite the zero carrier density at the Dirac point, graphene exhibits a finite minimum conductivity. This is counterintuitive, as conductivity is expected to vanish when the Fermi energy ( $E_F$ ) approaches the Dirac point. Theoretical analysis however proved that the finite conductivity is a characteristic property of Dirac chiral fermions in two dimensional systems. In the limit of zero temperature, at zero charge carrier density and without any scattering the conductivity is predicted to be of the order of  $e^2/h$  [9] (the units conversion is:  $h/e^2 = 25.8k\Omega$ ). Most theories suggest that  $\sigma_{min} = 4e^2/h\pi$ , which is about  $\pi$  times smaller than the typical values observed experimentally. The experimental values are presented in Fig. 1.5 and most of the data cluster around  $\sigma_{min} = 4e^2/h$ .

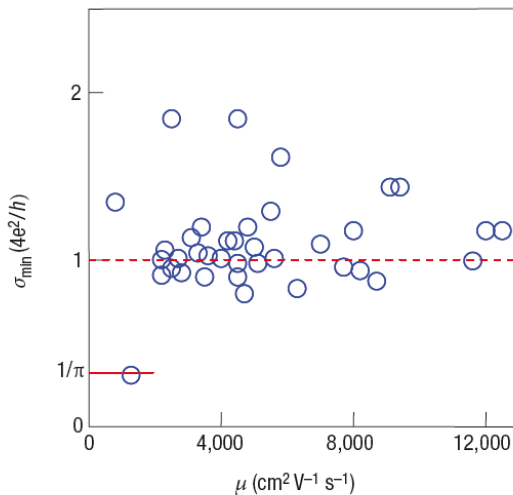


**Figure 1.5:** Minimum conductivity of graphene for different samples at low temperatures. All presented graphene devices exhibit approximately the same conductivity at the neutrality point (open circles) with most data clustering around  $4e^2/h$ . Adapted from [10].

This discrepancy can be understood when we realise that the nominally undoped and ungated graphene device with the Dirac point as a single point, is an idealised description, sometimes called *intrinsic* graphene. This *intrinsic* graphene, with no free carriers at Dirac point is an abstract model, because the slightest amount of the structural disorder, doping or external potential fluctuations will induce carriers in the system. In fact, in all experiments we study so called *extrinsic graphene*, where there is no point of vanishing charge carrier density ( $n=0$ ). Instead, minimum conductivity occurs at charge neutrality point (the point where the density of induced electrons in the conduction band is equal to the density of induced holes in the valence band), abbreviated later to CNP.

The carriers at minimum conductivity point can be induced by several mechanisms:

1. by structural corrugations (non-flatness), which shift locally the position of the Dirac point across the graphene sheet;
2. by the presence of charge impurities, which modify locally chemical potential (electron-hole puddles);
3. by molecular doping (exposing the system to charge transferring molecules);
4. by applying an external gate voltage  $V_g$ ;
5. by thermal fluctuations (highly reduced at few Kelvin measurements);
6. by other disorder effects (crystal defects etc.);

A brief analysis of these mechanisms will be presented in the following sections.

### 1.3 Graphene corrugations - broadening of the Dirac point

From the theoretical point of view, graphene appears to be a strictly two-dimensional (2D) material. On the other hand, according to predictions from thermodynamics, perfect two-dimensional crystals are unstable and cannot exist in the free state. Thermal fluctuations in their crystal lattices should lead to the atom displacements, which are comparable to the interatomic distances at any finite temperature. The crystal cannot keep its crystalline long-range order and hence will segregate into islands or decompose ([11], [12]). Although the theory does not allow perfect crystals in 2D space to exist, it does not forbid that for nearly perfect 2D crystals in three-dimensional (3D) space [13]. The *rippling* of the 2D structure, as one of the ways to extend 2-dimensionality, may neutralise the thermal and quantum fluctuations on which it is exposed. The stability of graphene single layer, when deposited on a substrate, is explained through the presence of a larger three-dimensional bulk structure beneath. There, a graphene film accommodates to the substrate by conforming its roughness, what produces microscopic corrugations (ripples) [14].

Fig. 1.6 presents height histograms of graphene on  $\text{SiO}_2$  substrate and of a pure  $\text{SiO}_2$ . The graphene sheet is approximately 40% smoother than the oxide surface. This stems from the fact that the graphene sheet does have a finite intrinsic stiffness, which prevents it from conforming completely the morphology of the substrate (closely following the sharp orientation changes of the  $\text{SiO}_2$  costs graphene more energy) [15]. From above argument it is also clear, why bilayer graphene deposited

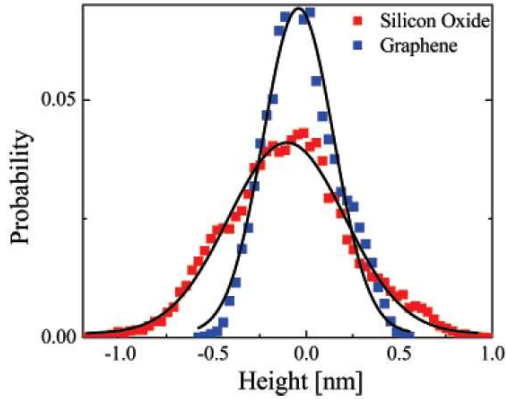


**Figure 1.6:** Height histograms acquired for graphene on  $\text{SiO}_2$  and for bare  $\text{SiO}_2$  (blue and red squares, respectively). The histograms are well-described by the Gaussian distributions (black lines) with standard deviations of 1.9 and 3.1 Å for graphene on  $\text{SiO}_2$  and for bare  $\text{SiO}_2$ , respectively. Adapted from [15].

on a substrate shows less corrugations than a single layered. The upper graphene layer has to conform to the second carbon layer beneath, which is much smoother than  $\text{SiO}_2$ . Similar argument holds for graphite, where due to 3-dimensional nature of the crystal, no stabilizing ripples are necessary.

It turns out however that graphene is stable enough to exist also without a substrate. This occurs in so called suspended graphene (graphene freely hanging in air, supported by a microfabricated metallic scaffold). There graphene extends its 2 dimensional nature by undergoing some internal rippling. The schematic drawing of the graphene structure of the ideally flat sheet and of the sheet with rippling is presented in Fig. 1.7(a) and (b). The presence of corrugations in the third dimension was confirmed by transmission electron microscopy (TEM), where it was found that the surface normal varies by several degrees and that out-of-plane deformations reach 1 nm [16].

This 3D morphology of the graphene sheet is important for transport properties. When the angle between orbitals varies, also the overlap between orbitals changes locally. The reciprocal space for corrugated sheet has slightly different relative orientations depending on the morphology (see Fig. 1.7(c) and (d)). As a result, the position of the Dirac point is not arbitrary for the whole graphene sheet. This, on average, causes the broadening of the density of states, so that the Dirac point is no longer a single point. It also implies that even if the Fermi level crosses the Dirac point at one particular region of graphene, it will lay above or below the Dirac point for regions where its position is slightly different due to rippling and will produce states available for carriers.

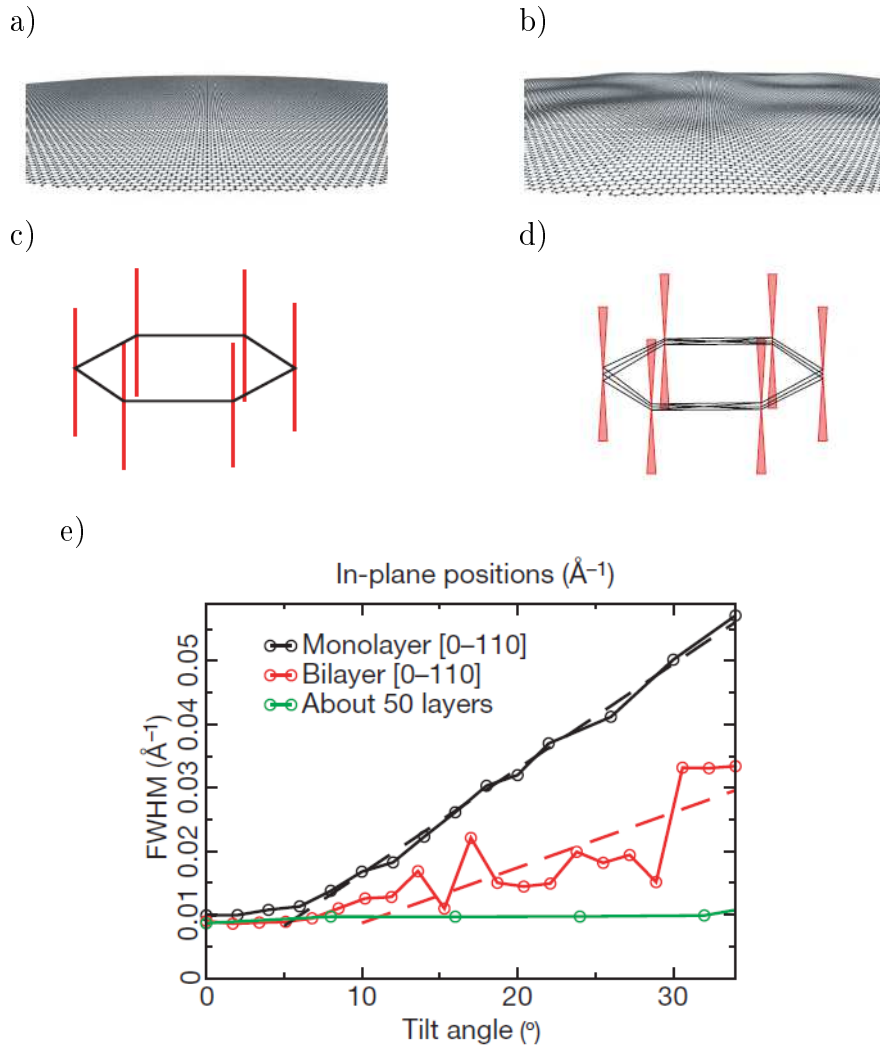


**Figure 1.7:** Microscopically corrugated graphene. An ideally flat graphene crystal in a real space (a) (a perspective view). Corrugations in suspended graphene (b) (displayed roughness imitates quantitatively the roughness found experimentally). The reciprocal space for a flat sheet (c) is a set of rods (red) directed perpendicular to the reciprocal lattice of graphene (black hexagon). The reciprocal space for the corrugated sheet (d) consists of a set of rods perpendicular to the plane of the reciprocal hexagonal lattice. A superposition of the diffracting beams from locally flat areas effectively turns the rods into cone-shaped volumes. As a result, the diffraction spots become broader with an increase of the tilt angle and with an increase of the distance from the tilt axis. From a theoretical point of view, this broadening is completely unexpected, revealing that graphene sheets are not flat within the submicrometre area of the electron beam. This broadening could be described by full widths at half maxima (FWHM) of spot-intensity and measure as a function of the tilt angle for monolayer, bilayer and graphite. The measured broadening is notably weaker in bilayer samples (also suspended) and completely disappears for multilayer graphene (included as a reference). Adapted from [16].

## 1.4 Formation of hole-electron puddles

Structural corrugations in graphene is not the only factor which changes locally the relative position of the Dirac point with respect to the Fermi level across graphene and gives rise to the finite carrier density ( $n \neq 0$ ). Even more significant is the shift of the Fermi level due to chemical potential variations induced by charged impurities above and below the graphene layer. The silicon dioxide  $\text{SiO}_2$ , so far the only used substrate for graphene devices, due to the possibility to identify single layer graphene flakes basing on the difference in optical contrast [17], has a surface roughness 0.3nm and about  $50 \times 10^{12} \text{ cm}^{-2}$  ionised impurities. Charge impurities as well as described later charge transferring adsorbates, modify electrostatic potential and lead to the local shift of the Fermi level. As a result the electrostatic gating does not occur homogeneously within the graphene sheet and at charge neutrality point (the Dirac voltage) the system splits into hole-rich and electron-rich puddles. The presence of puddles was confirmed with the use of scannable single-electron transistor (SET) at 0.3 K, [18], which allowed to map the local density of states and the carrier density landscape in the vicinity of the charge neutrality point (CNP).

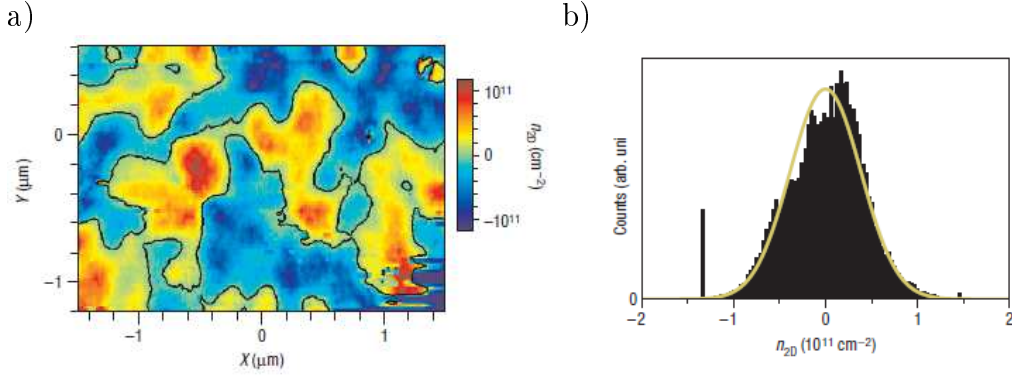


**Figure 1.8:** Spatial density fluctuations and electron/hole puddles at Dirac neutrality point. (a) Colour map of the spatial density variations in the graphene flake extracted from surface potential measurements. The blue regions correspond to hole-rich and the red regions to electron-rich puddles. The black contour marks the zero density contour. (b) presents histogram of the density distribution of (a). From the fit of the gaussian distribution, the density fluctuations are of the order of  $\Delta n_{2D, T=0.3K} = \pm 3.9 \times 10^{10} \text{ cm}^{-2}$ . Adapted from [18].

The 2D map of the carrier density of graphene deposited on  $\text{SiO}_2$  at CNP is shown on Fig. 1.8. We can see there regions with excessive number of holes (blue) and regions with excessive number of electrons (red) of the size up to few hundreds of nanometres, non-homogeneously distributed in graphene sheet. Scan of potential variation of the bare  $\text{SiO}_2$ , in Fig. 1.9, exhibit non-homogeneous potential fluctuations similar in size to the size of puddles. This confirms that charge impurities in  $\text{SiO}_2$  affects the carrier density in graphene and induce carriers at

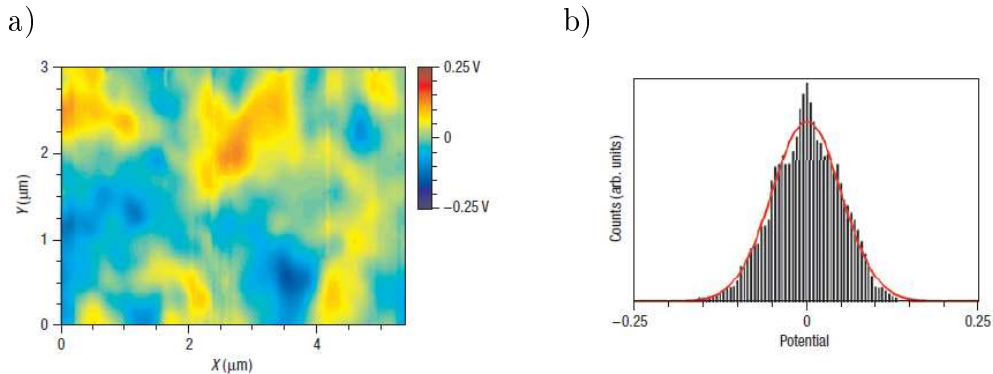


**Figure 1.9:** Potential variations of the  $\text{SiO}_2$  substrate. (a) Colour map of the spatial fluctuations in the surface potential in the vicinity of graphene flake. (b) Histogram of the potential fluctuation distribution in (a). The variance from the Gaussian fit is approximately equal to 50 mV. Lower resolution than in the scan of graphene surface is due to the bigger scanning distance (150nm) between surface and the tip comparing to the 50nm - distance for surface with graphene. A gaussian fit to the potential distribution yields a variance of 50mV. Adapted from [18].

the Dirac voltage. The induced fluctuations in the carrier density are smaller ( $\Delta n_{2D, T=0.3K} = \pm 3.9 \times 10^{10} \text{cm}^{-2}$  from Gaussian fit in Fig. 1.8(b)) than the density of charge impurities in  $\text{SiO}_2$  ( $50 \times 10^{12} \text{cm}^{-2}$ ), which means that impurities induce just a partial charge in graphene.

## 1.5 Short range and long range scattering mechanisms in graphene

Impurities not only induce variation of the crystal potential but they are additional source of scattering. Among them we distinguish neutral impurities and charged impurities. Neutral impurities (arising from defects or dislocations in the carbon lattice) produce short range potential and so called *short-range scattering*. Theoretically considered neutral impurities of concentration  $n_p$ , which produce radially symmetric potential of a typical radius size  $R \approx d_{C-C}$ , where  $d_{C-C} = 1.422 \text{ \AA}$  is an interatomic distance, result in rather small additional contribution to the resistivity,  $\delta\rho \approx (h/4e^2) n_p d_{C-C}^2$ . This contribution to resistivity is constant, independently of the induced carrier concentration [19].

The situation is different for charged impurities, which act as dopants and produce long range Coulomb potential and lead to so called *long-range scattering*. They can appear in the system as a result of gate doping or as a result of molecular doping (adsorption of charge transferring molecules), intentional or due to fabrication procedure. Around the defect site the opposite charge carriers nucleate, screening the defect potential. Hence, concentration of  $n_i$  charge impurities leads to the change in the electronic density of the order of  $n_i$ . The difference between the conductivities

for short- and long-type scatterers are presented in Fig. 1.10.

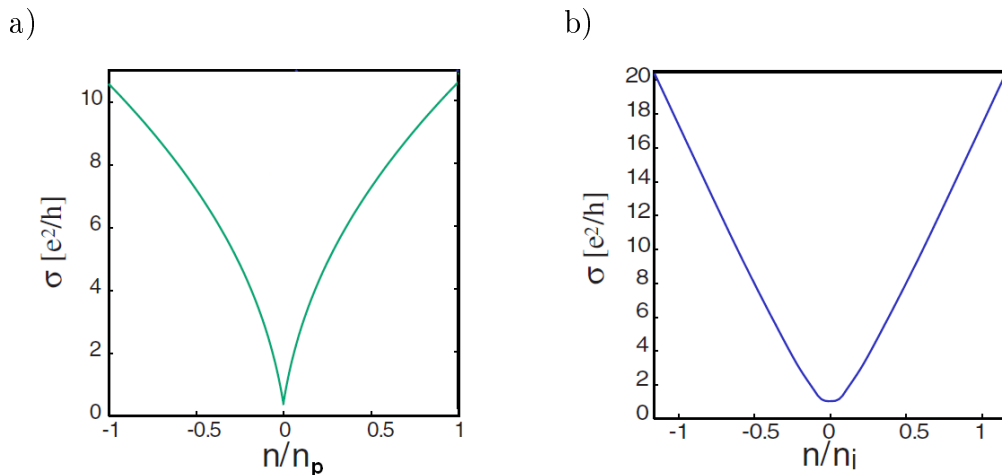


**Figure 1.10:** Conductivities in ideal graphene, at  $T=0K$ , for randomly distributed scatterers versus the carrier concentration induced by gate voltage  $n$ . (a) presents the dependence upon short-range scatterers and (b) upon screened Coulomb scatterers. Short range scatterers produce sub-linear relation of the conductivity, while Coulomb scatterers produce linear one. Adapted from [20].

In view of Boltzmann theory (applicable because carriers in graphene are weakly interacting), the conductivity for graphene is given by:

$$\sigma = \frac{e^2}{h} \frac{2E_F \langle \tau \rangle}{\hbar},$$

where  $\langle \tau \rangle$  is the energy averaged finite temperature scattering time. The Coulomb scattering time is proportional to the charge impurities concentration  $\tau_C \propto \sqrt{n_i}$ , while the short-range scattering time is inversely proportional  $\tau_s \propto 1/\sqrt{n_p}$ . From that it is clear that long-range scattering dominates at the low charge carrier concentration  $n$  (the scattering time is small), while the short-range scattering may play an important role at high densities  $n$  (we can assume that concentration of neutral impurities  $n_p$  is constant, irrespective of the gate voltage). The competition between these two types of scatterers determine the conductivity of graphene in different charge concentration regimes  $n$ . The crossover between these two mechanisms occurs when two scattering potentials are equivalent, that is:  $n_i V_i^2 \approx n_p V_p^2$ .

The theoretical calculations of conductivity versus gate induced carrier concentration  $n$  for different ratios between short and long range scatterers concentration are presented in Fig. 1.11. For small  $n_p/n_i$  ratio, the conductivity is linear in  $n$ , as it is seen in most experiments (compare with Fig. 1.4), while for large  $n_p/n_i$  ratio, in high carrier concentrations (for  $n > n_i$ ) the conductivity shows sublinear dependence [21, 22]. This effect is especially pronounced for very high mobility samples. Such high quality samples presumably have a small charge impurity concentration

$n_i$  and therefore neutral defects there play a more dominant role (see Fig. 1.11). In the presence of both the long-ranged charged impurity and the short-ranged neutral impurity, the total scattering time becomes  $1/\tau_{total} = 1/\tau_i + 1/\tau_p$ , where  $\tau_i$  ( $\tau_p$ ) is the scattering time due to charged Coulomb (short ranged) impurities. While the shift of the Dirac voltage  $V_{Dirac}$  away from zero-gate voltage serves as an indication of charge impurity concentration  $n_i$  (more precisely, it corresponds to the difference between positive and negative charge impurities - to the number of non-compensated charges), the presence of sublinearity may serve as an indication of the number of neutral scatterers and the sample quality.

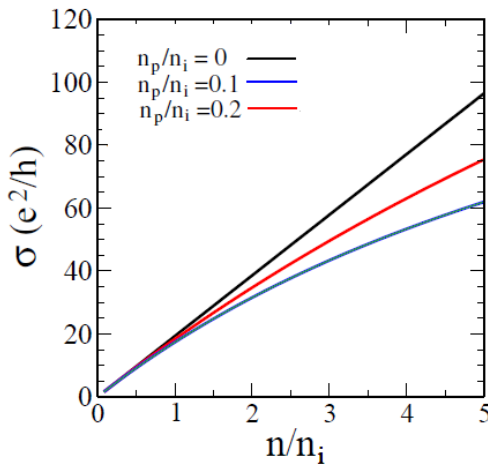


**Figure 1.11:** Graphene conductivity calculated in the presence of both short and long range scatterers. The sublinear conductivity at high density is likely to be seen in samples with a small Coulomb impurity density  $n_i$  and at high mobility. Adapted from [22]

The change from sub-linear conductivity to linear one under increase of charge impurities  $n_i$  was experimentally verified in [23]. In that experiment the authors studied the conductivity under exposure to the potassium flux (Fig. 1.12(a)). Potassium acts as an n-dopant (electron donor). The measurements were done at temperature  $T = 20$  K in ultrahigh vacuum (UHV). With the increase of doping time, we observe not only shift of the charge neutrality point (CNP), but also the change of the conductivity from sub-linear to linear gate-dependence. Fig. 1.12(b) presents the changes of mobility under exposure and the ratio between hole and electron mobilities.

On potassium doping:

1. the mobility decreases;
2. the dependence of the conductivity  $\sigma$  versus gate voltage becomes more linear;
3. the asymmetry between the mobilities of holes and electrons increases;
4. the charge neutrality point  $V_{Dirac}$  shifts to negative gate voltages;
5. the minimum conductivity  $\sigma_{min}$  decreases;

These experimental results can be easily understood in the view of the described scattering mechanisms. The change from sub-linear to linear curve shape of the conductivity, when the time of doping increases (Fig. 1.12), is related to the decrease of the ratio  $n_p/n_i$  between density of neutral impurities (constant in the system) and charge impurities (increased with the doping). The decrease of the mobility is the consequence of the increase of the charge impurity scatterers, which induce a screening potential and localise carriers, decreasing their velocity. For uncorrelated scatterers, the mobility depends inversely on the density of charged impurities,  $1/\mu \propto n_i$ , which is observed in Fig. 1.12(b). The asymmetry between the electron and hole mobility is the consequence of the different scattering strength for electrons and for holes. With doping we increase the disorder in the system (increase potential variations), which also leads to the formation of hole-electron puddles and decrease the minimum conductivity value  $\sigma_{min}$ . The experimental findings as well as theoretical predictions clarifies the dominant role of the charge impurity scattering (Coulomb scattering) in electronic transport and helps to describe the initial state of the device (we can roughly estimate the type and concentrations of impurities).

## 1.6 Initial molecular doping

All graphene devices are subjected to the adsorbates from the environment and contamination introduced during the device preparation. The adsorbed molecules can act as an electron acceptor (causing p-doping of graphene) or as an electron donor (causing n-doping of graphene). One clear evidence of the initial doping of the system is the fact that the charge neutrality points (CNP) is often shifted with

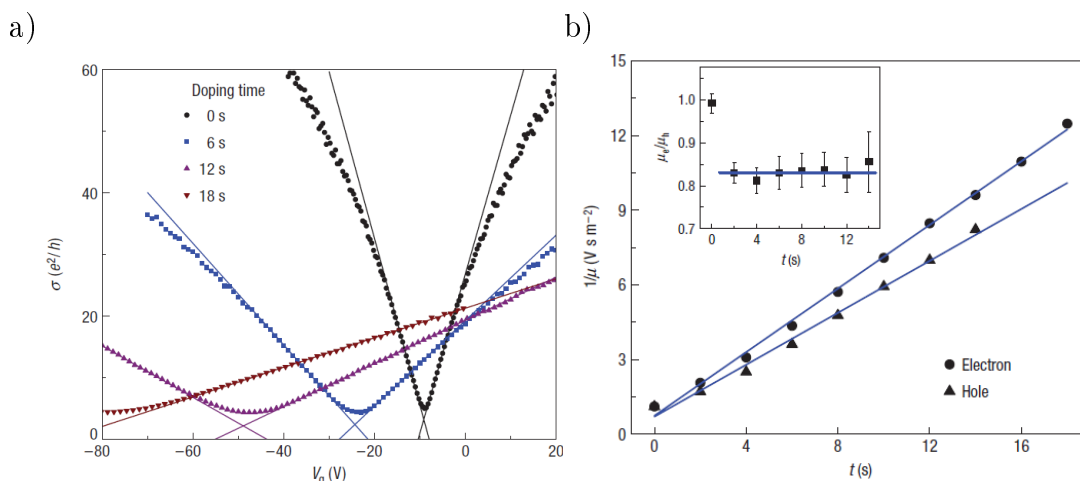


**Figure 1.12:** Potassium doping of graphene. (a) Conductivity vs gate voltage at different doping stages. (b) Inverse of electron mobility  $1/\mu_e$  and hole mobility  $1/\mu_h$  versus doping time. Inset: The ratio of the electron to hole mobility:  $\mu_e$  to  $\mu_h$  versus doping time. Adapted from [23].

respect to the zero-gate voltage. In this section I describe two most important doping mechanisms, which determine initial electronic performance of graphene device: *p-doping* from water molecules (always present in ambient environment) and *n-doping* from metal contacts.

All theoretical calculations predict that water molecule in contact with graphene behaves as an electron acceptor [24]. However, a strong dipole moment of water favours the binding between the H<sub>2</sub>O molecules and formation of water clusters rather than adsorption of individual molecules on graphene. This hydrophobic character of graphene implies that water molecules will always adsorb to graphene in clusters. The adsorption energy of the water clusters on graphene is defined as:  $E_a = (E_{cluster} + E_{graph}) - E_{total}$ , where  $E_{cluster}$  is isolated cluster,  $E_{graph}$  is the energy of a perfect graphene layer, and  $E_{total}$  is the total energy of the cluster-graphene system. The highest adsorption energy is found for clusters build from 5 water molecules. A corresponding charge transfer per molecule is 0.002e [25]. This leads to the shift of the CNP to positive gate-voltages. The water as well as other residual contaminations left after device preparation can be removed by annealing in vacuum. As a result, the Dirac neutrality point shifts back towards the zero gate voltage.

As a puzzle for a while was the origin of the shift of the CNP to negative voltages in vacuum after annealing. Desorption of water and some residues of polymer should bring the CNP back to zero, as we remove p-dopants. However, recent studies reveal that contacting metals on graphene act as an electron donors (n-dopants) [26]. Titanium (Ti) is of particular interest because it is commonly used as an adhesion layer for gold (Au). At the interface between two materials, a key factor in determining how electrons will transfer is the work function,  $\phi$ , which is the minimum energy needed to remove an electron from a material. For two materials in contact, the material having higher work function acts generally as an acceptor of electrons. When we compare the graphene work function,  $\phi_{gr} \simeq 4.5eV$ , with the work function of Ti,  $\phi_{Ti} \simeq 4.3eV$ , we notice that  $\phi_{gr} > \phi_{Ti}$  and we expect the donor behaviour of Ti. This was confirmed in [26], where the authors studied the influence of Ti-coverage on conductivity and observed the shift of the Dirac voltage (identified as a voltage at minimum conductivity) to negative values (Fig. 1.13).

Like in the case of doping with potassium [23], we observe similar changes in electronic transport, as listed on page 13, namely: the decrease of mobility, the disappearance of sub-linear shape of the conductivity  $\sigma$  under doping, the shift of the charge neutrality point to negative values, the decrease of the minimum conductivity  $\sigma_{min}$ . All these effects arises from increase of charge transferring impurities and related to them Coulomb scattering.

To sum up, the mechanism of molecular doping can occur unintentionally, as an effect of fabrication procedure and environment (doping by contamination left during the device preparation, due to presence of water, of Ti-contacts, of a substrate). The detailed description of initial quality of the device and the role of unavoidable

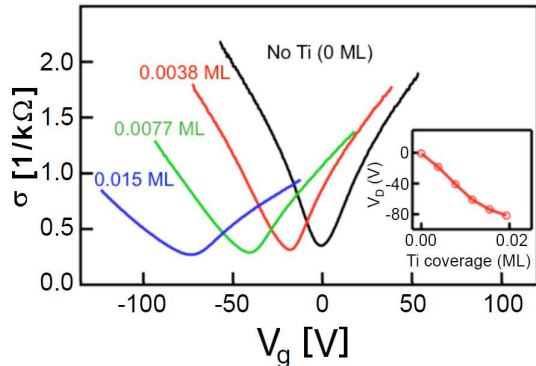


**Figure 1.13:** Conductivity as a function of gate voltage  $V_g$  for increasing Ti-coverage in graphene. The Dirac point, identified by the minimum in the conductivity curves, shifts towards negative voltages with the increase of the Ti-coverage, indicating that the Ti acts as a donor (n-type doping). The inset displays the dependence of the Dirac voltage  $V_D$  as a function of Ti coverage (scale is expressed in terms of full monolayer coverage, ML). The initial slope of the  $V_D$  vs Ti coverage data has a value of  $-4602.4V/ML$ , which reflects the doping efficiency. Adapted from [26].

dopants is necessary for understanding of electronic transport in graphene.

## 1.7 Hall effect: determination of charge carrier concentration

An optimal technique for detection of changes in charge carrier density is the Hall effect measurements. The Hall effect produces a potential difference (the Hall voltage) across an electrical conductor, transverse to an electric current path at magnetic field perpendicular to the current due to the Lorentz force. From the measurements of transversal resistance  $R_{xy}$ , also called Hall resistance, under magnetic field  $B$ , we readily obtain the Hall coefficient through the relation  $R_{xy} = R_H B$  (for  $B=1T$   $R_{xy}$  and  $R_H$  are identical). The charge neutrality point for  $R_{xy}$  occurs for the voltage where  $R_{xy} = 0$ . The measurements of the Hall coefficient  $R_H$ , by the use of relation:

$$R_H = \frac{1}{ne}. \quad (1.6)$$

gives information about the total carrier concentration in the system.

Experimental results in [27] show that under exposure to the mixture of  $NO_2$  and  $N_2O_4$  (both act as acceptors) the charge neutrality point shifts to positive values (Fig. 1.14 (a)), the difference in resistivity between maximums of  $R_{xy}$  decreases and they occur at larger voltage distances. These changes can be easier distinguished on the plot of inverse resistance  $1/R_{xy}$  (Fig. 1.14 (b), where  $\Delta_1$  marks the shift of charge neutrality point, and  $\Delta_2$  is the half of the voltage distance between  $R_{xy}$  maximum and minimum).

Away from the Dirac point,  $1/R_H$  is linear with the gate voltage, according to

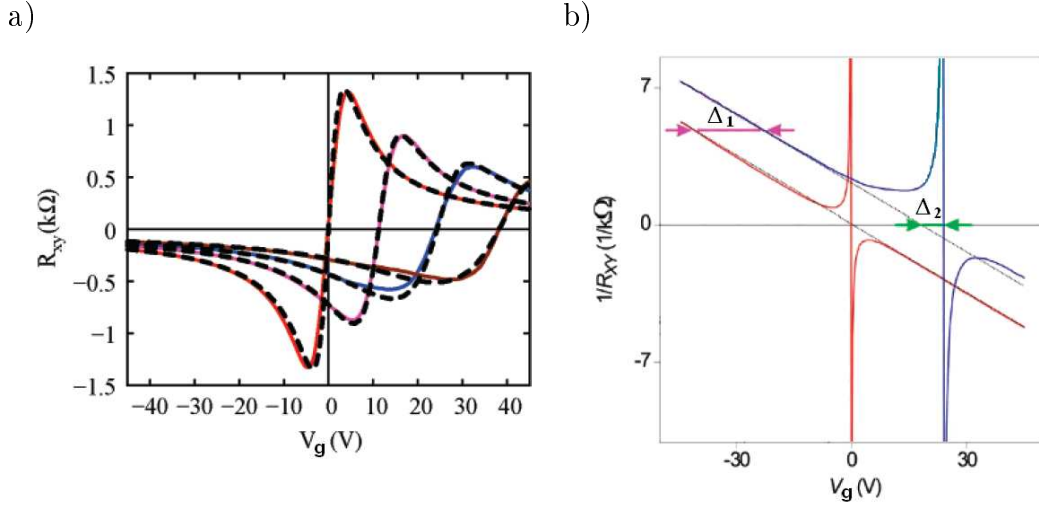


**Figure 1.14:** Transversal resistance  $R_{xy}$  as a function of gate voltage  $V_g$  under increase of doping with mixture of gases:  $NO_2/N_2O_4$  (p-doping) (a). Measurements were done at  $B=1T$ , where  $R_{xy} = R_H$ . The solid lines are the experimental results, with the brown curve corresponding to the highest concentration of adsorbates, and the red curve corresponding to almost zero doping. (b) presents  $1/R_{xy}$  for initial (red curve, calculated from red curve of  $R_{xy}$  in (a)) and doped (blue curve, calculated from blue curve of  $R_{xy}$  in (a)) graphene samples. Adapted from [27].

Eq. 1.6. From the slope of the linear fit we can extract exact value of coefficient  $\alpha$  which describes proportionality between the induced charge carriers and the applied gate voltage according to the Eq. 1.2. Close to the Dirac point we observe the divergence of  $1/R_H$ , which is related to the vanishing density of carriers.

From above we can conclude that under exposure to charge transferring molecules the Hall coefficient  $R_H$  exhibits two characteristic features:

1. the charge neutrality point shifts to positive (in case of p-doping) or to negative (for n-doping) gate voltages;
2. the transition regions between two maximums of  $R_H$  becomes wider, and simultaneously the maximums becomes lower with the increase of doping.

These features give also indication of the initial sample quality.

## 1.8 Positive magnetoresistance in graphene

Another feature of graphene is the magnetoresistance - the change of graphene longitudinal resistance  $R_{xx}$  under magnetic field. Away from the charge neutrality point the graphene longitudinal resistance  $R_{xx}$  is almost independent from the

magnetic field. However, closer to the Dirac point the positive magnetoresistance (increase of resistance with increase of the field) is stronger, reaching its maximum at charge neutrality point (CNP) (Fig. 1.15).

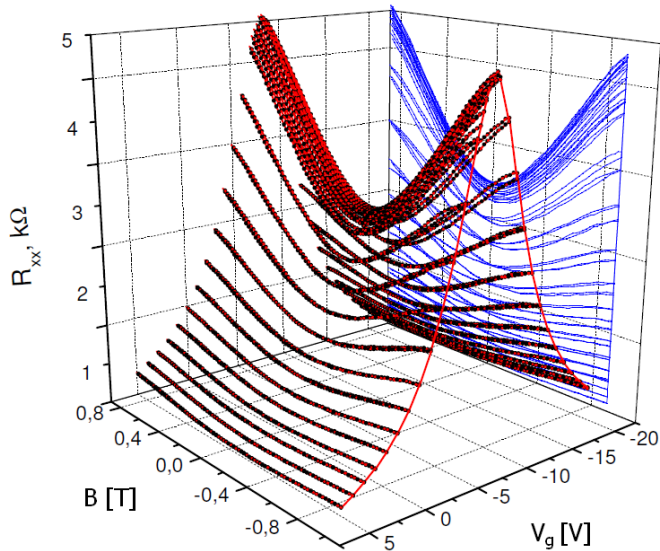


**Figure 1.15:** Longitudinal resistance  $R_{xx}$  as a function of magnetic field  $B$  at different gate voltages  $V_g$ . Adapted from [28].

### 1.8.1 Classical origins of magnetoresistance

Within the Drude model, which is used to describe ideal graphene, a two-dimensional conductor with an one carrier type exhibits no longitudinal magnetoresistivity, because the voltage drop occurs simultaneously along the current path. However, a conductor with electrons and holes may exhibit large longitudinal magnetoresistivity, due to the development of different components of drift velocity perpendicular to the current. The increase of magnetoresistivity while approaching the Dirac point is a strong indication that two types of carriers contribute to the transport. Fig. 1.16(a) presents the change of maximum resistivity ( $R_{xx}$  at CNP) under magnetic field for different temperatures. With the increase of the temperature the magnetoresistivity effect increases (the difference between resistivity at zero magnetic field and at  $B=8\text{T}$  increases with temperature, from  $\sim 0.25$  to  $\sim 0.65h/e^2$ ). With the increase of temperature also the saturation of resistivity starts from larger magnetic fields.

In all measured temperatures, at low magnetic fields  $R_{xx}$  shows positive magnetoresistance (Fig. 1.16(b)) of the similar size. This supports the idea that disorder effects which are weakly temperature dependent, like electron-hole puddles, dominate in building up two-charge type carrier system in the vicinity of CNP. The detailed description of the possible origins of positive magnetoresistance at room

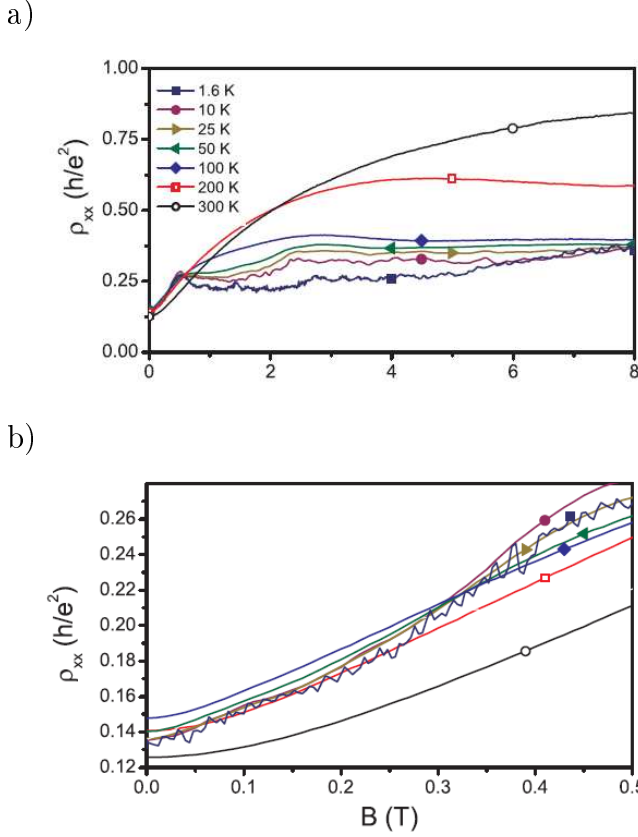


**Figure 1.16:** Longitudinal resistivity  $\rho_{xx}$  at charge neutrality point as a function of magnetic field  $B$  at various temperatures (a). The zoomed-in region for low fields is presented in (b). Adapted from [29].

temperature within a classical approach to model this effect will be extended in the chapter 2.

## 1.8.2 Magnetoresistance due to quantum localisation effects

Another effect, which plays a role in building up a magnetoresistance is weak localisation and anti-localisation. These are purely quantum mechanical effects which arise at low temperatures. When the Fermi wavelength is comparable or longer than the mean free path of electron ( $k_F l \lesssim 1$ ) electrons remain coherent over long distances. As the quantum interference and the coherent scattering occur, the classical (Drude) expression for resistivity has to be modified with weak localisation corrections. These corrections are usually due to the positive interference between two paths of electron along closed loops, traversed in opposite directions (Fig. 1.17). As the two paths are identical, the phase of the waves is the same and at the point of intercept the interference is constructive. This increases the probability of the electron to stay in the intercept region (to be weakly localised) and increase the overall electrical resistance. This interference is suppressed for paths longer than the dephasing length (the length over which the coherence is destroyed). Interference effects can be also suppressed by magnetic fields that break down time reversal symmetry and adds a random relative phase to the electron wavefunction. Hence in

most metals the resistivity decreases when a small magnetic field is applied (negative magnetoresistance).

In graphene the charge carriers are chiral and their wavefunction has an additional (Berry) phase, which arises due to the zero effective carrier mass near the Dirac points [30]. This leads to the opposite effect than in metals: to anti-localisation and decrease of resistance. Applying magnetic field randomises the phase and suppress the anti-localisation effect, which leads to the increase of resistivity in magnetic fields (positive magnetoresistance).

The graphene's band structure has two valleys ( $k, k'$ ), with an opposite chirality. Anti-localisation occurs due to scattering within the valley (intra-valley scattering). On the other hand, localisation effects occur for electron scattered between the valleys (inter-valley scattering) as the quantum interference there is suppressed. Inter-valley scattering can happen on sharp defects, which are able to change strongly the momentum of the electron (for example edges of the sample). In [31] was shown that graphene, depending on experimental conditions, can demonstrate both localisation and anti-localisation effects. These findings are presented in Fig. 1.18, where conductivity difference vs magnetic field was recorded at three different carrier concentrations. Negative values of  $d\sigma_{xx}/dB$  correspond to negative magnetoconductivity (positive magnetoresistivity) while positive values correspond to positive magnetoconductivity (negative magnetoresistivity). According to [31] this quantum interference effects can survive up to  $T \approx 200$  K.

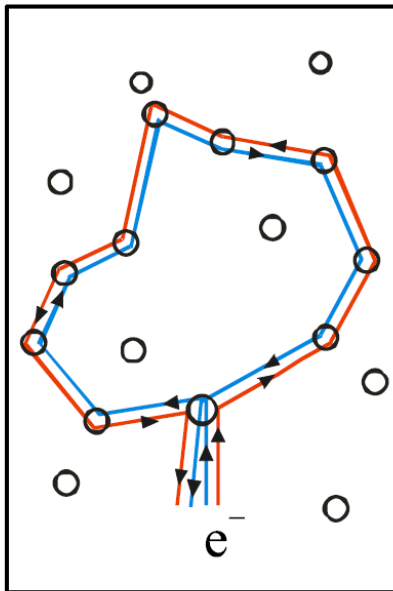


**Figure 1.17:** The trajectories of an electron scattered by impurities that give rise to quantum interference. In graphene this type of interference, due to additional phase in electrons wavefunction (Berry phase), gives rise to anti-localisation. The interference is suppressed for paths longer than the dephasing length. After [31].

In the experiment, I focus on graphene properties in diffusion transport regime at room temperature. Presented further theoretical analysis as well as experimental results were done at room temperature for device of few  $\mu m$  wide, where the features of ballistic transport as well as the quantum interference effects disappear.

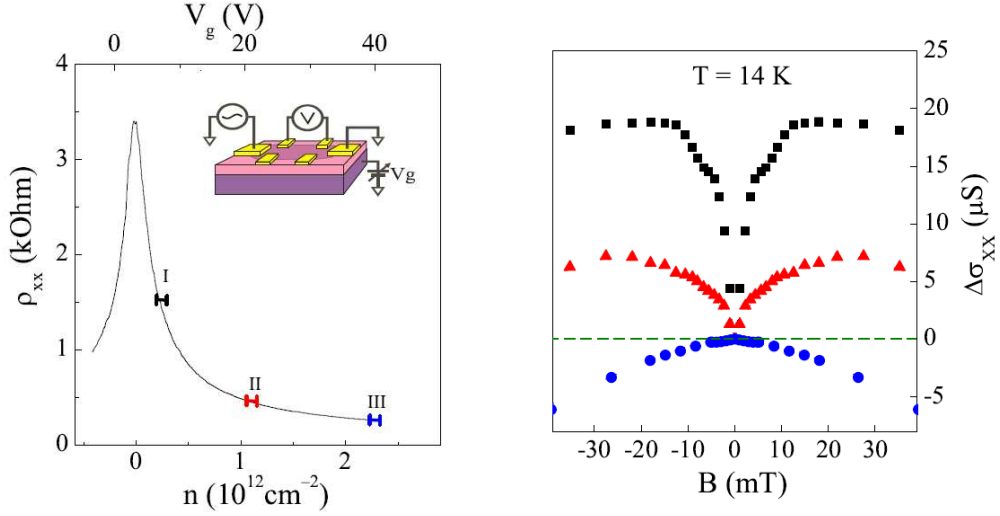


**Figure 1.18:** Resistivity as a function of the carrier density, with three points for which magnetoconductance was studied (a). Insets: a scheme of the device. (b) First derivative of conductivity vs magnetic field at  $T=14$  K. With increasing electron density (moving from region III to region I in (a))  $d\sigma_{xx}/dB$  changes its sign from positive to negative (the dashed green line indicates zero level). This sign-change corresponds to change from positive magnetoconductivity (negative magnetoresistivity) to negative magnetoconductivity (positive magnetoresistivity) and is the evidence for localisation and anti-localisation. Adapted from [31].

The presented in this chapter features of graphene: its conical bandstructure and rippling together with its interactions with environment: doping by substrate and adsorbed molecules, have direct consequences for electronic transport measurements and description of the initial graphene quality. Many of these features are interdependent (for example the electric potential variations imposed by a substrate can be possibly compensated by adsorbed molecules) therefore it is not trivial to give simple relation between different quantities (like the relation between mobility and gate voltage in graphene device). In the next section I will focus on mechanisms, which stimulate the occurrence of both types of carriers, electrons and holes, in the vicinity of Dirac point: thermal equilibrium excitations and fluctuations of electric potential, which leads to spatial fluctuations of the doping level (formation of electron-hole puddles).



# Transport in one vs two charge carrier system. Magnetoresistance.

The analysis of the electronic band structure of ideal graphene suggests that its conductivity is carried by only one-type of carriers, either electrons or holes depending on the location of the Fermi level. This idealised picture has to be extended for the finite temperature measurements, where thermal equilibrium leads to the population of states above the Fermi level. In this chapter I analyse the density of states and the carrier concentration in graphene at room temperature without and with additionally fluctuating potential. The effect of fluctuating potential is induced by the substrate and adsorbed charge transferring molecules (dopants) and leads to the formation of hole-electron puddles. . Both effects (thermal equilibrium and variation of potential) leads to the coexistence of holes and electrons in the vicinity of charge neutrality point (CNT). Therefore, the one-type carrier description (Drude model) needs to be extended. Semiclassical analysis of transport in the two type carrier system is here presented and expressions for resistances versus gate voltage and magnetic field are derived. The resistivities calculated for graphene carrier densities (at room temperature and with fluctuating potential) exhibit finite maximum of longitudinal resistance  $\rho_{xx}$  and zero transversal resistance  $\rho_{xy}$  at CNT and magnetoresistance which agrees with experimental observations. In the end of the chapter the influence of parameters from the model on the resistance maximum and width of the curve between deflection points is analysed.

## 2.1 Carriers in ideal graphene at room temperature.

In an undoped graphene layer in thermal equilibrium, there are mobile electrons in the conduction band and holes in the valence band, similar to the thermally excited holes and electrons in an intrinsic bulk semiconductor. As the conductivity of graphene depends on number of carriers available in the vicinity of Fermi level, we need to find the density of such intrinsic carriers in two-dimensional (2D) system. Taking linear energy dispersion relation (Eq. 1.1), the 2D density of states (DOS)

is as follows:

$$\rho_{gr}(E) = \frac{1}{V} \frac{dN}{dk} = \frac{1}{V} \frac{dN}{dk} \frac{dk}{dE} = \frac{g_s g_v |E|}{2\pi(\hbar v_F)^2} \quad (2.1)$$

where  $V$  is the 2D volume of graphene,  $N$  is the number of available states in the Fermi sphere, the prefactors  $g_s = 2$ ,  $g_v = 2$  take into account the spin and valley degeneracy. In thermal equilibrium the density of carriers is calculated as a product of the DOS and the probability distribution function (as the carriers undergo fermion statistics, we use Fermi-Dirac distribution  $f_{FD}(E) = (\exp(\frac{E-\mu}{k_B T}) + 1)^{-1}$ , where  $\mu$  is the chemical potential. The chemical potential of a system of electrons is also called the Fermi level and later on this name will be used). In undoped system ( $E_F = 0$ ), we calculate the number of conducting electrons ( $n$ ) as follows:

$$n(T) = \int_0^{\infty} f_{FD, n}(E) \rho(E) dE \quad (2.2)$$

where  $f_{FD, n}(E) = (\exp(\frac{E-E_F}{k_B T}) + 1)^{-1}$ .

The density of conducting holes (denoted as  $p$ ) is calculated from similar formula, ( $f_{FD, p} = 1 - f_{FD, n} = (\exp(\frac{E_F-E}{k_B T}) + 1)^{-1}$ ) as follows:

$$p(T) = \int_{-\infty}^0 f_{FD, p}(E) \rho(E) dE \quad (2.3)$$

The density of states and the Fermi distribution, which contribute to these integrals are schematically presented in Fig. 2.1.

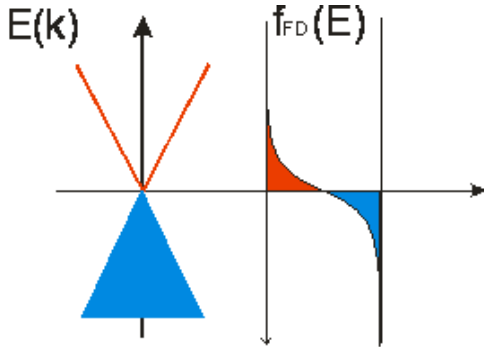


**Figure 2.1:** A scheme of the bands occupation and the corresponding Fermi distribution for  $E_F = 0$  at finite temperatures. Indicated in blue valence band is fully occupied, while the conduction band is empty. However, thermal equilibrium allows to occupy upper and lower states according to the Fermi-Dirac distribution (red colour indicates the non-zero population for electrons, while blue for holes).

Taking Fermi velocity of carriers in graphene ( $v_F = 10^6 m/s$ ), at room temperature ( $k_B T \approx 26 meV$ ) and integrating the formulas for  $n$  and  $p$ , we get:

$$n = p = \frac{\pi(k_B T)^2}{6(\hbar v_F)^2} \cong 8.2 \times 10^{10} cm^{-2} \quad (2.4)$$

From above we can see that at finite temperature the ideal graphene is not a purely one-type carrier system and that even when the Fermi level lies exactly at Dirac

points, there are still carriers of both type present in the system (compare with [32]).

When we apply an external electric field, the Fermi level is shifted, and the density of one type carrier dominates over the other (see Fig. 2.2). Fig. 2.3 presents

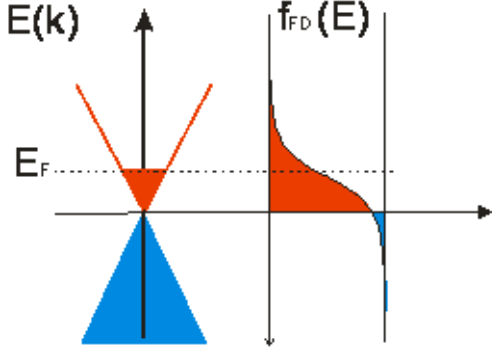


**Figure 2.2:** Scheme of bands occupation and corresponding Fermi distribution for  $E_F > 0$  at finite temperatures. Indicated in blue valence band is fully occupied, but there is a considerable number of electron states in conduction band. Shift of the Fermi level up increases population of electrons in conduction band (red colour), while decreasing the number of holes.

the concentrations of electrons and holes at room temperature. When  $E_F \neq 0$  one carrier type dominates over the other (separation into majority and minority carriers). For sufficiently large shift of the Fermi level from zero (Dirac point), the density of minority carriers in graphene is negligible and the system can be considered as one-type charge carrier.

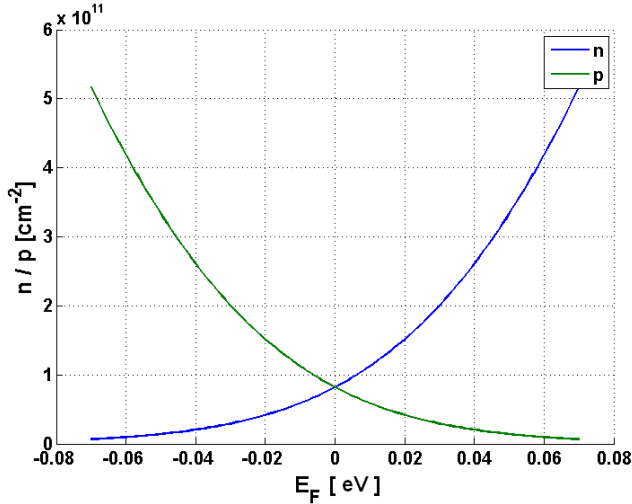


**Figure 2.3:** The charge carrier concentration for different position of the Fermi level at room temperature. The green curve indicates concentration of holes, the blue - concentration of electrons.

In the experiment we control the number of induced charge carriers by applying the gate voltage. Both the Fermi level and the gate voltage have a direct correspondence to the charge carrier density. The charge carrier density  $n$  is a function of the Fermi level through Eq. 2.2 and Eq. 2.2, while it is a function of gate voltage through Eq. 1.2. Taking into account the fact, that the gate voltage induces the difference between positively and negatively charged carriers ( $p - n = \alpha V_g$ ), we

can find (numerically) the dependence of the shift of the Fermi level from the gate voltage. The conversion from the position of the Fermi level to the gate voltages

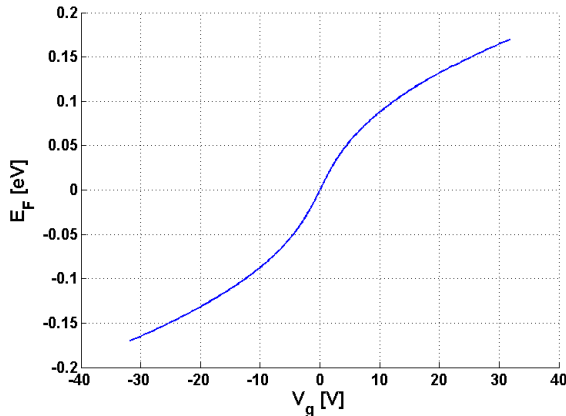


**Figure 2.4:** Shift of Fermi level in graphene due to gate voltage at room temperature.

based on corresponding charge carrier densities will be used further on for calculations of the resistivities. Presented here semi-classical description of carrier density in ideal graphene shows that the carrier density vanishes for  $T \rightarrow 0K$ . Therefore this approach doesn't explain the occurrence of minimum conductivity, which is also present at liquid helium temperatures. However, it serves as a good indication that with the increase of temperature the voltage range where densities of electrons and holes are comparable also increases. At room temperature the region of considerable densities of minority carriers corresponds to the gate voltages  $V_g \in (-5V, 5V)$ , giving the argument that the transport cannot be described there by only one-type of carriers model (Drude description).

## 2.2 Carriers in graphene with electron and hole puddles.

A suggestion that in the vicinity of the Dirac point graphene system behaves like a two-type charge carrier system has several reasons. Firstly we have to include the finite temperature broadening of the energy levels in the band structure (in room temperature, broadening of the states is around 30mV). This allows for a coexistence of electrons and holes due to thermal fluctuations and disorder in the vicinity of the Dirac point. Secondly, graphene is affected by charge impurities, especially these originating from rough  $\text{SiO}_2$  substrate. Charge impurities shift locally the Fermi level, creating hole-rich and electron-rich puddles (described in section 1.4). Additionally the rippling of graphene effectively broadens Dirac point (described in section 1.3). All this effects can explain observations of non-zero minimum conductivity at Dirac point (where in principle the density of states should vanish).

In transport measurements we are averaging the contribution of charge carriers in different parts of graphene (from different electron- and hole-rich puddles). With an increase of the gate voltage above CNP hole puddles "dry" out and as a result we turn to the pure electron conduction, as it is presented in Fig. 2.5). Similarly, when we decrease the gate voltage below CNP we "dry" out electron puddles up to pure hole conduction state. The detailed description of holes and puddles is unattainable, as it depends on topography of graphene, its substrate, molecular dopants, etc. However, for a sufficiently large system, we can average its influence using the Gaussian distribution with position of the Fermi level as its argument and with the standard deviation  $\sigma$ , as follows.

$$n = \frac{1}{\sqrt{2\pi}\sigma} \int_{-\text{inf}}^{\text{inf}} n(T, E_F = b) \cdot \exp\left(-\frac{b^2}{2\sigma}\right) db \quad (2.5)$$

$$p = -\frac{1}{\sqrt{2\pi}\sigma} \int_{-\text{inf}}^{\text{inf}} p(T, E_F = b) \cdot \exp\left(-\frac{b^2}{2\sigma}\right) db \quad (2.6)$$

where  $b$  represents the shift of the Fermi level from zero (from the Dirac point),  $p(T, E_F)$  is defined in Eq. 2.3,  $n(T, E_F)$  is defined in Eq. 2.2. In numerical calculations, due to practical reasons, integration range is cut off at  $\pm 3\sigma$ , which accounts 99.7% of the set.

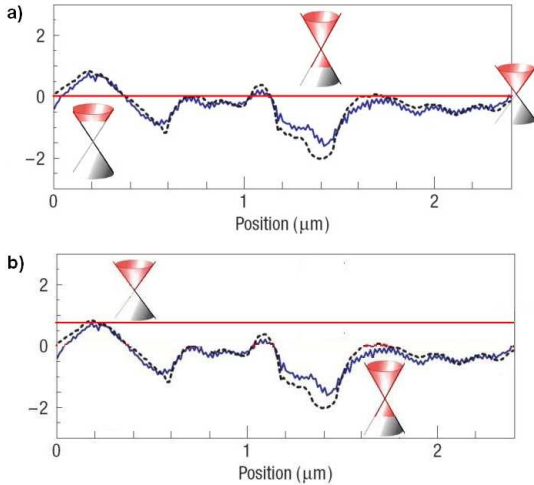


**Figure 2.5:** Mechanism of drying puddles when the external voltage is applied. At the zero gate voltage, indicated by red line in (a), we can see local variations of the potential and corresponding occupation of the band structure. The total charge from electron-rich puddles is compensated by the charge from hole-rich puddles. An application of external voltage (b) shifts the Fermi level and dries out the puddles. One type of carriers start to dominate over the other. We can distinguish majority and minority type of carriers.

The concentration of charge carriers at room temperature for ideal graphene and graphene with additional effect of homogeneously distributed, symmetric puddles (of the Gaussian distribution with  $\sigma = 20\text{meV}$ ) are presented in Fig. 2.6. We notice that away from the Dirac point the concentrations of  $n$  and  $p$  with puddles converge to the concentrations of  $n$  and  $p$  for ideal graphene. This is because at large carrier densities the small local changes in number of carriers become negligible. On the other hand, close to the Dirac point, we can see that the carriers density for holes and for electrons is comparable and cannot be neglected. At the zero Fermi level

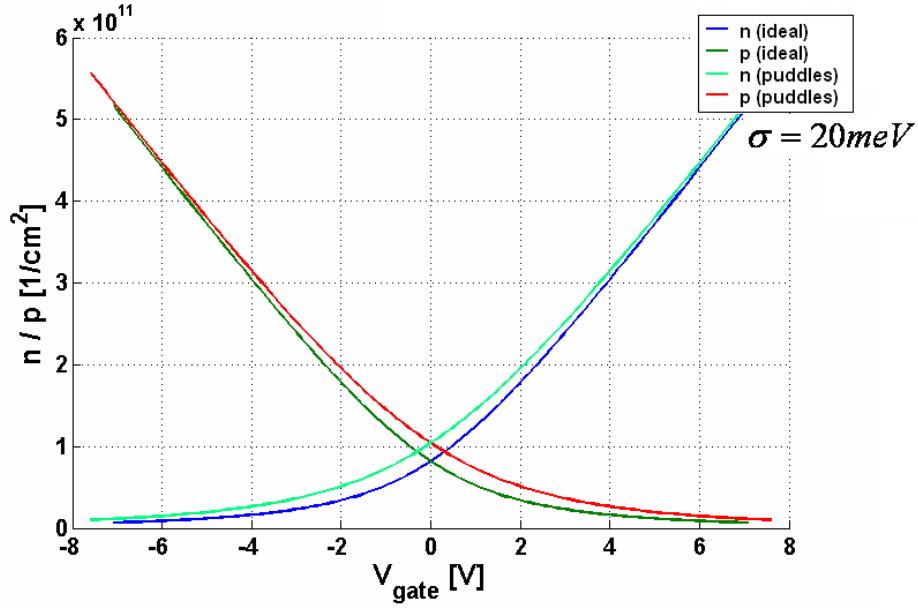


**Figure 2.6:** Charge carrier concentration for ideal graphene (blue and dark green) and ideal graphene with puddles, modelled by the Gaussian distribution of the Fermi level (red and light green) at room temperature. The standard deviation of Fermi level is taken  $\sigma = 20\text{meV}$ .

the carrier density for model with puddles  $\sigma = 20\text{meV}$  is  $n = p \cong 9.6 \times 10^{10}\text{cm}^{-2}$  and it is higher than for ideal graphene, where  $n = p \cong 8.2 \times 10^{10}\text{cm}^{-2}$ . The carrier density at the Dirac point increases with the increase of the Gaussian broadening, which is illustrated in Fig. 2.7.

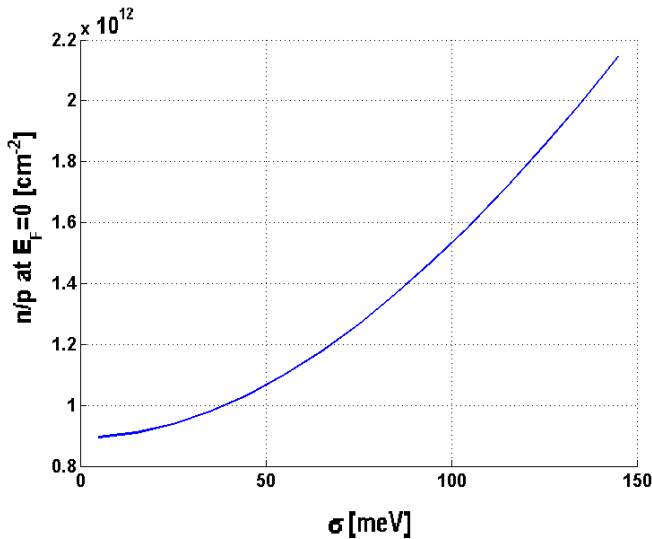


**Figure 2.7:** The charge carrier concentration at the Dirac point for different size of puddles (different width of the Gaussian distribution  $\sigma$ ).

In the literature there are also other methods exploring the influence of potential variations on carrier densities in graphene to calculate the carrier density, e.g. self-consistent random phase approximation [34], constant puddle-depth model [35]. The description presented here is the most simple one addressing this question.

## 2.3 Resistivity in one vs two charge type carrier system. Magnetoresistance.

For generality I describe transport in a two carrier-type system, because the model for a one-type carrier system (Drude model), can be readily obtained from the general formulas by setting the density of minor carriers to zero.

Let us consider system with the two type of charge carriers: electrons and holes. In classical picture an application of a net electrostatic force  $\mathbf{F}_{el} = q\mathbf{E}$  results in a charge carrier drift. The drift velocity  $v_q$  of charge  $q$  caused by the net force  $\mathbf{F}_{net}$  satisfies the relation:  $\mathbf{F}_q = q\mathbf{v}_q/\mu_q$  where  $\mathbf{v}_q = \mu_q\mathbf{E}$ . Moving charges in magnetic field non-parallel to their motion path experience the Lorentz force:  $\mathbf{F}_L = q(\mathbf{v}_q \times \mathbf{B})$ .

Let us consider an ambipolar conductor set in a magnetic field  $B_z$  as indicated in Fig. 2.8. When one applies the voltage drop along the  $x$  direction, electrons and holes start to drift in opposite directions along the same axis. As magnetic field is perpendicular to their motion, the Lorentz force will deflected the motion of carriers to the same side of the material (Lorentz force is pointed to the same direction for holes and for electrons, because they are moving in the opposite direction). As a result, charges accumulate on one face of the material, leaving equal and opposite charges on the other face. When the density of carriers as well as their mobilities are equal, there is no potential drop across the conductor (negative electrons compensate positive holes). On the other hand when the density of different carriers or their mobilities differ, we have an asymmetric distribution of the charge density across the material. It establishes an electric field  $E_y$  that opposes further migration of charges, so that a steady electrical potential (Hall potential) builds up.

For a charge  $q$  in a magnetic field (in our experiment we consider magnetic field with just  $z$  component  $\mathbf{B} = (0, 0, B)$ ), which travels in  $x$  and  $y$  direction as presented in Fig. 2.8, the equation of motion can be derived in the following way:

$$\frac{q\mathbf{v}_q}{\mu_q} = \mathbf{F}_{net,q} = \mathbf{F}_{el} + \mathbf{F}_L \quad (2.7)$$

where  $\mathbf{F}_{el} = q\mathbf{E}$  is the electric force in the system. In case of holes, for which  $q = e$ , where  $e$  is the elementary charge ( $e \cong 1.602 \times 10^{-19}$  C), we obtain the following:

$$\begin{aligned} \frac{ev_{hx}}{\mu_h} &= e(E_x + v_{hy}B) \\ \frac{ev_{hy}}{\mu_h} &= e(E_y - v_{hx}B) \end{aligned}$$

(for holes their velocity and mobility keep index 'h'). In case of electrons, for which  $q = -e$ , we have to take into account that they are moving in the opposite to holes direction, hence we obtain:

$$\frac{e v_{ex}}{\mu_e} = e(E_x - v_{ey} B)$$

$$\frac{e v_{ey}}{\mu_e} = e(E_y + v_{ex} B)$$

(for electrons their velocity and mobility keep index 'e').

Rewriting equations for velocities in matrix forms we get for electrons and holes respectively:

$$\begin{pmatrix} 1 & \mu_e B \\ -\mu_e B & 1 \end{pmatrix} \cdot \begin{bmatrix} v_{ex} \\ v_{ey} \end{bmatrix} = -\mu_e \begin{bmatrix} E_x \\ E_y \end{bmatrix} \quad (2.8)$$

$$\begin{pmatrix} 1 & -\mu_h B \\ \mu_h B & 1 \end{pmatrix} \cdot \begin{bmatrix} v_{hx} \\ v_{hy} \end{bmatrix} = \mu_h \begin{bmatrix} E_x \\ E_y \end{bmatrix} \quad (2.9)$$

After algebraic inversion, the expressions for the velocities look as follows:

$$\begin{bmatrix} v_{ex} \\ v_{ey} \end{bmatrix} = \frac{-\mu_e}{1 + (\mu_e B)^2} \cdot \begin{pmatrix} 1 & -\mu_e B \\ \mu_e B & 1 \end{pmatrix} \cdot \begin{bmatrix} E_x \\ E_y \end{bmatrix}$$

$$\begin{bmatrix} v_{hx} \\ v_{hy} \end{bmatrix} = \frac{\mu_h}{1 + (\mu_h B)^2} \cdot \begin{pmatrix} 1 & \mu_h B \\ -\mu_h B & 1 \end{pmatrix} \cdot \begin{bmatrix} E_x \\ E_y \end{bmatrix}$$

The built-in potential prevents the carriers from the further migration so that in the  $y$ -direction there is no net current, therefore:  $J_y = J_{hy} + J_{ey} = epv_{hy} - env_{ey} = 0$ , where as  $p$  we denoted the concentration of holes and as  $n$  concentration of electrons. From that we obtain:  $pv_{hy} = nv_{ey}$ . On the other hand the current flowing along  $x$ -direction is non-zero and consists of two components  $J_x = J_{hx} + J_{ex} = epv_{hx} + env_{ex}$ .

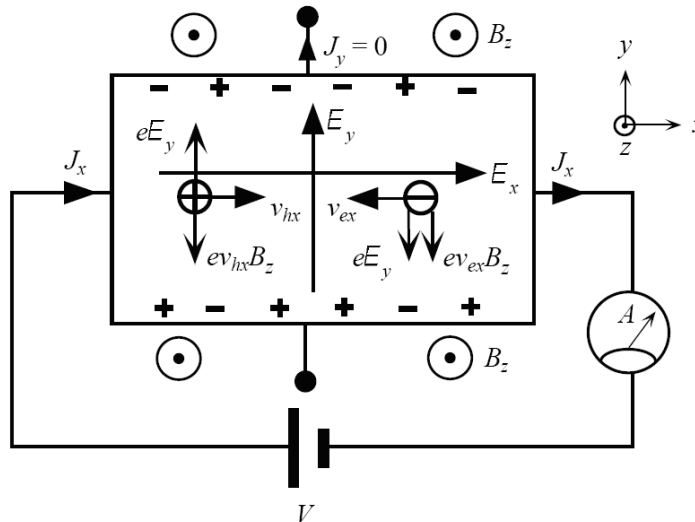


**Figure 2.8:** The origin of the Hall effect in bipolar conductor. The arrangement of forces acting on holes and on electrons: the electric force and the Lorentz force is denoted with arrows.

Comparing the last expression with the definition of conductivity  $\mathbf{J} = \sigma \mathbf{E}$ , we find the respective hole and electron conductivities:

$$\hat{\sigma}_h = \frac{ep\mu_h}{1 + (\mu_h B)^2} \cdot \begin{pmatrix} 1 & -\mu_h B \\ \mu_h B & 1 \end{pmatrix} \quad (2.10)$$

$$\hat{\sigma}_e = \frac{en\mu_e}{1 + (\mu_e B)^2} \cdot \begin{pmatrix} 1 & \mu_e B \\ -\mu_e B & 1 \end{pmatrix} \quad (2.11)$$

The total conductivity of a two-charge-type system is the sum of the conductivities of each type (for carriers which are not coupled)  $\hat{\sigma} = \hat{\sigma}_e + \hat{\sigma}_h$ . In experiment, we measure resistivities rather than conductivities, therefore we convert the equations using the tensor relation:  $\hat{\rho} = \hat{\sigma}^{-1}$ . Further analysis is held for equal mobilities of both charge type carriers:  $\mu_e = \mu_h = \mu$ , as this is the case in graphene. After inverting the total tensor of conductivity we obtain:

$$\hat{\rho} = \frac{1 + (\mu B)^2}{e\mu[(p+n)^2 + (\mu B)^2(p-n)^2]} \begin{pmatrix} p+n & -B\mu(p-n) \\ B\mu(p-n) & p+n \end{pmatrix}$$

Putting the longitudinal resistivity  $\rho_{xx}$  and the transversal resistivity  $\rho_{xy}$  explicitly, we get:

$$\rho_{xx} = \frac{(p+n) \cdot (1 + (\mu B)^2)}{e\mu[(p+n)^2 + (\mu B)^2(p-n)^2]} \quad (2.12)$$

$$\rho_{xy} = -\frac{(p-n) \cdot (1 + (\mu B)^2)}{e[(p+n)^2 + (\mu B)^2(p-n)^2]} \quad (2.13)$$

From the last formula we can extract the Hall coefficient  $R_H$ , as  $\rho_{xy} = R_H \cdot B$ . On the contrary to the one charge type carrier model, in the two type model  $R_H$  turns out to be field dependent:

$$R_H = \frac{(n-p) \cdot (1 + (\mu B)^2)}{e[(p+n)^2 + (\mu B)^2(p-n)^2]}$$

This description should be replaced by a much easier one, when we consider ideal graphene sheet at absolute zero temperature. With the external gate voltage  $V_g$  we can shift the Fermi level of the system, switching from the one charge type transport, either electron or hole, to another (Drude system). In such a case, equations for resistivity (2.12), (2.13) should be reduced by inserting appropriate form of the carrier concentration. This leads us to the Drude model of graphene resistivity:

$$\begin{aligned} \text{when } V_g > V_{Dirac} \quad p = 0, \quad n = \alpha(V_g - V_{Dirac}) \\ \rho_{xx} = \frac{1}{e\mu n}, \quad \rho_{xy} = \frac{B}{en} = R_H B \end{aligned} \quad (2.14)$$

$$\begin{aligned} \text{when } V_g < V_{Dirac} \quad n = 0, \quad p = \alpha(V_{Dirac} - V_g) \\ \rho_{xx} = \frac{1}{e\mu p}, \quad \rho_{xy} = \frac{B}{ep} = R_H B \end{aligned} \quad (2.15)$$

The experiment provides us with  $\rho_{xx}$ ,  $\rho_{xy}$ . Applying the above formulas, we can obtain the mobility and the carrier concentration, as follows:

$$\mu = \frac{1}{en\rho_{xx}}$$

$$n = \frac{B}{e\rho_{xy}}$$

A short analysis of formulas of Drude model for the one-type of carriers system (Eq. 2.14 and Eq. 2.15) gives the following remarks:

1. the mobility diverges at Dirac point ( $n \rightarrow 0$ ),
2. the graphene resistivity  $\rho_{xx}$  doesn't depend on magnetic field.

The simple Drude description (with one-type of carriers) doesn't explain observed at room temperature magnetoresistance ( $\rho_{xx} = \rho_{xx}(B)$ , in Fig. 1.15).

As presented in the previous sections, at room temperature in extrinsic graphene the transport around the Dirac point cannot be explained just by one type of carrier system, as the concentrations of both holes and electrons is of comparable level. The situation is different away from the Dirac point (in the so called *metallic regime*), where the number of minority carriers is orders of magnitude smaller and system can be considered as one-type only. In that range Drude model can be used for description of charge transport.

## 2.4 Resistivity in ideal graphene and graphene with puddles.

In this section I analyse the properties of derived expressions of resistivities and their behaviour at different parameters range. I compare the resistivities of ideal graphene and of graphene with puddles at room temperature using 2-type-carrier description (Eq. 2.12 and Eq. 2.13). The free parameters in the model are: mobility  $\mu$  and broadening of the puddles  $\sigma$ . I assume that the mobility is constant and doesn't depend on charge carriers concentration. This is just rough approximation, because different scattering mechanisms dominate at different charge concentrations and it is not trivial issue how they modify the value of mobility. The value for mobility is taken in correspondence with the experimental findings in metallic regime (there the typical values range from 2000 to 20 000  $cm^2/Vs$ ).

The longitudinal resistivity  $\rho_{xx}$  as a function of magnetic field at different gate voltages is presented in Fig. 2.9. We can recognise there positive magnetoresistance effects (the increase of resistance with the increase of magnetic field), which is most pronounced in the vicinity of CNT. Away from it, in metallic regime,  $\rho_{xx}$  is constant like in the predictions from the Drude model.

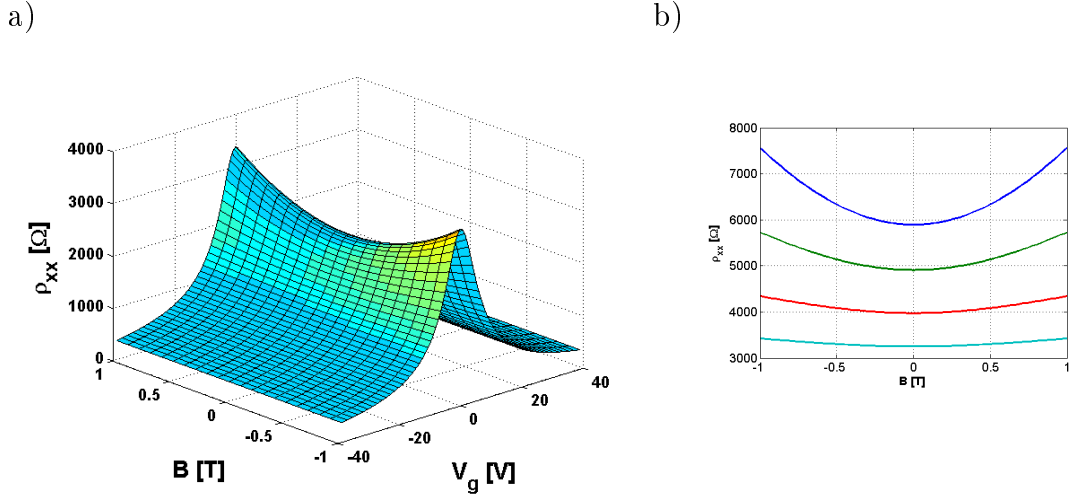


**Figure 2.9:** Longitudinal resistivity  $\rho_{xx}$  in ideal graphene as a function of magnetic field and gate voltage, at room temperature (a). The same data, but projected on  $(B, \rho_{xx})$  are presented in (b). The voltage sequence (from top curve to bottom) is -1, -2, -3, -4 V. The curves are calculated according to the formula in Eq. 2.12 with constant mobility  $\mu = 6000 \text{cm}^2/\text{Vs}$ .

The transverse resistivity  $\rho_{xy}$  for ideal graphene at room temperature is presented in Fig. 2.10. From definition it is proportional to the Hall coefficient  $R_H$  and inversely proportional to the difference in number of charge carriers ( $n - p$ ). As  $\rho_{xy}$  at the Dirac point crosses zero, the number of electrons and holes is equal in the system. The resistivity doesn't diverge at the Dirac point, due to the presence of finite carrier concentration ( $n \neq 0$ ).

The influence from puddles can be seen in Fig. 2.11 where I present comparison between the resistivity in ideal graphene and in graphene with puddles. The puddles broaden the curve of resistivities and lower their maximum value, but qualitatively the shape of the curve remain the same.

Now, let us analyse the influence of the mobility  $\mu$  on the modelled resistivity  $\rho_{xx}$ . For simplicity, I set the broadening to zero,  $\sigma = 0 \text{ eV}$ . The computed curves for different  $\mu$  presents Fig.2.12. We can observe that the larger mobility, the smaller maximum of resistivity  $\rho_{xx,max}$ .

In our model the mobility is constant and independent from the broadening. However, in real systems mobility is also influenced by the potential fluctuations, simply described by  $\sigma$ . Reducing these fluctuations means increasing mobility. The relation between mobility and potential fluctuations is not trivial and is not covered by this model, where both  $\mu$  and  $\sigma$  enters as a free, independent parameters.

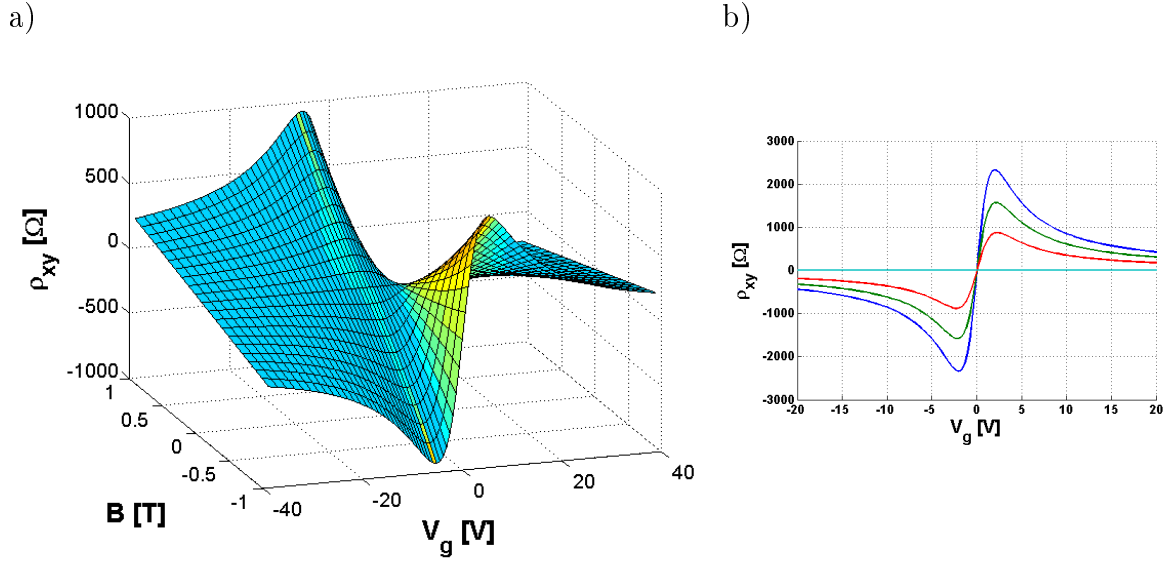


**Figure 2.10:** Transversal resistivity  $\rho_{xy}$  in ideal graphene as a function of magnetic field and gate voltage, at room temperature (a). The same data, but projected on  $(B, \rho_{xy})$  space are presented in (b). The magnetic field sequence (from the top blue curve to the red bottom) is -1, -0.72, -0.42, 0 T). The curves are calculated according to the Eq. 2.13, with constant mobility  $\mu = 6000\text{cm}^2/\text{Vs}$ .

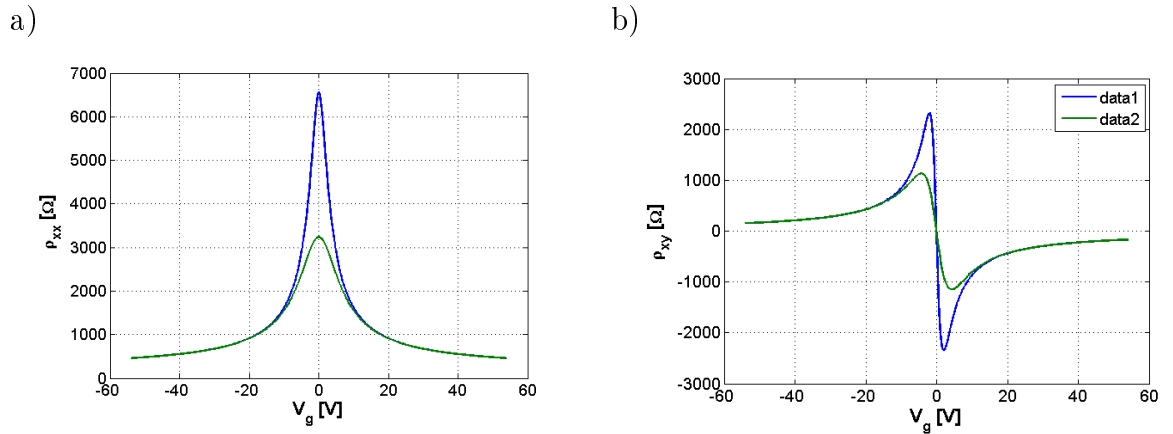


**Figure 2.11:** Comparison of the resistivities:  $\rho_{xx}$  in (a) and  $\rho_{xy}$  in (b) of ideal graphene (blue curves) and of graphene with puddles (green curves). The curves are calculated according to the Eq. 2.12 and 2.13 (at  $B=1\text{T}$ ), with the constant mobility,  $\mu = 6000\text{cm}^2/\text{Vs}$ . The Gaussian broadening of puddles is  $\sigma = 50\text{meV}$ .

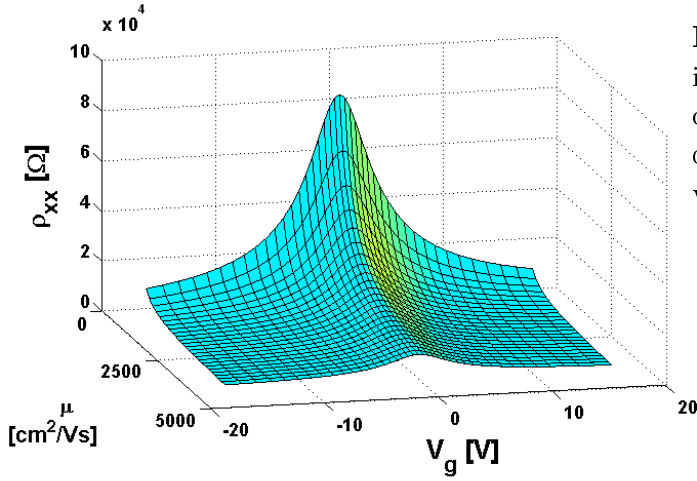


**Figure 2.12:** Resistivity  $\rho_{xx}$  in ideal graphene vs gate voltage at different mobilities. With the increase of the mobility the resistivity pick goes down.

The broadening  $\sigma$ , which represents all kind fluctuations of the electric potential (due to the substrate, adsorbed molecules etc.) can serve as an indication of the quality of the graphene flake. In the model, the value of the broadening have direct relation to the distance between deflection points  $\Delta_{defl.points}$  of the resistivity  $\rho_{xx}$  vs gate voltage. We calculate  $\Delta_{defl.points}$  as a voltage difference between maximum and minimum of numerical first derivative of resistance  $d\rho_{xx}/dV_g$ . The resistivity  $\rho_{xx}$  and its differential versus gate voltage  $V_g$ , with the clear maximum and minimum are plotted in Fig. 2.13. The distance between deflection points  $\Delta_{defl.points}$  can be easily obtained from experimental measurements of  $\rho_{xx}$ . The relation between  $\Delta_{defl.points}$  and  $\sigma$  in the model, plotted in Fig. 2.14, can be used to determine the value of free parameter  $\sigma$ .

The dependence of both: the mobility and the broadening on the maximum of resistivity  $\rho_{xx,max}$  presents Fig. 2.15. The smaller is the broadening  $\sigma$ , the higher is the maximum of resistivity  $\rho_{xx}$  while it decreases with the rise of mobility. This indicates competing influence between  $\mu$  and  $\sigma$  on the value of the resistivity maximum. The dependence of both: mobility and broadening on the the distance between deflection points is plotted in Fig. 2.16. Suprisingly  $\Delta_{defl.points}$  doesn't change with the change of mobility, as one may expect looking at Fig. 2.12, where the increase of mobility flattens the shape of  $\rho_{xx}$ . The relation between  $\sigma$  and  $\Delta_{defl.points}$  from Fig. 2.14 holds for all mobility values. Therefore it can be determined independently from the fitting procedure for  $\mu$ .

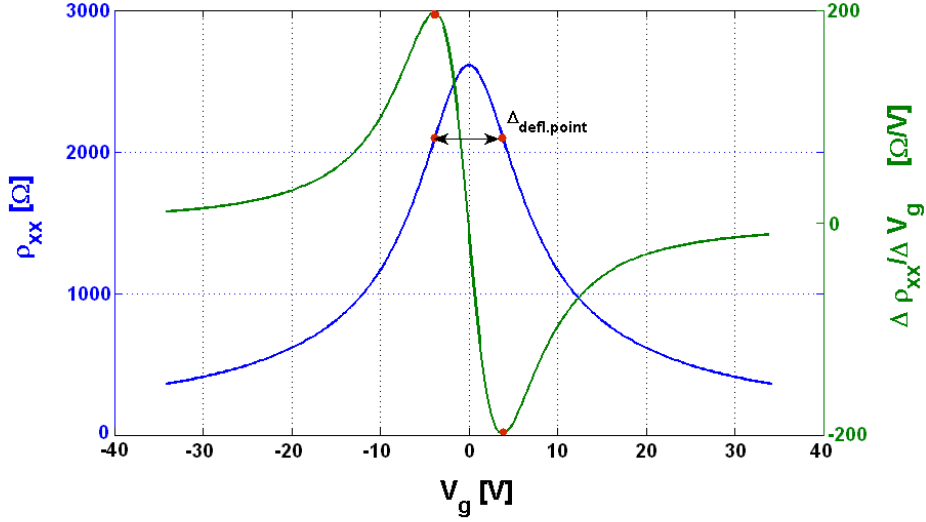


**Figure 2.13:** Resistivity  $\rho_{xx}$  and its differential ( $\Delta\rho_{xx}/\Delta V_g$ ) versus gate voltage  $V_g$ . The red points indicate position of maximum and minimum of the differential resistivity curve and corresponding deflection points of the resistivity curve. The distance between deflection points  $\Delta_{defl.points}$  is marked with an double arrow. The curves are calculated for  $\sigma = 50meV$ ,  $\mu = 7000 cm^2/Vs$ .

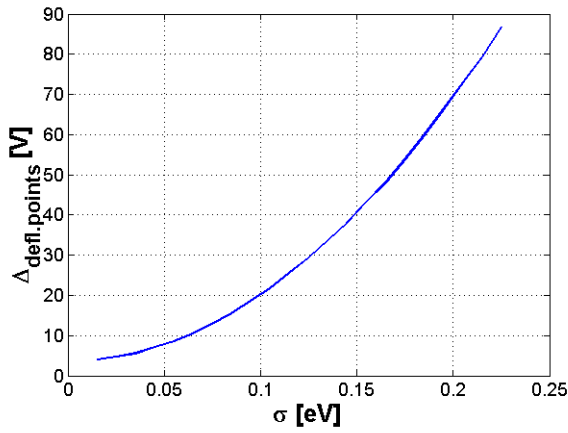


**Figure 2.14:** A relation between the broadening and the voltage distance between deflection points in modelled curves of the resistivity  $\rho_{xx}(V_g)$ .

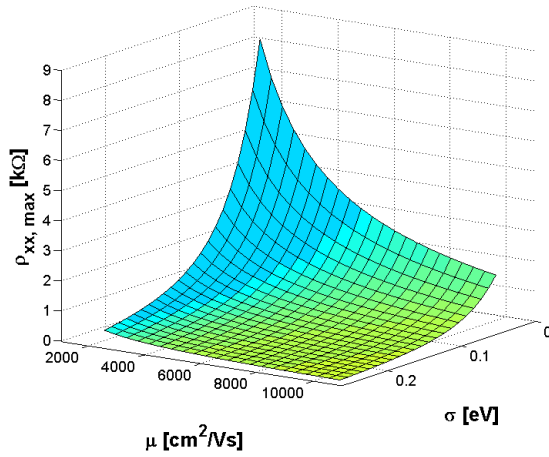


**Figure 2.15:** Maximum of resistivity  $\rho_{xx}$  as a function of the puddles broadening  $\sigma$  and the mobility. With increasing the mobility the resistivity pick goes down. With the increase of the puddles broadening the resistivity pick also goes down.

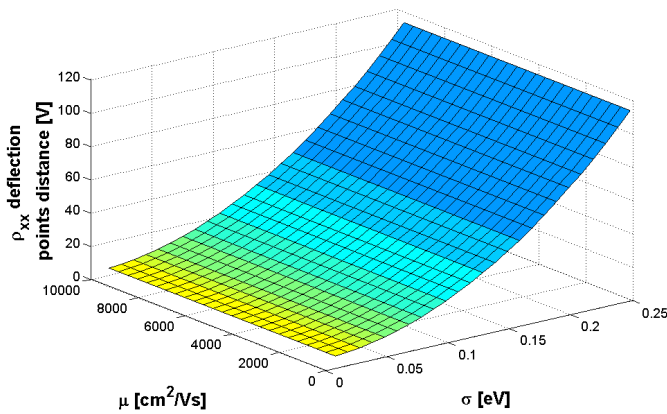


**Figure 2.16:** Distance between deflection points of  $\rho_{xx}$  as a function of broadening  $\sigma$  and mobility  $\mu$ . The distance between deflection points doesn't change with the increase of mobility and depends only on broadening  $\sigma$ .



## Chapter 3

---

# Device preparation and measurement setup

The aim of this thesis was to investigate the magnetoresistance and Hall effect in graphene. In this chapter I present the procedure of device preparation, pointing out the problems I encountered during it. At the beginning I give a brief description of different types of graphite, used to obtain graphene flakes. The deposition technique - micromechanical cleavage of graphite on  $\text{SiO}_2$  - produces not only single layer graphene flakes but also multilayered ones. Therefore, the crucial step is a verification of the number of layers of deposited flakes. The rough mapping and selection of suspicious flakes is done with the use of optical microscope. The suspected monolayer graphenes are confirmed by atomic force microscopy (AFM), where we can determine the number of layers and geometrical shape of the flake. Later on I present the procedure of contacts deposition and structuring the flake by oxygen plasma etching. The shaping of graphene with plasma etching leaves lots of contamination possibly from burned carbon. Therefore I applied additional cleaning procedure: annealing under  $\text{Ar}/\text{H}_2$  gas flow. With AFM I investigate the surface roughness of graphene and of  $\text{SiO}_2$  at different stages of device preparation. In the last section I present the measurement setup and measurement scheme for device characterisation.

### 3.1 Deposition of Kish graphite

The first and still the most common method of graphene deposition on a  $\text{Si}/\text{SiO}_2$  wafer is mechanical exfoliation. In there we mechanically rub off one layer from the bulk graphite. For this purpose we can use one of the graphites available commercially: natural graphite, Highly Oriented Pyrolytic Graphite (HOPG) and Kish graphite. Natural graphite is available in form of amorphous powder with graphitic flakes usually small in size (typically less than 0.1 mm). It contains many defects, dislocations and chemical impurities such as Fe, Ni, Mn, Cu (typically few  $\mu\text{g}$  per 1g of graphite, after [37]), which can affect charge transport. A better choice for studies of graphene is HOPG. HOPG is prepared by the pyrolysis of hydrocarbons at temperatures above  $2000^\circ\text{C}$ . The resulting pyrolytic carbon is subsequently heated to improve crystalline order. HOPG has a very high crystal quality, high chemical purity and is sold in large solid pieces of typical size  $10\text{mm}\times 10\text{mm}$ . The third type, Kish graphite, was firstly obtained during steelmaking procedure. It is a by-product, skimmed from the sides of carbon-rich molten iron feed. After an on site recycling

of iron, what is left is a mixture of graphite and slag. Further many purification steps lead to the final high quality graphite (with almost none metal impurities,  $<0.5 \text{ mug/g}$ , after [37]). It has a form of graphitic flakes which are much larger in size than the natural graphite flakes (typically around 1mm). As in our group we aim at graphene with the highest quality (the least of possible impurities correspond to better electronic performance) we use HOPG or Kish graphite. In this thesis, all presented measurements are for samples out of Kish graphite.

Before deposition of graphene, we firstly prepare golden markers on the  $\text{SiO}_2/\text{Si}(n++)$  substrate and the back gate electrode (also made of gold). These markers serve for the determination of the flake's coordinates and are alignment points for electron beam lithography. After deposition of markers the wafer is put into reactive ion plasma etcher and exposed to oxygen plasma for 5 min. at power 100W to remove all organic contaminants from the wafer (especially residues of PMMA left after preparation of markers). Deposition of graphene on silicon dioxide substrate is done by mechanical exfoliation, using the scotch tape (for details see [28]). This deposition technique produces not only single layer graphene flakes but also multilayered ones. Therefore, we use optical microscopy to select the candidates for graphene single layer. Remarkably, with a proper choice of  $\text{SiO}_2$  thickness [17], a single layer of graphene resting on a  $\text{SiO}_2/\text{Si}(n++)$  substrate can be visible. The contrast difference is calculated to be larger for 300nm layer of  $\text{SiO}_2$  than for 500nm (contrast  $C$  is defined as the relative difference in reflected light intensity  $R$ , from substrate without graphene ( $R_{\text{SiO}_2}$ ) and with graphene ( $R_{\text{graph.}}$ ), by formula:  $C = (R_{\text{SiO}_2} - R_{\text{graph.}})/R_{\text{graph.}}$ . It gives  $C=0.05$  for 300nm  $\text{SiO}_2$  and  $C= 0.04$  for 500nm  $\text{SiO}_2$  [36]). Because of that in our experiments we use the wafers with  $\text{SiO}_2$  thickness 300nm. Optical microscopy enables to select the potential monolayer candidates, while presence of gold markers enables for its precise location. Having the precise positions of the flake, we can easily find it back under Atomic Force Microscope (AFM), with which we can determine the layer thickness in order to confirm wheather the flake is a single layer graphene. For that we use AFM Digital Instrument Nanoscope IVa in tapping mode, with maximum scan window:  $15.7 \mu\text{m}$ . All pictures were taken at resolution:  $512 \times 512$ . The distance between graphene planes in bulk graphite is 0.335 nm, but when a single layer is deposited on  $\text{SiO}_2$  one may expect increase of its step height due to the presence of water layer, immediately caught by a highly hygroscopic silica just before graphene exfoliation. Various groups report the stepheight between graphene and  $\text{SiO}_2$  ranging from 0.35 to 1.6 nm. This scattering of the reported values may also (as it was shown by [39]) originate from improper choice of measurement parameters of AFM (especially crucial is the choice of free amplitude of tapping cantilever, which may lead to increase of stepheight value of as much as 1 nm). The most reliable AFM measurements of graphene thickness can be obtained from folded regions, where investigated layer folds back onto itself. There we can measure a stepheight of two graphene layers on top of each other. However such folded regions are not always available. An example of the stepheight analysis is presented in Fig. 3.1.

The AFM imaging is used not only for a determination of the graphene flake

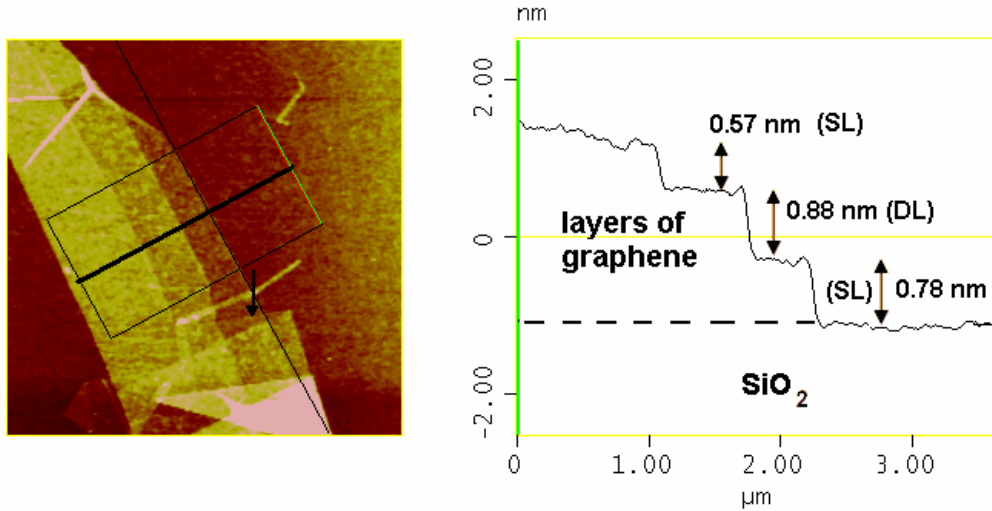


**Figure 3.1:** Stepheight measurements of graphene in tapping mode AFM. The height is recorded along the thick black line (a). The first step is addressed to the single layer (labelled SL), the second to the double layer (DL) and the third to the single layer. We claim that the bottom layer is single by reference to the additional folded layer below the black rectangular (marked with an arrow). The step height between  $\text{SiO}_2$  and the graphene is 0.8nm, while the step height at graphene bottom layer is 0.38nm.

thickness but also to measure its shape coordinates with respect to markers. These coordinates enable to align the metal contacts in the lithography step, with accuracy below 100nm.

The size of graphene flakes obtained from Kish graphite are much larger (up to tens of  $\mu\text{m}$  in size) comparing to the one obtained from HOPG. However, the larger the size, the bigger the tendency for the flake to fold during the device preparation. The flake can fold while spinning the polymer resist (the spreading polymer can drag the folded parts further with adhesion forces), when immersing in acetone or during ultrasonication. An example of this effect is presented in Fig. 3.2, where the flakes rolled up after dipping in acetone. A tendency of graphene to fold can be explained by many factors (strength of adhesion after deposition, the substrate local roughness, the shape of individual graphite flake, the type of terminating atoms) which are beyond the control of deposition technique. As the folding occurs irregularly, for safety, we tried to avoid any extra cleaning procedures before placing the metal contacts on the device.

## 3.2 Preparation of the device

For magnetoresistance and Hall effect studies in graphene we need to contact the flake in the double Hall bar geometry, so that we could measure the longitudinal

resistivity  $\rho_{xx}$  and transversal resistivity  $\rho_{xy}$  at the same flake, see Fig. 3.3(a). The measured resistance  $R_{xx}$  is converted to the 2-dimensional resistivity  $\rho_{xx}$  using the concept of a sheet (square) resistance. In a regular 3-dimensional conductor, the resistance can be written as

$$R = \rho \frac{L}{A} = \rho \frac{L}{Wt}$$

where  $\rho$  is the resistivity,  $A$  is the cross-sectional area and  $L$  is the length of resistor. The cross-sectional area can be split into the width  $W$  and the sheet thickness  $t$ . By grouping the resistivity with the thickness, the resistance can be written as:

$$R = \frac{\rho}{t} \frac{L}{W} = \rho_s \frac{L}{W} \quad (3.1)$$

where  $\rho_s$  is the sheet (square) resistance. The units of sheet resistance are ohms or more precisely "ohms per square" ( $\Omega/\square$ ). Further on I skip the subscript "s" as whenever talking about resistivity  $\rho_{xx}$  in graphene, I will always refer to the sheet resistivity. From above it is clear that for quantitative measurements, one needs to determine the scaling factor  $L/W$ . In Hall bar geometry however, the current path is ambiguous because the current can go not only through the central graphene channel but also through the side contacts (as they have lower resistivity), see Fig. 3.3(a). To suppress this effect, one etches the graphene channel, so that the current cannot easily reach the side contacts and its path becomes well defined, see Fig. 3.3(b).

In the following subsections I firstly present the fabrication of metal contacts and later on the etching procedure, with the use of electron beam lithography.

### 3.2.1 Deposition of gold contacts

The crucial procedure in fabrication of graphene device is preparation of the contacts to the flake. For that we use electron beam lithography (EBL), which enables us to design the individual contact pattern for any shape of the flake at any place of the wafer. The primary advantage of electron beam lithography over optical lithography is that it makes the fabrication of nanometer features possible.

The presented below fabrication procedure follows the standard recipe used in our group. Firstly, the sample have to be covered with an electron-beam resist. In our case we use polymethylmethacrylate (PMMA) which is an ultra-high resolution (down to 20nm) positive resist commonly used for nanolithography. Before deposition of polymer, we bake the sample for approximately 5 min. in the oven at  $170^\circ$  to remove water from the  $\text{SiO}_2$  surface and improve adhesion of PMMA. Next, we spin the PMMA (with molecular weight 950k, 2% dissolved in anisole) at the 4000 rate per minute (rpm) for 60 seconds. This produces approximately 70 nm thick resist layer. We briefly check the homogeneity of the spun polymer layer under the optical microscope. In some rare cases polymer may not stick to some areas of the wafer. If these parts are important for the device preparation, we remove the PMMA in

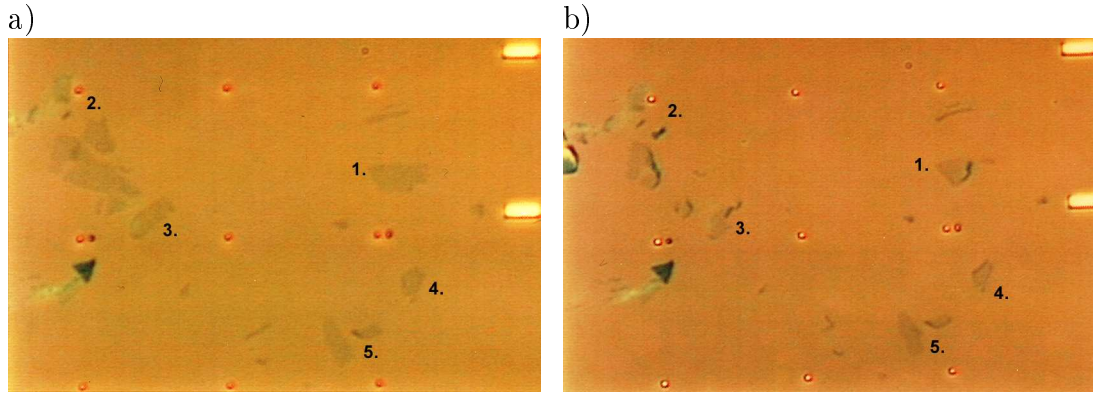


**Figure 3.2:** Folding of graphene under acetone treatment. The optical image before immersing sample in acetone (a) and after (b). To make the comparison easier, the same areas and flakes carry the same numbers on both pictures, (a) and (b).

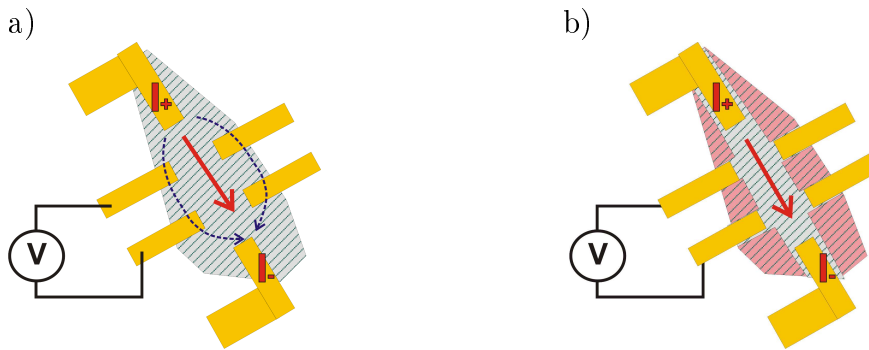


**Figure 3.3:** A Hall bar geometry of graphene device with the indicated voltage drop for  $\rho_{xx}$  measurements. In (a) the current goes not only through the middle channel but also through the side contacts (as they have lower resistivity), which leads to ambiguity of the current path and choice of scaling factor  $W/L$  for graphene square resistance. To suppress this effect, we can etch the graphene channel, so that the current path is well defined (b).

warm acetone and repeat the procedure. After the resist is spincoated, we bake the sample for 1 hour in the oven at  $170^\circ$  to harden the resist. This backing makes sure that anisole, in which PMMA is dissolved, evaporates and dry PMMA is left.

The design of contacts is divided into two parts: the small and big pattern, as we use two writing fields ( $300\mu\text{m}$  by  $300\mu\text{m}$  and  $2400\mu\text{m}$  by  $2400\mu\text{m}$ ). The small pattern contacts directly graphene flake, while the big pattern connects the small contacts with contact pads, further used for bonding.

The small contacts are exposed with the dose factor  $(1-1.2)\times 100\mu\text{C}/\text{cm}^2$  and big contacts with the dose  $2.0\times 100\mu\text{C}/\text{cm}^2$ . The beam acceleration voltage is 10kV. The exposure of PMMA to intense electron beam causes scission of the polymer chains. The exposed (lighter molecular weight) resist is then developed in a solvent developer. A high dose intensify fragmentation of PMMA. However, at higher doses the electrons can be multiply scattered and penetrate through the photoresist away from desired exposure parts (producing so called undercut). As a result the exposed area is much larger than the one defined by the designed pattern. This process is to some extent desirable, as it helps in lift-off procedure, but can also merge small contacts patterns. Due to that reason for the dose factor  $(1-1.2)\times 100\mu\text{C}/\text{cm}^2$  the space between contacts of 500nm and more was kept for safety.

After the exposure we develop PMMA in the mixture of methyl isobutyl ketone (MIBK) and iso-propanol (IPA) in ratio 1:3 for 60 seconds at  $T \approx 20^\circ\text{C}$ . We use the mixture because the alone MIBK is too strong developer, and may develop also unexposed areas. To stop further development we rinse the sample in IPA solution for 15-30 seconds. After development the exposed pattern can be seen under optical microscope, so that we can verify the alignment of the contact patterns with respect to graphene. In case of wrong alignment we can clean the resist in warm acetone, which dissolve both the exposed and unexposed PMMA (for  $>10$  min.). Then the entire procedure is repeated. One should however keep in mind that the more lithography steps are done, the more polymer residues are left on the graphene surface, which may result in high resistive contacts (hundreds of  $\text{k}\Omega$ , comparing to few  $\text{k}\Omega$ ).

Next step is a deposition of gold contacts with the use of electron beam evaporator in the vacuum of  $p \approx 10^{-6}$  mbar. The electron beam heats up the target material, which starts evaporating. As a result our sample is covered with a thin layer of metal with desired thickness. To improve the adhesion of Gold to the silica substrate, a thin layer of Titanium ( $\sim 3 \div 5$  nm) is deposited first and then a gold layer of set thickness is deposited afterwards. The evaporation rates and deposited thicknesses are following: Ti: 0.15nm/s, 3nm; Au: 0.2nm/s, 35 nm. After evaporation the whole front surface is covered with metal. To remove unwanted metal parts we perform a *lift-off* process. We dip the sample in warm acetone ( $\sim 45^\circ\text{C}$ ) for few minutes. Acetone penetrates under the metal layer due to the height differences between the resist and deposited materials (the film must be thin enough to allow the solvent to penetrate underneath, that is why the thickness of resist is

always larger than the thickness of evaporated material). The resist under the film is removed with acetone, taking the metal film with it, and leaving behind only the metal parts deposited directly on the substrate, see Fig. 3.4(a). In my case, sometimes the lift-off procedure didn't remove all the metal parts between the contacts, see Fig. 3.4(b). The reasons for that can be that the resist below the metal parts could not have been dissolved properly or that the metal has attached so well to the contacts that it prevented the lift-off. We can try to improve lift-off by leaving the sample in acetone for few hours or by ultrasonication (at lowest power for few seconds, but we risk losing the contacts or breaking graphene apart).

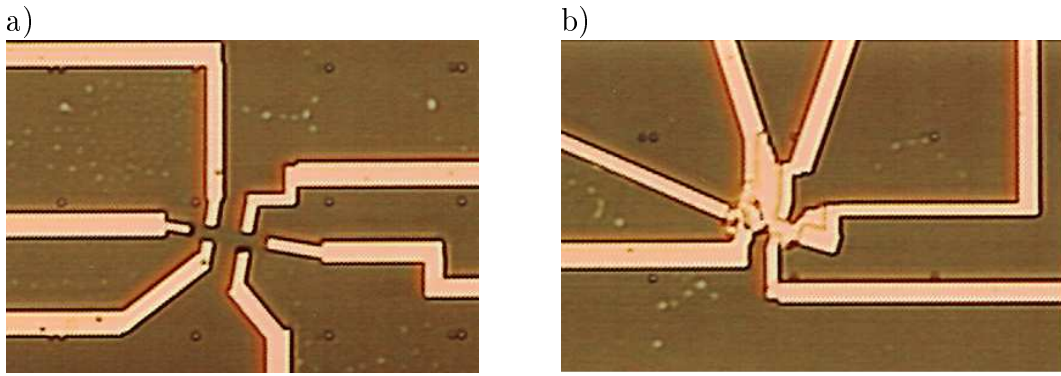


**Figure 3.4:** Optical image after the lift-off procedure for two devices: (a) with successful lift-off and (b) with partial lift-off.

There are few improvements which can be done to ensure full lift-off. First is reduction of the metal layer thickness (with this we don't want to go below 30 nm, as the thinner the contact, the easier it breaks). Second is the use of thicker resist.

### 3.2.2 Shaping graphene: oxygen plasma etching.

As it was mentioned, for Hall measurements we wanted to shape the flake in the Hall bar geometry (see Fig. 3.3(b)). This can be done by the etching with ion plasma. Like in the case of contact pattern, the pattern of etch mask is firstly prepared in PMMA with EBL technique. The dose factor for exposed pattern was  $3.5 \times 100 \mu C / cm^2$  with the beam acceleration voltage 30kV. After development, the sample is placed in reactive ion etcher (RIE), where it is etched with oxygen plasma for 20s. at the power of 40W. The sample is bombarded with oxygen ions and graphene in polymer free windows is destroyed, leaving many carbon burns. These contaminants spread not only in the etched window but also in some distance around and remain there even after dissolving the polymer. These leftovers are highly undesirable as they can act as molecular dopants and scattering centers. In the case, when gold is placed on graphene after etching, the leftovers can lead to high contact resistances. In our group was shown that after etching graphene with argon (at similar RIE conditions) the layer of resist turns into some glossy state, which cannot be dissolved with warm acetone [38]. Although the similar behaviour was

not observed in oxygen plasma, it gives suggestion that etching produces a lot of contamination, also on the areas protected by the resist, which remains at the surface after warm acetone cleaning. After etching the additional cleaning procedure to remove the left contamination was performed. In it the sample is placed into oven with a steady gas flow of mixture Ar/H<sub>2</sub> in ambient conditions. We anneal at the temperature of 340°C for 3 hours. The influence of this cleaning procedure on surface roughness was studied in details in [28].

Let us compare surface roughness of graphene, etched areas and SiO<sub>2</sub> substrate with AFM at different stages of cleaning procedure. We chose three different graphene flakes from the same sample (Fig. 3.5). The surface roughnesses of the areas in white rectangles in Fig. 3.5 are shown in Table 3.1.

**Table 3.1** : Surface roughness at different stages of sample preparation for 3 different regions in Fig. 3.5, white table cells correspond to Fig. 3.5(I.a, II.a, III.a), light gray to Fig. 3.5(I.b, II.b, III.b), and grey to Fig. 3.5(I.c, II.c, III.c).

<b>rms</b>	graphene	etched window	SiO <sub>2</sub>
before etching	0.37 nm	-	0.26 nm
	0.30 nm	-	0.27 nm
	0.24 nm	-	0.18 nm
after etching / acetone cleaning	1.1 nm	2.5 nm	1.04 nm
	0.64 nm	3.6 nm	0.6 nm
	2.2 nm	-	2.7 nm
after etching / Ar/H <sub>2</sub> cleaning	0.36 nm	1.34 nm	0.23 nm
	0.62 nm	3.1 nm	0.4 nm
	0.22 nm	-	0.18 nm

For chosen devices the graphene surface roughness is slightly bigger than the roughness of SiO<sub>2</sub>. Normally, stiff graphene layer has smaller surface roughness than the substrate (see [28]). This discrepancy indicates that, particularly, Kish graphene studied here has initially a lot of structural corrugations. After etching and removing the resist with the warm acetone, the surface roughness of all studied areas increased. This is expected for the regions around etching windows, as etching burns carbon (Fig. 3.5 (II.a) and (II.b)). However, the SiO<sub>2</sub> regions away from etched areas (Fig. 3.5(II.a), (II.b), white side squares) or graphene and SiO<sub>2</sub> at non-etched region (Fig. 3.5 (II.c)), also show the increase in the surface roughness. The occurrence of polymer contaminants' texture there can be easily recognised on AFM images (Fig. 3.5(c), middle). This texture is removed with Ar/H<sub>2</sub> annealing. After this cleaning step the surface roughness of all studied areas decreased, but not always to the initial value. This is because some contamination introduced by etching remain attached even after the additional cleaning procedure. From above it is clear that when the etching of graphene is performed, the cleaning with warm

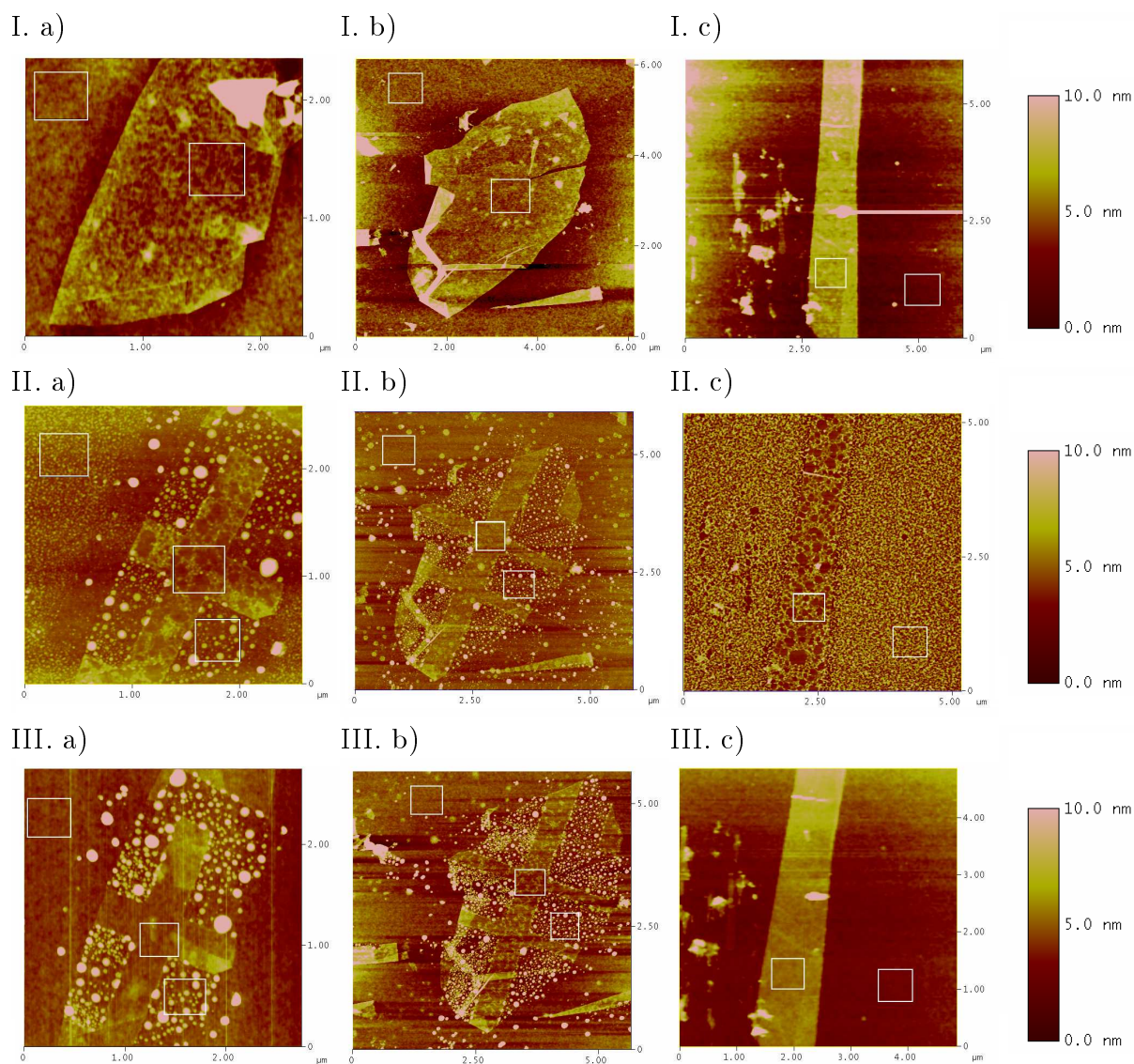


**Figure 3.5:** AFM images for 3 different graphene regions (a), (b) and (c) at different cleaning stages. Images before etching are labelled with number I, images after etching and acetone cleaning are labelled with number II, images after etching and cleaning in Ar/H<sub>2</sub> are labelled with number III. Region (c) was not etched and lied in far distance from etching areas (~1mm).

acetone is not efficient (many adsorbates remain on graphene) and Ar/H<sub>2</sub> annealing is quite essential.

### 3.3 Measurement setup

The objective of this thesis is an investigation of the charge transport properties in graphene. For this I deposited graphene flakes on Si/SiO<sub>2</sub> wafer, etched graphene into Hall bar shape and contacted it. Next, the sample was placed into a chip carrier. The bottom part of the sample (the back side, covered with gold) was glued to the metal base of chip carrier with conducting silver paint (ACHESON ELECTRODAG 1415M). The back gate and graphene contacts were bonded to the chip pins with the aluminium bonding wires. Further on, the chip carrier with the sample was placed in the chip holder. The holder was mounted in the vacuum can, so that I could perform the measurements also in the vacuum,  $p \sim 2 \times 10^{-6}$  mbar. This holder is also equipped with the heater. By heating we can remove the adsorbed water molecules as well as some additional contamination from the graphene surface, restoring the Dirac point toward zero gate voltages). In the experiment I heated up to 250°C. The other side of the holder is connected to the switchbox, equipped with 16 toggles through which we can open and close the circuit for individual contacts. In the passive state all connections are grounded to prevent the uncontrolled charge flowing through the device. The switchbox contains filters (Pi-filters,  $R_f = 1k\Omega$ ,  $C_f = 10nF$ ), which reduce the picked up noise and cut out high frequency and high amplitude voltage spikes from the network. All electric measurements are performed with current of nano- and microampers.

A source of alternating current (AC) of sinusoidal shape is supplied by IV-measurement box. The IV current is controlled by a lock-in amplifier (Stanford Research Systems SR830), by sending the AC voltage to the IV-box. Lock-in amplifier tune the amplitude and frequency of the current generated by IV-box in the range from several pA up to 1 mA. The IV box also detects the voltage drop between the contacts, amplifies it and sends it to lock-in amplifier, where the signal is extracted and measured. For the best performance of the amplifier (the highest sensitivity and low signal to noise ratio) a reference signal at the same frequency is provided. This is done by splitting the signal from IV box into 2 channels, one to switchbox and one to amplifier (as a reference). Amplifier records amplitude of voltage drop at selected frequency and phase difference between detected and reference signal. Lock-in amplifier can measure both in-phase (X) and out-of-phase (Y) components of the signal. In resistance measurements we are interested only in X component.

In case, when the measurements didn't show substantial phase shift ( $0 \div 10^\circ$ ) I performed measurements on frequency around 17Hz and time delay: 1s. I avoided setting the exact frequency value, due to a possible interference of the signal with other electronic equipment and an increase of the noise level. The time delay is the

time during which amplifier integrates the received signal, and should be at least 3 times larger than the period of the signal  $T$ . In case when the signal is out of phase ( $>10^\circ$ ) I reduced the frequency (as this also reduces the out-of-phase Y component). When this was the case I typically measured at frequency  $\omega = 2\text{Hz}$  with the time delay  $t = 3s$ .

The switchbox is also connected to the voltage source (Kethley 6517A), which connects the gate of our sample.

As I wanted to study the influence of magnetic field on resistance, the sample holder was placed between poles of the electromagnet (GMW, model 5403). The coils can be supplied with the current up to 70A, which corresponds to  $\sim 1.5T$ . In the range between 0 and 30A the dependence between the current  $I$  in coils and produced magnetic field  $B$  is linear, according to the relation  $B = 22.6 \cdot I$ , the coefficient is expressed in [mT/A], for the spacing between poles 34mm. Above this range the linear relation no longer holds, and I used the calibration curve from electromagnet specification.

The most important settings in the measurement setup can be controlled by computer with the aid of LabView script (written by Dr. Mihai Popinciuc). It involves recording the amplitude and the phase of detected signal, the gate voltage, the current delivered to electromagnet. The scheme of the measurement setup is presented in Fig. 3.6

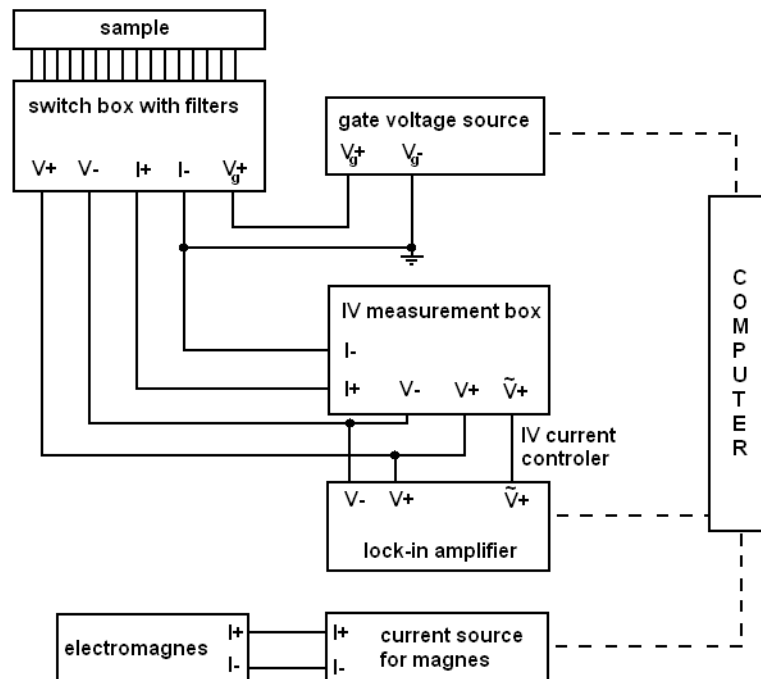


**Figure 3.6:** Scheme of the measurement setup.

We start electrical characterisation of the device from 2 point measurements,

where the current is sent through the contacts (a and b), filters and graphene and the voltage drop is measured at the same circuit elements (scheme of the circuit is presented in Fig. 3.7). The measured resistance:

$$R_{meas} = R_a + R_f + R_{graphene} + R_b + R_f.$$

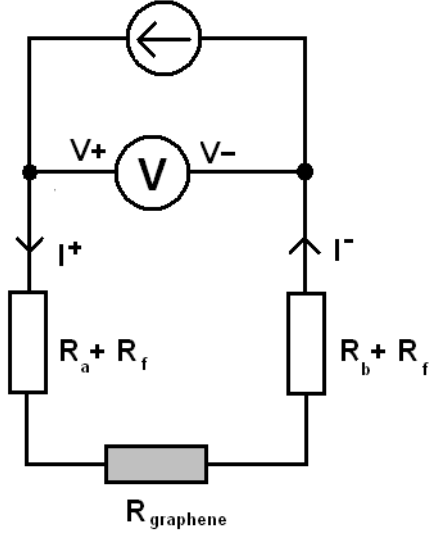


**Figure 3.7:** A scheme of the 2 point measurements configuration. The measured resistance:

$$R_{meas} = R_a + R_f + R_{graphene} + R_b + R_f.$$

Further we measure resistance in 3 point configuration, where the current is sent through the contact  $a$  ( $I+$ ) and  $b$  ( $I-$ ) and the voltage drop is measured between the contact  $a$  ( $V+$ ) and  $c$  ( $V-$ ), as depicted in Fig. 3.8. The measured resistance:  $R_{meas} = R_a + R_f + R_{graphene}$ . The single contact resistance can be isolated by subtracting  $R_{graphene}$ . In practice, we expect the graphene resistance  $R_{graphene} < 10k\Omega$ , therefore even without knowing  $R_{graphene}$  the 3 point measurements gives a rough indication of the contact quality.

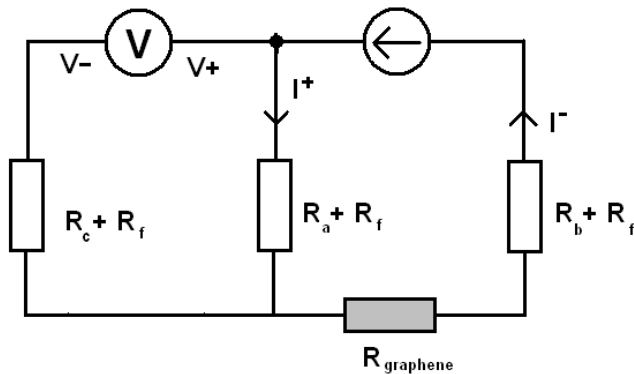


**Figure 3.8:** A scheme of the 3 point measurements configuration. The measured resistance:

$$R_{meas} = R_a + R_f + R_{graphene}.$$

Finally with the 4 point configuration we eliminate the contact resistance from measurements. The current is sent through the contact  $a$  ( $I+$ ) and  $b$  ( $I-$ ) and the voltage drop is measured between  $c$  ( $V+$ ) and  $d$  ( $V-$ ), as depicted in Fig. 3.9. The measured resistance is only the graphene resistance:  $R_{meas} = R_{graphene}$ .

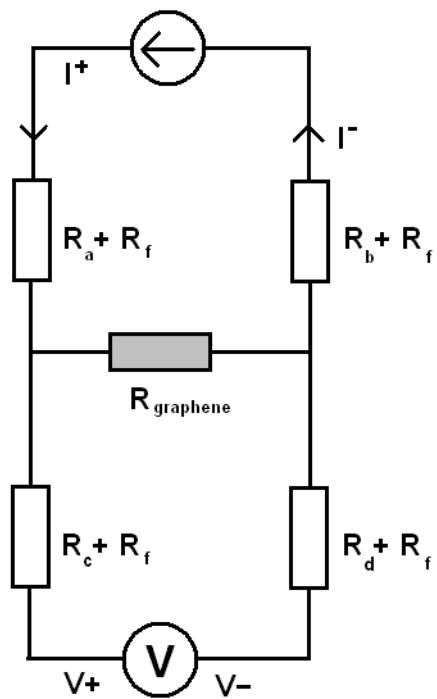


**Figure 3.9:** A scheme of the 4 point measurements configuration. The measured resistance:  $R_{meas} = R_{\text{graphene}}$ .



## Experimental part

### 4.1 The influence of device preparation on contact resistance

Graphene was obtained from Kish graphite by mechanical exfoliation on 300nm SiO<sub>2</sub> over doped Si (n++) and connected with Ti/Au electrodes defined by electron-beam lithography. For structuring the flake shape I used oxygen plasma etching and explored the annealing in Ar/H<sub>2</sub> gas flow. In Chapter 3 I investigated the influence of etching and annealing on surface roughness of graphene and SiO<sub>2</sub>. The contamination after lithography/etching steps may also affect the resistance of contacts, if one deposits the contacts afterwards. To verify this influence I studied the contact resistances for devices prepared in 4 different ways:

1. deposition of contacts without plasma etching
2. plasma etching followed by deposition of contacts
3. plasma etching followed by Ar/H<sub>2</sub> annealing, and deposition of contacts afterwards
4. deposition of contacts followed by plasma etching and Ar/H<sub>2</sub> annealing

The contact resistance was measured in 3-probe configuration. The obtained range of resistance values are shown in the table 4.1, each of them was measured on one device with 5 contacts.

**Table 4.1** : Contact resistance range for different preparation strategies.

number	Preparation sequence	contact resistance range [k $\Omega$ ]
1.	deposition of contacts, no etching	1.5 $\div$ 5
2.	plasma etching $\Rightarrow$ deposition of contacts	130 $\div$ 1200
3.	etching $\Rightarrow$ annealing at Ar/H <sub>2</sub> gas flow $\Rightarrow$ deposition of contacts	1.8 $\div$ 70
4.	deposition of contacts $\Rightarrow$ etching $\Rightarrow$ annealing at Ar/H <sub>2</sub> gas flow	1.2 $\div$ 1.5

The measured contact resistances for not etched device ranged from 1.5 to 4.8 k $\Omega$ . In the second approach (plasma etching followed by deposition of contacts) contact resistances were two orders of magnitude higher than in the case without etching (hundreds of k $\Omega$  comparing to few k $\Omega$ ). What is more the measurements show large phase shift ( $\sim 90^\circ$ ), which was frequency dependent. It was not possible to perform 4 point measurements and determine the graphene resistance. This behaviour can be explained by the presence of the polymer contaminants which form an insulating layer between the metal contact and graphene, decreasing the efficiency of current injection (increase of resistance) and raising the capacity component of the resistance (big negative phase shift was detected). In the third approach the etching procedure is followed by annealing in Ar/H<sub>2</sub> after which the contacts were deposited. The contact resistances (dozens of k $\Omega$ ) were smaller comparing with the previous case, but larger than in the case without plasma etching. At last I checked the contact resistances, when the contacts were deposited before etching, then graphene was etched with oxygen plasma etching and annealed in Ar/H<sub>2</sub>. We can see that the obtained contact resistances are comparable with the first case (few k $\Omega$ ). This leads to the conclusion that when structuring the flake is required, the best strategy is to deposit contacts before the plasma etching. If the etching step needs to be performed before the contact deposition, the etching procedure should be always followed by annealing in Ar/H<sub>2</sub> gas flow.

The measurements presented in the following sections were obtained for devices prepared according to the 3rd way: I firstly etched graphene with plasma etching, then annealed it in Ar/H<sub>2</sub> and deposited the contacts afterwards.

## 4.2 Electrical characterisation of the device - Dirac curve.

In the experiments I investigated two devices, the unetched one (later referred as D2), for which I did Hall effect measurements, and the one with an etched channel (later referred as C5), for which I investigated the resistivity versus gate voltage at different magnetic fields. More detailed measurements were impossible to perform because the sample was blown-up while ramping the gate voltage.

Firstly, I determined the contact resistances with 2 point and 3-point measurements. Device geometry and contact resistance for investigated samples is presented in Fig. 4.1

The scaling factor from resistance to square resistivity for unetched device (D2) is  $w/l = 1.5$ , for etched device (C5)  $w/l = 1.3$ .

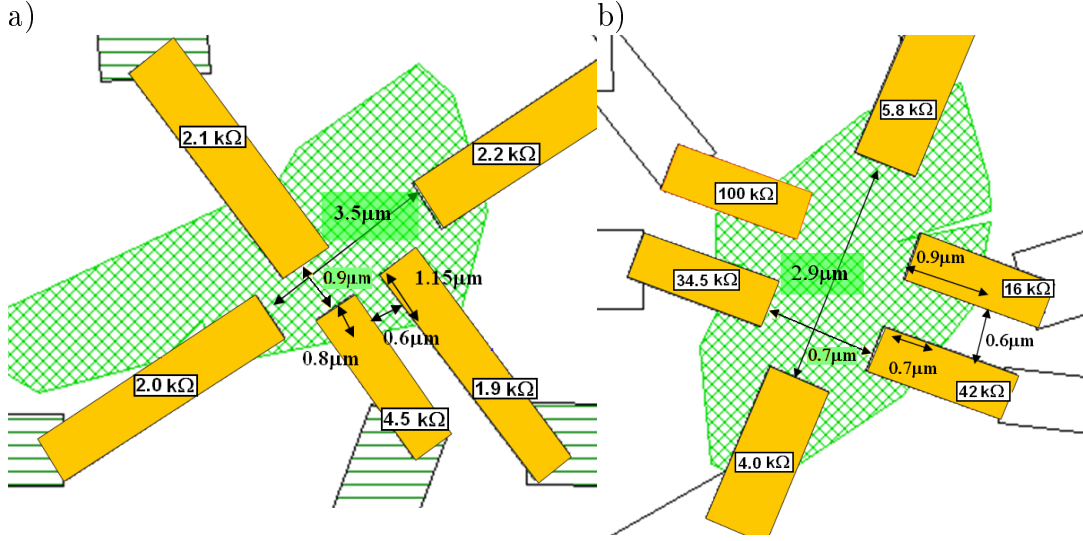


**Figure 4.1:** Device geometry and contact resistances for investigated devices. Image (a) presents the unetched sample, image (b) etched one.

#### 4.2.1 Tracing the charge neutrality point

After the determination of the contact resistances, I measured graphene resistance (4 probe configuration). The graphene resistance depends on the initial doping of the system. The reference point is the voltage of maximum resistivity point,  $V_{Dirac}$ , called Dirac point (more properly, charge neutrality point CNP). To measure the value of initial doping I scanned the graphene resistance as a function of gate voltage  $V_g$ . With the gate we induce charge carriers, which compensate the doping presented in the system. The number of charges induced by the gate voltage into the system is determined according to the Eq. 1.3.

Usually, because of the initial doping, the charge neutrality point is beyond the region of voltage sweep ( $V_{Dirac} > 80V$ ). To bring the Dirac point back towards zero gate voltages, I heated the sample. Heating causes the desorption of water and other molecular adsorbates. In the studied devices, I performed the heating twice before we could observe the Dirac point in scanned voltage range (see Fig. 4.2). In every voltage sweep of graphene resistivity I recorded trace (voltage scan from  $-V_0$  to  $+V_0$ ) and re-trace (voltage scan from  $+V_0$  to  $-V_0$ , where  $V_0$  is the maximum voltage in the sweep). The observed difference between curves for trace and retrace (hysteresis) can be explained by migration of impurities in the  $SiO_2$  and water molecules (possibly trapped between graphene and substrate). After heating the sample for 1 hour at temperature  $150^\circ C$  the slope of resistivity curves went up, suggesting that the heating reduced the initial doping, but the Dirac point was still away from the scanned range. The second heating for 1.5 hour at  $250^\circ C$  induced the shift of the Dirac point toward zero voltage. The Dirac point for D2 device:  $V_{Dirac} = 20V$ , while for C5:  $V_{Dirac} = -6V$ )

The obtained resistivity curves were very broad (the distance between deflection

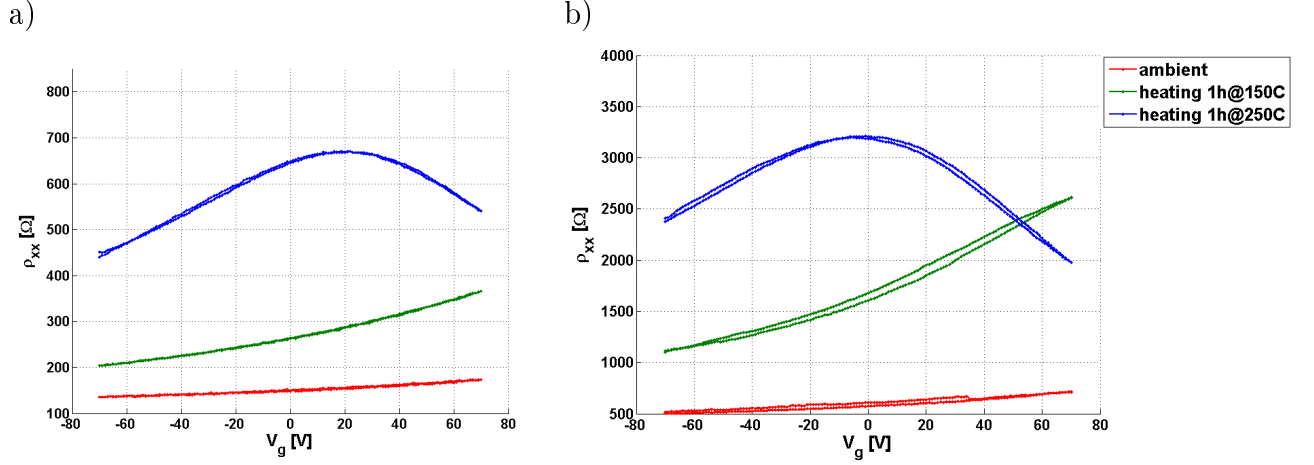


**Figure 4.2:** Graphene resistivity as a function of gate voltage for D2 device (a) and C5 device (b). Red curve was measured in ambient conditions, at initial stage. Green curve shows the resistivity after heating the sample for 1 hour at 150°C. Measurements were performed in vacuum, at  $p \sim 2 \cdot 10^{-6}$  mbar. The blue curve shows the resistivity after second heating for 1.5 hour at 250°C.

points:  $\Delta_{defl.points} \gtrsim 100V$ ). What is more, with the gate sweep (at the same conditions) the Dirac point shift dramatically towards positive voltages ( $\Delta V_{Dirac}$  is up to 70V for 27 sequential voltage sweeps under the same measuring conditions). These suggest the high scattering of the carriers and big influence of the substrate on the electronic transport. The shift of the Dirac point with respect to the number of the voltage sweep, at the same conditions (vacuum,  $p \sim 2 \cdot 10^{-6}$  mbar) is presented in Fig. 4.3

We have to note that for C5 device annealing moved the Dirac point to negative voltages ( $V_{Dirac} = -6V$ ). This suggest that the number of donors prevail over the number of acceptors in graphene. The electron doping in this system can be explained by the presence of Ti contact layer, as it was described in Sec. 1.6.

The resistivity  $\rho_{xx}$  is very flat and broad. Typically we expect the bell-shape curve with a very sharp peak, (reaching values  $\approx 6k\Omega$  and decreasing below  $1k\Omega$  for voltage difference  $V_g - V_{Dirac} > 20V$ ) and small distance between deflection points of few volts ( $\Delta_{defl.points} < 10V$ ). In current experiment the maximum of the curves was much lower:  $\rho_{xx,max} = 0.67k\Omega$  for D2,  $\rho_{xx,max} = 3.2k\Omega$  for C5, and curves were broad ( $\Delta_{defl.points} \gtrsim 100V$ ) indicating poor sample quality.

From the measurements of the Dirac curve, one can calculate mobilities using the equations 1.5 and 1.3 of the Drude model. The obtained values are presented in Fig. 4.4. The arrows indicate values of mobility in the metallic regime, for D2 device  $\mu = 2000cm^2/Vs$  and for C5 device  $\mu = 3400cm^2/Vs$ . Obtained mobilities are low (typically we expect mobilities in the range:  $2\ 000 \div 20\ 000\ cm^2/Vs$ ). This can be explained by contamination left after plasma etching on graphene flake, some

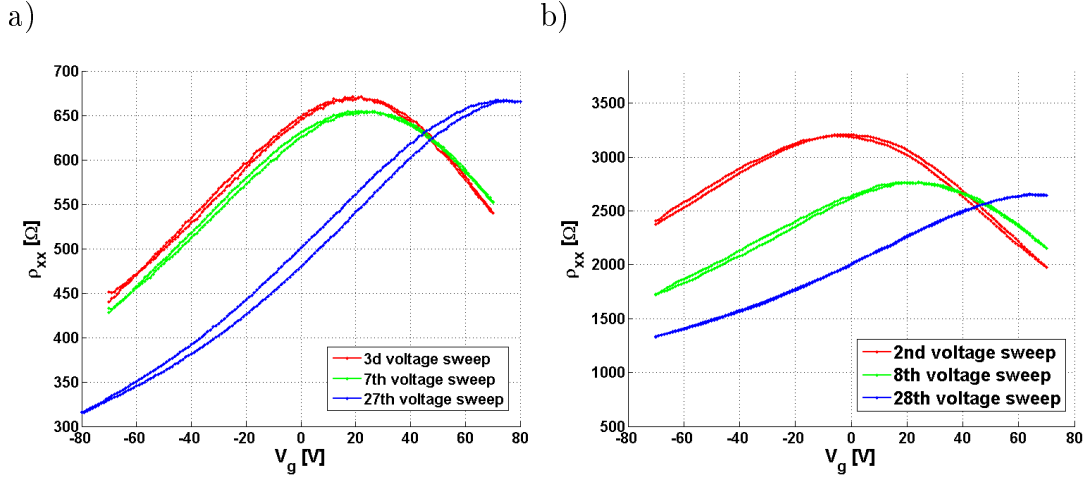


**Figure 4.3:** Shift of the Dirac point in resistivity measurements during the sequential voltage sweep at the same measurement conditions for D2 device (a) and C5 device (b). Red curve describes the first voltage scan after second annealing, green shows the 7th scan and blue 27th scan. In case of C5, these colours corresponds to scans of 2nd, 8th and 28th (the next scan).

of which could not be removed even with the Ar/H<sub>2</sub> annealing.

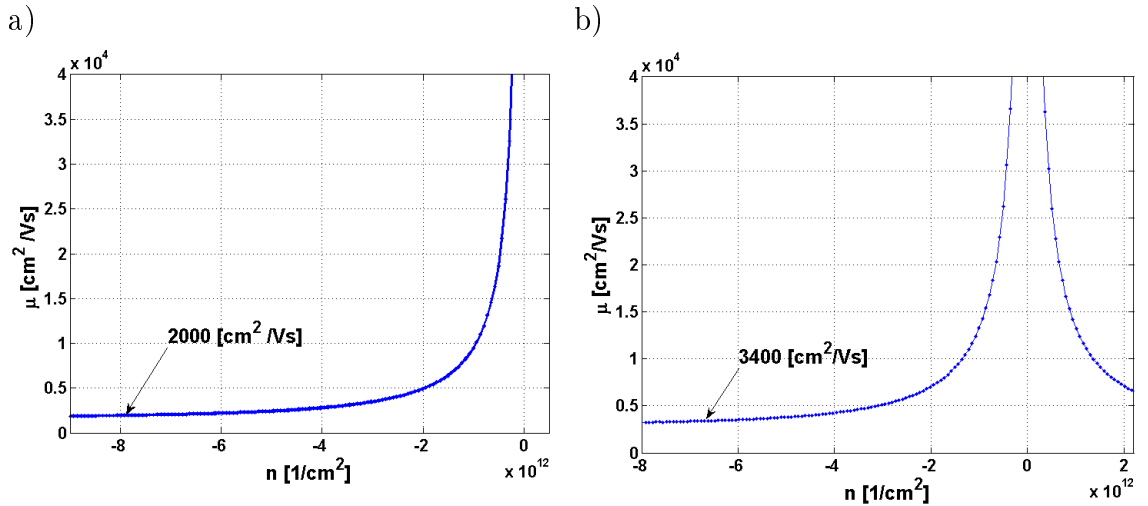


**Figure 4.4:** Mobility of carriers as a function of gate voltage for D2 (a) and C5 (b) device. The arrows indicate value of mobility in the metallic regime.

The minimum conductivity is calculated to be for device D2:  $\sigma_{min} = 38.7e^2/h$  and for device C5:  $\sigma_{min} = 8.26e^2/h$ . This value are higher than expected (we expect  $\sigma \approx 4e^2/h$ , as in Fig. 1.5), which is another evidence of poor sample quality.

## 4.2.2 Influence of magnetic field on the graphene resistivities

In this section I study the Hall effect and a change of the Dirac curve shape at different magnetic fields. Unfortunately additional investigations were impossible due to the damage of the sample. I managed to measure the Hall effect on an unetched device D2 and the Dirac curves at various magnetic fields for etched device C5.

## 4.2.3 Hall effect measurements

The Hall effect measurement is a very important technique to determine the concentration of the charge carriers in the studied system. To get its value, I focused on measuring the Hall coefficient  $R_H$  (see Eq. 1.6), from the relation with the transversal resistance  $R_{xy} = BR_H$ . We can determine the Hall coefficient in two ways:

1. from the slope of  $R_{xy}$  versus magnetic field at the constant gate voltage
2. from  $R_{xy}$  versus gate voltage at constant magnetic field

In the first approach we measure  $R_{xy}$  versus magnetic field, for arbitrary number of values of magnetic field, at fixed gate voltage. Then we can perform the linear fit  $R_{xy} = \gamma \cdot B$ , and from the slope  $\gamma$  of the linear fit we obtain  $R_H$ , as  $R_H = \gamma$ . The example of measurements for 2 different gate voltages,  $V_g = 30V$  and  $V_g = -30V$ , together with linear fits presents Fig. 4.5. For  $V_g = -30V$  (holes conduction regime)  $R_H = -58.5\Omega/T$  while for  $V_g = 30V$  (electrons conduction regime)  $R_H = 112.1\Omega/T$ . The asymmetry in the absolute value of the slopes of the curves originates from the shift of the Dirac point to positive voltages ( $V_{Dirac} \approx 20V$ ).

This approach gives more reliable measurements especially in case when the signal is very noisy. With the increase of the number of magnetic field points (x-axis), we increase the number of data (y-axis) for linear regression and reduce the measurement error. During the scan we don't sweep the gate voltage (it is fixed at one particular value), and therefore we reduce the effect of the Dirac point shift due to voltage scans. In our case the shift under sweeping the gate voltage was substantial (Fig. 4.3). The disadvantage of this method is that it is time consuming because to record  $R_H$  for different carrier concentrations, one has to repeat the measurements for many different gate voltage values.

In the second approach one measures  $R_{xy}$  versus gate voltage at constant magnetic field. In this way we can extract the value of  $R_H$  for different charge carrier concentrations at once (Fig. 4.6).

This approach can be less time consuming, but obtained values of  $R_H$  have larger observational error (as we determine the  $R_H$  basing on single measurement),

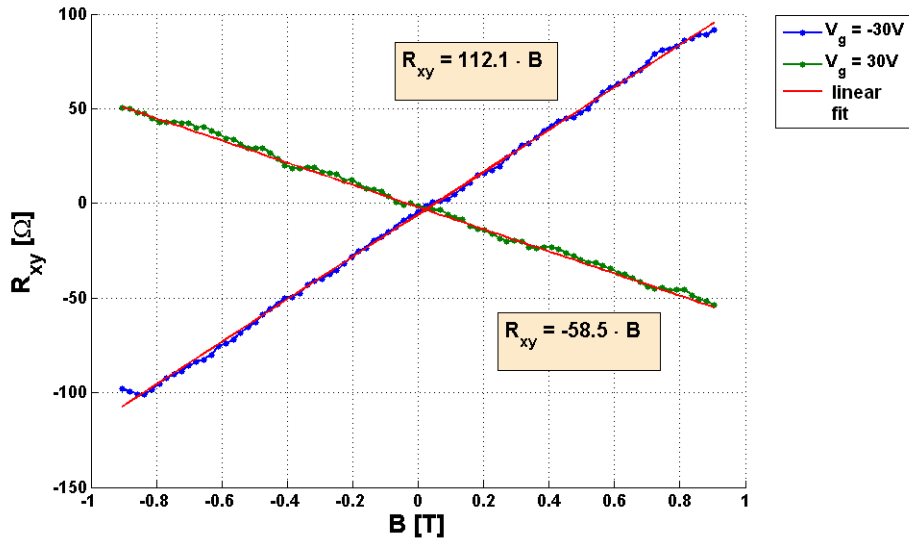


**Figure 4.5:** The transversal resistance  $R_{xy}$  versus magnetic field at constant gate voltage. Measurements were done for two gate voltages  $V_g = 30V$  and  $V_g = -30V$ . From the linear fit we obtain Hall coefficient:  $R_H = 112.1\Omega/T$  for  $V_g = 30V$  and  $R_H = -58.5\Omega/T$  for  $V_g = -30V$ .

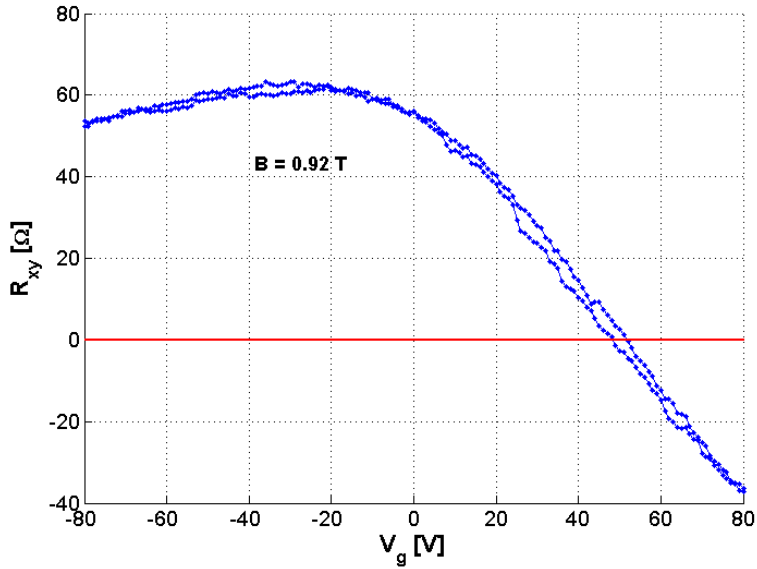


**Figure 4.6:** The transversal resistance  $R_{xy}$  versus gate voltage at constant magnetic field ( $B=0.92T$ ). From this measurement one can immediately calculate the Hall coefficient  $R_H$  as a function of the charge concentration (as from definition  $R_{xy} = R_H \cdot B$ ). However, the coefficient in this case mimics the measurement noise of  $R_{xy}$ .

especially in case when the signal  $R_{xy}$  is very noisy. To reduce this error, we can repeat the scans for few different values of magnetic field and average the value of  $R_H$ . However, one also has to keep in mind that sweeping the gate during the measurements may shift the Dirac point. Therefore, before doing the averaging, it is crucial to shift the curves to one common Dirac point.

For the purpose of verification of the model, I chose to measure  $R_{xy}$  versus gate voltage at constant magnetic field (the second approach). Basing on device geometry, I assumed that  $R_{xy} = \rho_{xy}$ . I sequentially performed voltage sweeps for 8 different values of magnetic field:  $\pm\{0.92, 0.84, 0.452, 0.226\} T$ . Firstly I measured the signal for zero magnetic field, and subtracted it from further measured curves to exclude background effects. Within the voltage scan range I expected to measure two extreme values of  $\rho_{xy}$ : maximum and minimum, as it was measured in [27] (Fig. 1.14). However, similarly to the case of longitudinal resistivity, the  $\rho_{xy}$  also showed large broadening (distance between minimum and maximum is approximately 140V). In all cases the voltage scan range was too small to obtain both minimum and maximum in one curve. Similarly to the measurements of  $\rho_{xx}$  versus gate voltage, also  $\rho_{xy}$  showed the shift of the Dirac point while sweeping the gate voltage (at the Dirac point  $\rho_{xy} = 0$ ). Let us assume that for observed shift of the Dirac point the system properties like mobility and impurity concentration, did not change considerably. Hence, we can shift the recorded curves to each other, so that they all cross zero at one point. Arbitrarily, I fixed Dirac point at the value obtained for the first scan ( $V_{Dirac} = 51V$ ). An example of recorded curves after corrections of the Dirac point position are presented in Fig. 4.7. As expected, we observe axial symmetry (along x-axis) of recorded curves for the same values but different sign of magnetic fields.

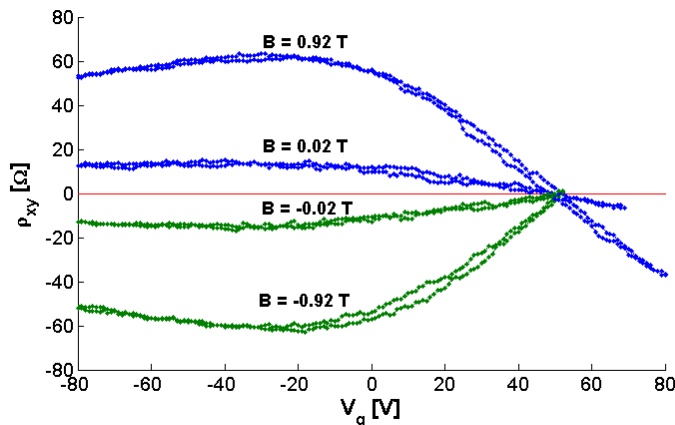


**Figure 4.7:** Transversal resistivity  $\rho_{xy}$  as a function of gate voltage at different magnetic fields (the values of the corresponding field are placed above each of the recorded curves). All curves have subtracted background and they are shifted to arbitrarily chosen Dirac point (at  $V_{Dirac} = 51 V$ ).

During the measurements the Dirac point shifted from 36V to 74V. From measurements of  $\rho_{xy}$  one can calculate the Hall coefficient (according to the formula:  $R_{xy} = R_H \cdot B$ ) by averaging the measurements from scans at different magnetic fields. The obtained curve is presented in Fig. 4.8(a). From the Hall coefficient we can determine the charge carrier concentration  $n$  independently from Eq. 1.3. The comparison between charge carrier concentration obtained from  $R_H$ , via Eq. 1.6

and from Eq. 1.3 is presented in Fig.4.8(b). We observe that away from the Dirac point both curves approach each other but they don't merge within the voltage scan range (at  $(V_g - V_{Dirac}) = -90V$ :  $\Delta n = 1.7 \times 10^{12} cm^{-2}$ ).

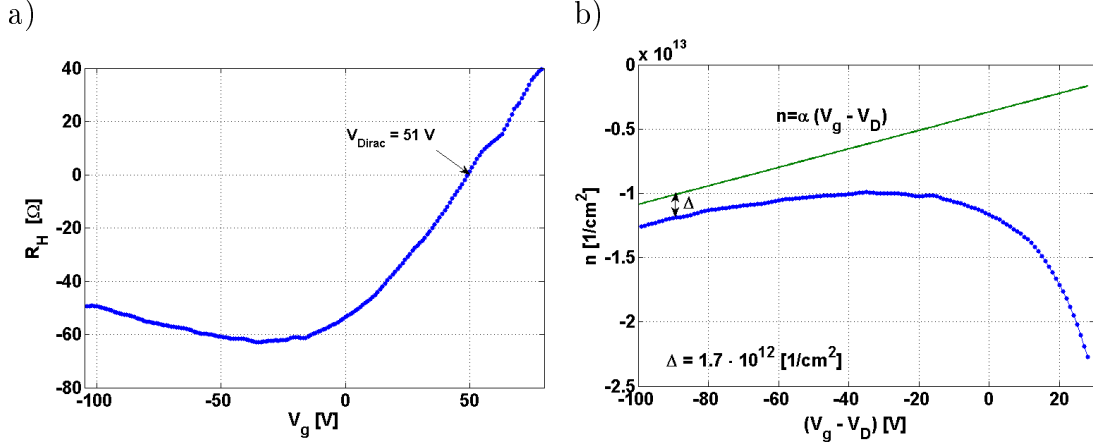


**Figure 4.8:** The Hall coefficient  $R_H$  (a) and the charge carrier density  $n$  (b) as a function of gate voltage.  $R_H$  is obtained from  $\rho_{xy}$  as a function of gate voltage at different magnetic fields. For each scan I adjusted the Dirac point to  $V_{Dirac} = 51V$ . To reduce the fluctuations from single measurement I calculated  $R_H$  as an arithmetical average over all scans. From  $R_H$  I calculated charge carrier density (b), according to Eq. 1.6. Green line represents the charge carrier density induced by the gate voltage, from the Eq. 1.3. Away from the Dirac point both curves show similar slope but don't merge within the voltage scan range.

#### 4.2.4 Dirac curve under different magnetic fields

The longitudinal resistance  $\rho_{xx}$  was measured in etched device. I sequentially performed voltage sweeps for 8 different values of magnetic field:  $\pm\{0.92, 0.84, 0.452, 0.226\}$  T. Similarly to the measurements of non-etched device, the Dirac curve shifted during sweeping the gate voltage. Again let us assume that for this shift of the Dirac point the system properties, like mobility and impurity concentration, did not change considerably. Hence, I can shift the recorded curves to each other, so that they all show maximum at one voltage. Arbitrarily, I fixed the Dirac point at the value obtained for the first scan ( $V_{Dirac} = 47V$ ). An example of recorded curves after correction of the Dirac point position is presented in Fig. 4.9. With the decrease of magnetic field, the position of resistivity maximum  $\rho_{xx,max}$  decreases (marked by arrow), indicating positive magnetoresistance. As expected, I observed overlap of the recorded curves for the same value but different sign of magnetic field (curves for  $+0.23T$  and  $-0.23T$  in Fig. 4.9).

Next, I compared the experimental measurements with proposed model (described in details in Chapter 2), trying to find the quantitative correspondence.

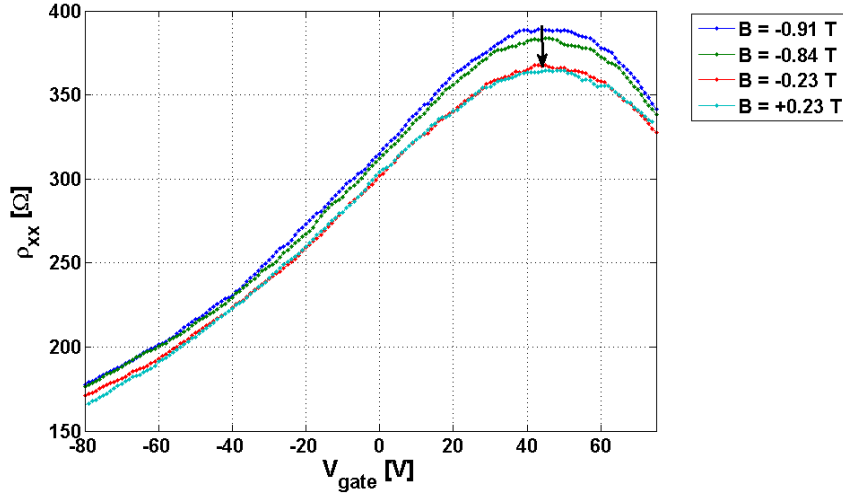


**Figure 4.9:** Dirac curve as a function of gate voltage at different values of magnetic field in C5 device. A black arrow marks the decrease of resistivity maximum  $\rho_{xx,max}$  with the decrease of the magnetic field (positive magnetoresistance). As expected, the red and light blue curves overlap as they are recorded for the same absolute value of magnetic field,  $|B| = 0.23T$ .

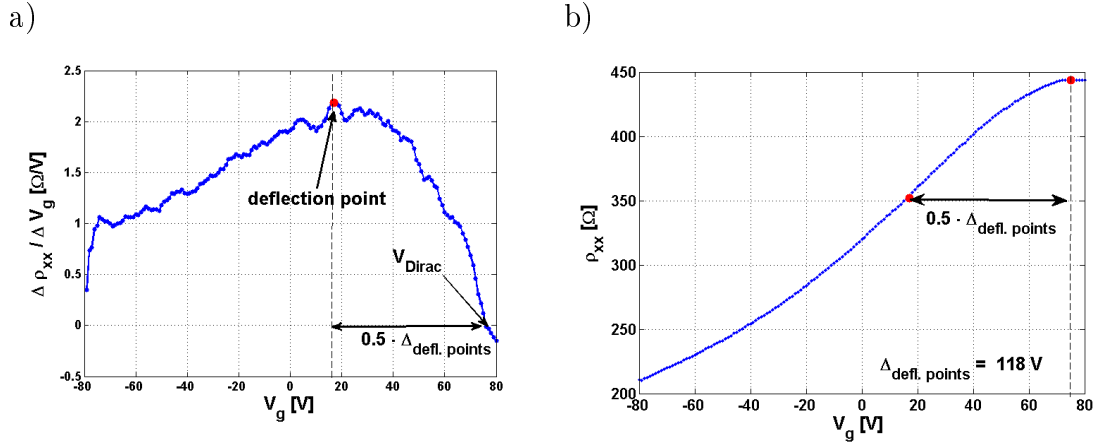
### 4.3 Relation between obtained experimental results and proposed theoretical model.

Proposed in Chapter 2 model includes three free parameters: mobility  $\mu$ , gaussian broadening of puddles  $\sigma$  and the offset in longitudinal resistivity  $\rho_{offset}$ . To keep the quantitative relation between the model and experimental results, these values are determined from experimental Dirac curves and are kept constant for all simulated curves at  $B \neq 0$  of particular device. As it was shown in the Chapter 2, the broadening of the calculated curves doesn't depend on the mobility (Fig. 2.16) and can be directly determined from the distance between deflection points of the Dirac curve  $\rho_{xx}$ , through the calibration curve in Fig. 2.14. In presented model the value of mobility is constant in whole range of the carrier densities. Therefore, I can determine its value from measurements in the metallic regime from Eq. 1.5, where Drude model also holds:  $\mu = 2000cm^2/Vs$  for D2 (Fig. 4.4(a)), and  $\mu = 3400cm^2/Vs$  for C5 (Fig. 4.4(b)). In some cases addition of offset value  $\rho_{offset}$  was necessary. When it was the case, the added value was kept the same for scans of the same resistivity type at different magnetic fields. As it was described in Chapter 1, the offset value represents the short-range, neutral scatterers. However the relation between the offset value and the number of neutral scattering centres is still unclear. The Dirac point of theoretical curves is shifted to coincide with the experimental one.

### 4.3.1 Comparison of the measurements with the model for the non-etched device D2

I begin our comparison from the device D2, for which I measured Dirac curves at zero magnetic field and Hall curves at different constant magnetic fields. I start the calculations from determining the distance between deflection points  $\Delta_{defl.points}$ , see Fig. 4.10(a). I calculated them numerically as a minimum and maximum of the first derivative  $d\rho_{xx}/dV_g$ . In our measurement only one extreme value fit into the scan voltage range. Therefore I determined the distance between maximum deflection point and the Dirac point, which corresponds to  $0.5 \cdot \Delta_{defl.points}$ . For D2 device  $\Delta_{defl.points} = 118V$ , which corresponds to  $\sigma = 263meV$ . Later on I fixed  $\sigma$  and  $\mu$  ( $\sigma = 263meV$ ,  $\mu = 2000cm^2/Vs$ ) and calculated for them the  $\rho_{xx}$  from the model (according to Eq. 2.12). Both experimental curve (green dotted line) and the one calculated from the model (blue constant line) overlap onto each other confirming high accuracy of predictions (Fig.4.10(c)).

Further on, I calculated transversal resistivity  $\rho_{xy}$  at different magnetic fields. The calculations were performed for the values determined from the Dirac curves ( $\sigma = 263meV$ ,  $\mu = 2000cm^2/Vs$ ) using the formula Eq. 2.13. The comparison with experimental data is presented in Fig. 4.11(c). For clearness, the plots for different magnetic field are presented separately. All the theoretical curves fit well to the experimental measurements confirming good quantitative agreement with the model.



c)  $\sigma = 263\text{meV}$ ,  $\mu = 2000\text{cm}^2/\text{Vs}$ ,  $\rho_{offset} = 52\Omega$

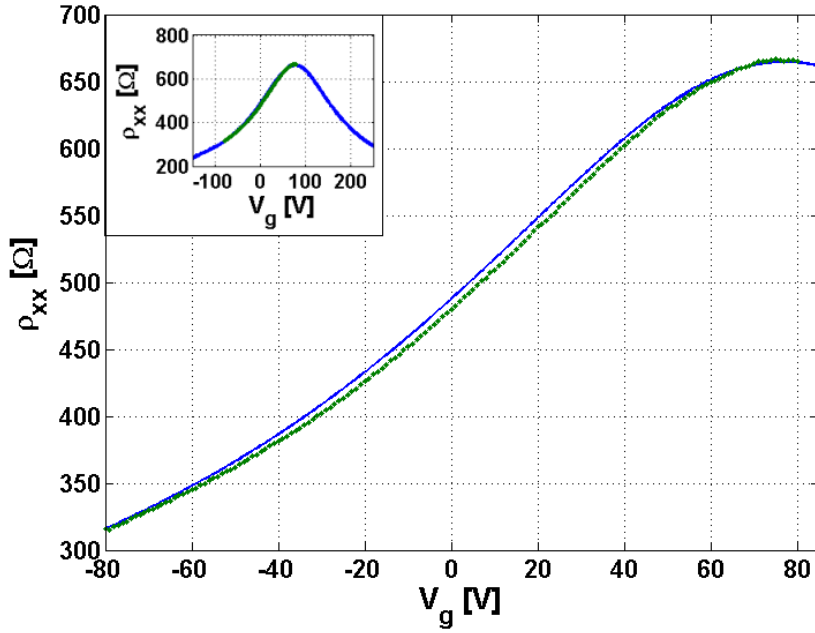
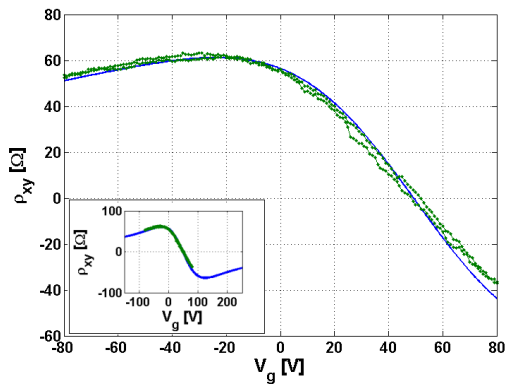
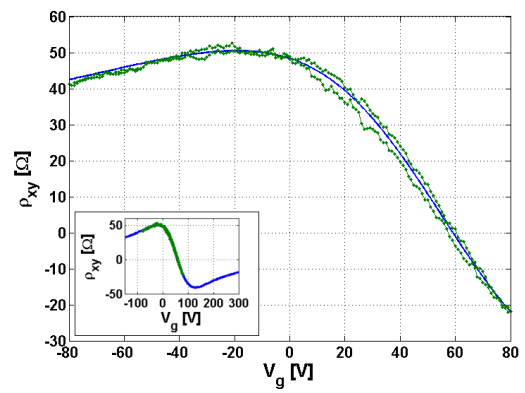


**Figure 4.10:** Determination of deflection point distance  $\Delta_{defl.points}$  and comparison of the Dirac curve (device D2) with the theoretical curve. (a) Numerical differential of longitudinal resistivity  $\Delta\rho_{xx}/\Delta V_g$  with marked maximum and the Dirac point. Indicated with an black arrow distance corresponds to the half of the deflection points distance. (b) Longitudinal resistivity with marked deflection point (determined from (a)). The  $\Delta_{defl.points}$  is directly related to the Gaussian broadening of carrier density  $\sigma$ , which is an input value to the model. For  $\Delta_{defl.points} = 118\text{V}$  the broadening  $\sigma = 263\text{meV}$ . (c) Comparison between measured data (green dots) and theoretical predictions (blue line). The calculation parameters are placed above the Figure (c). Inset represents the same curves in larger voltage range.

a)  $B = 0.91$  T



b)  $B = 0.67$  T



c)  $B = 0.45$  T

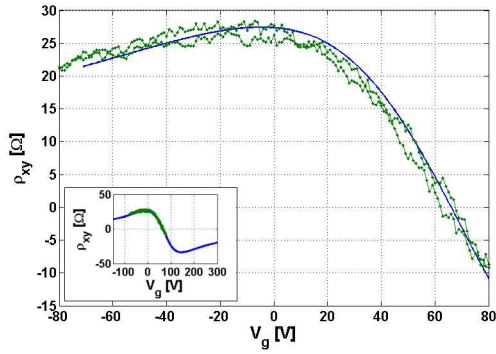


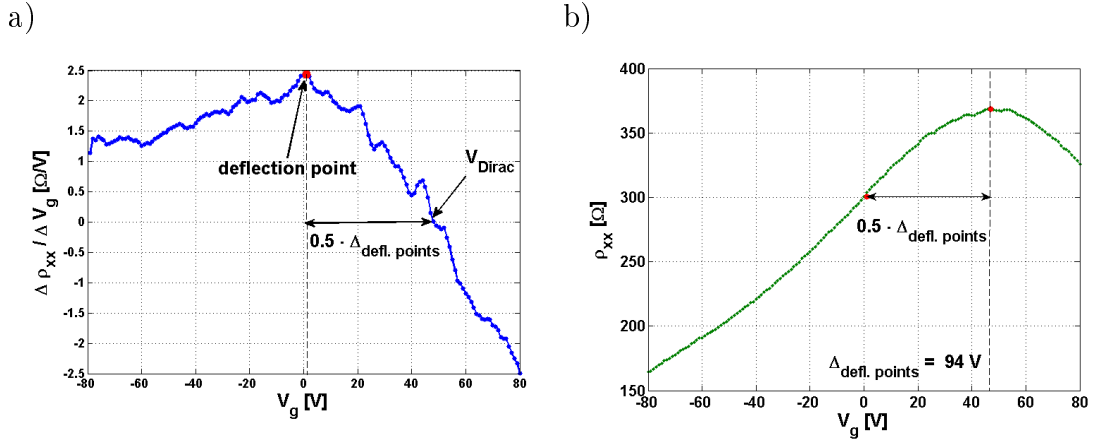
**Figure 4.11:** Hall effect measurements on D2 device. Comparison between measured data (green dots) and theoretical predictions (blue line) for three different magnetic fields. Insets represent the same curves in larger voltage range.

### 4.3.2 Comparison of the measurements with the model for the etched device C5

Now I compare the measurements from etched device C5, for which I attained Dirac curves at different magnetic fields. As before I started the calculations from determining the distance between deflection points  $\Delta_{defl.points}$ , see Fig. 4.12(a). For C5 device  $\Delta_{defl.points} = 94V$ , which corresponds to  $\sigma = 233meV$ . I fixed  $\sigma$  and  $\mu$  and  $\rho_{offset}$  ( $\sigma = 233meV$ ,  $\mu = 3400cm^2/Vs$ ,  $\rho_{offset} = 56\Omega$ ) and calculated for them the  $\rho_{xx}$  from the model (according to Eq. 2.12). Both experimental curves (green dotted line) and calculated from the model (blue constant line) overlap onto each other confirming high accuracy of predictions (Fig.4.12(c)).

Further on, I calculated the resistivity  $\rho_{xx}$  at different magnetic fields. The calculations were performed for the values determined from the Dirac curves ( $\sigma = 233meV$ ,  $\mu = 3400cm^2/Vs$ ,  $\rho_{offset} = 56\Omega$ ), using the formula Eq. 2.12. The comparison with experimental data is presented in Fig. 4.13(c). For clearness, the plots for different magnetic field are presented separately.

The obtained value of broadening ( $\sigma = 263meV$  for D2 device and  $\sigma = 233meV$  for C5 device) are very big. The best reported value for graphene on  $SiO_2$  is 40 meV [40] and is even smaller for suspended graphene (10meV, after [41]). Also the values of minimum conductivity ( $\sigma_{min} = 38.7e^2/h$  for D2,  $\sigma_{min} = 8.3e^2/h$  for C5) are high comparing with the expect values from the range:  $2 \div 12e^2/h$ . High minimum conductivity can be related to the residual density induced by the inhomogeneous charge distribution in the sample at CNP. Therefore the higher minimum conductivity of device D2 comparing with device C5 also implies larger broadening of its resistivity (the fitted broadening  $\sigma$  was larger). All these confirms that the prepared devices had poor quality. Although the comparison between the experimental measurements and the proposed model is very good, one has to remember, that the equations for  $\rho_{xx}$  and  $\rho_{xy}$  are nonlinear and the agreement with experimental data may depend on the particular range of values of input parameters. Therefore it is essential to test this model for a high quality sample as a verification.



c)  $\sigma = 233\text{meV}$ ,  $\mu = 3400\text{cm}^2/\text{Vs}$   $\rho_{offset} = 56\Omega$

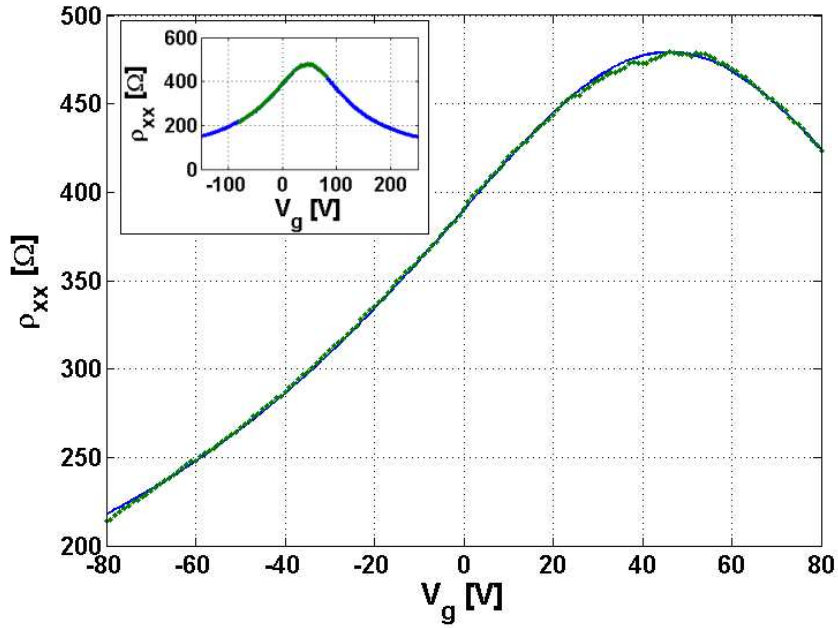
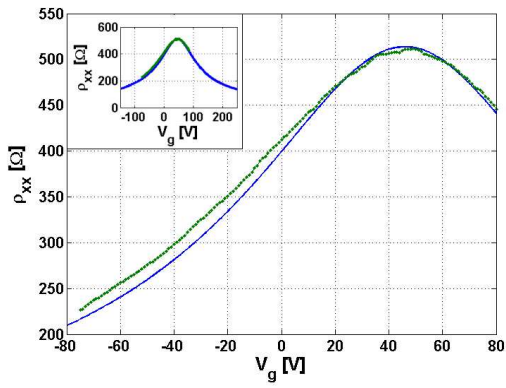
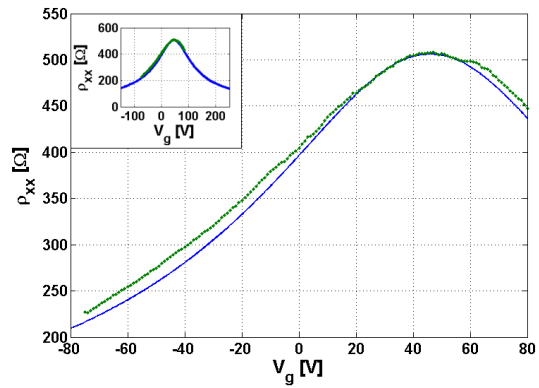


**Figure 4.12:** Determination of deflection point distance  $\Delta_{defl.points}$  and comparison of Dirac curve (device C5) with the theoretical curve. (a) Numerical differential of longitudinal resistivity  $\Delta\rho_{xx}/\Delta V_g$  with marked maximum and the Dirac point. Indicated with an black arrow distance corresponds to the half of the deflection points distance. (b) Longitudinal resistivity with marked deflection point (determined from (a)). The  $\Delta_{defl.points}$  is directly related to the Gaussian broadening of carrier density  $\sigma$ , which is an input value to the model. For  $\Delta_{defl.points} = 94\text{V}$  the broadening  $\sigma = 233\text{meV}$ . (c) Comparison between measured data (green dots) and theoretical predictions (blue line). The calculation parameters are placed above the Figure (c).

a)  $B = 0.91$  T



b)  $B = 0.84$  T



c)  $B = 0.45$  T

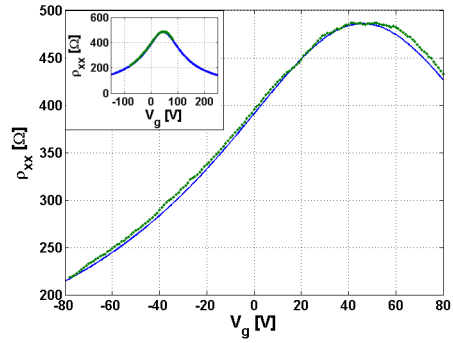


**Figure 4.13:** The Dirac curves obtained from measurements on C5 device at different magnetic fields. Comparison between measured data (green dots) and theoretical predictions (blue line) for three different magnetic fields. Insets represent the same curves for larger voltage range.

# Chapter 5

---

## Conclusions

The goal of this thesis was the analysis of electronic transport in graphene both experimentally and theoretically. An important part of presented work focuses on development of simple, semiclassical model which could explain, in quantitative way, the graphene electronic transport, especially at the charge neutrality point. The carrier concentration in thermal equilibrium at room temperature and with additionally fluctuating electric potential (defined by the Gaussian distribution with standard deviation  $\sigma$ ) was calculated. The effect of fluctuating potential originates from the formation of hole-electron puddles induced by the substrate and adsorbed charge transferring molecules (dopants). Both effects (thermal equilibrium and variation of potential) lead to coexistence of holes and electrons in the vicinity of charge neutrality point. Therefore the modelled resistances versus gate voltage and magnetic field both in thermal equilibrium and in graphene with potential variations qualitatively showed the same behaviour: decrease of maximum resistivity values and broadening of the curves. It was shown here that the extension of the model into system of two charge type carriers, even though it assumes constant mobility of carriers in the whole carrier concentration range, explains finite maximum of longitudinal resistance  $\rho_{xx}$  and zero transversal resistance  $\rho_{xy}$  at charge neutrality point and magnetoresistance of graphene. The derived expressions of resistances are non-linear functions of the charge carrier concentrations. The analysis of the influence of parameters:  $\sigma$ ,  $\mu$  on the resistances maxima and its broadening (described by the voltage distance between deflection points) showed regions of weak and strong dependence on the value of input parameters.

To verify the proposed model I prepared graphene devices in Hall bar geometry. To reduce the ambiguity of the current path I perform shaping of graphene with oxygen plasma etching. With the use of AFM I investigated the surface roughness of graphene and SiO<sub>2</sub> at different fabrication steps. It was shown here that after oxygen plasma etching the protective PMMA layer cannot be fully removed by an ordinary treatment with warm acetone. This concerns not only the regions of graphene and SiO<sub>2</sub> in the etched area but also the regions far apart from the etching window (>1mm). Performance of an additional cleaning step: the annealing in Ar/H<sub>2</sub> gas flow, reduced the surface roughness, especially at unetched regions. Around the etched away graphene parts, the contamination from the possibly burned carbon appeared, which could not be removed by annealing in Ar/H<sub>2</sub> gas flow. Plasma etched graphene devices were prepared in different sequences of fabrication steps to test their influence on contact resistance. The optimal steps-sequence for device preparation, when one needs to perform plasma etching was achieved. It is to firstly deposit contacts and then perform plasma etching. The further cleaning procedure at the Ar/H<sub>2</sub> gas flow is recommended, to remove the remaining contamination

after plasma etching from the graphene surface. When the etching step needs to be performed before contact deposition, the etching procedure should be always followed by annealing in Ar/H<sub>2</sub> gas flow.

The presented in the thesis measurements were performed on the etched device, where I studied the  $\rho_{xx}$  as a function of gate voltage in different magnetic fields, and on the unetched device, where I studied Hall effect. Both devices were prepared on the same wafer and hence underwent similar fabrication procedure. Particularly, for both studied devices, the measured resistivities as a function of gate voltage were very broad (voltage distance between deflection points of longitudinal resistivity  $\Delta_{defl.points} \gtrsim 100V$ ). For both devices, the standard deviation of Gaussian distribution of potential variations in the model was very high:  $\sigma = 235meV$  for etched device,  $\sigma = 255meV$  for unetched device. This can be explained by poor quality of prepared devices. However, the comparison of the measurements with the modelled resistivities are in a good agreement. The parameters of the model:  $\sigma$ ,  $\mu$ , were obtained from the resistivity curves, independently from the fitting procedure. The good agreement with the model confirms the quantitative accuracy of the proposed description. However, the agreement with experimental data may depend on the particular range of values of input parameters. Therefore it is essential to test this model for high quality sample as a verification.

# Acknowledgement

First and foremost I would like to thank my supervisor PhD Alina Veligura. She introduced me to the exciting physics in graphene, the experimental and measurement techniques and always was an invaluable source of practical advice. I would like to stress my gratefulness not only for her help, patience, constant readiness to support and contagious enthusiasm with which she is doing her research, but also for many critical comments, always pointing sharp the root of the problem. Working with Alina had a great influence not only on the presented results but also on my personality. Lots of discussions with her made me aware of some of my strong and weak points - the precious knowledge without which the changes for better cannot start.

I would like to warmly thank Prof. Bart van Wees, the leader of the Physics of Nanodevices Group (FND) and the mentor of the thesis. His constant and motivating interest in the research progress built up a very nice and inspiring scientific environment. I am grateful to him for giving me the access to the very well-facilitated laboratory and for the chance to work with the top-level equipment for nanodevices.

The third person I am cordially thankful is Dr. Csaba Jozsa, for assistance during measurements and the experience he was always willing to share. My thanks I also direct to Msc. Paul Zomer, my office mate, and to PhD Thomas Massen for many useful discussions.

I would like to thank our group technicians: Siemon, Bernard and Johan, who always keep an eye on the equipment and helped in resolving many technical puzzles. I am really grateful for your whole visible and invisible work (like changing N<sub>2</sub> cans, bonding devices, maintaining the equipment at its best performance level etc.) and for the very positive state of mind every day.

There are many other people from FND who at some point gave me support, inspire with suggestions, share experience and create a nice working surrounding. Guys, thank you very much for that.

Last but not least I want to thank my family and friends, for support, believing in me and keeping in touch in times when I was difficult to bear. This altogether made the year of my master project not only a key stone in my scientific development but also in development as a person. I promise that initiated changes won't be wasted.



# Bibliography

- [1] K.S. Novoselov, A.K. Geim, S.V. Morozov, D. Jiang, Y. Zhang, S.V. Dubonos, I.V. Grigorieva, A.A. Firsov *Electric Field Effect in Atomically Thin Carbon Films*, Science, Vol. 306. no. 5696, 666 - 669 (2004)
- [2] A. Castro Neto, F. Guinea, N.M.R. Peres, K.S. Novoselov & A.K. Geim *The electronic properties of graphene*, Rev. Mod. Phys. 81, 109 (2009)
- [3] M.I. Katsnelson, K.S. Novoselov & A.K. Geim, *Chiral tunneling and the Klein paradox in graphene*, Nature Physics 2, 620 (2006)
- [4] F. Chen, J. Xia, D.K. Ferry & N. Tao *Dielectric screening enhanced performance in graphene FET*, Nano Lett. 9 (7) pp. 2571-2574 (2009)
- [5] K.I. Bolotin, K.J. Sikes, Z. Jiang, M. Klima, G. Fudenberg, J. Hone, P. Kim & H.L. Stormer *Ultrahigh electron mobility in suspended graphene*, Solid State Communications 146, 351-355 (2008)
- [6] D.L. Rode *Electron transport in InSb, InAs, and InP*, Phys. Rev. B3 (10) pp. 3287 - 3299 (1971)
- [7] T. Dürkop, S.A. Getty, E. Cobas & M.S. Fuhrer *Extraordinary Mobility in Semiconducting Carbon Nanotubes*, Nano Lett. 4, 35-39 (2004)
- [8] J-H. Chen, C. Jang, S. Xiao, M. Ishigami & M.S. Fuhrer *Intrinsic and extrinsic performance limits of graphene devices on SiO<sub>2</sub>*, Nature Nanotechnology 3, 206 - 209 (2008)
- [9] M. I. Katsnelson *Zitterbewegung, chirality, and minimal conductivity in graphene*, Eur. Phys. J. B 51, 157-160 (2006)
- [10] A.K. Geim, K.S. Novoselov *The rise of graphene*, Nature Materials 6, 183-191 (2007).
- [11] L.D. Landau, E.M. Lifshitz *Statistical Physics*, Part I Pergamon, Oxford, (1980)
- [12] N.D. Mermin *Crystalline Order in Two Dimensions*, Phys. Rev. 176, 250 - 254 (1968)
- [13] D.R. Nelson, T. Piran & S. Weinberg *Statistical Mechanics of Membranes and Surfaces*, World Scientific, Singapore, (2004).

- [14] E. Stolyarova, K.T. Rim, S. Ryu, J. Maultzsch, P. Kim, L.E. Brus, T.F. Heinz, M.S. Hybertsen & G.W. Flynn *High-resolution scanning tunneling microscopy imaging of mesoscopic graphene sheets on an insulating surface*, Proc. Natl. Acad. Sci. USA, Vol. 104, No. 22, 9209-9212 (2007)
- [15] M.Ishigami, J.H. Chen, W.G. Cullen, M.S. Fuhrer & E.D. Williams *Atomic Structure of Graphene on SiO<sub>2</sub>*, Nano Lett. 7 (6), pp 1643-1648, (2007)
- [16] J.C. Meyer, A.K. Geim, M.I. Katsnelson, K.S. Novoselov, T.J. Booth & S. Roth *The structure of suspended graphene sheets*, Nature 446, 60-63 (2007)
- [17] P.Blake, E.W. Hill, A.H. Castro Neto, K.S. Novoselov, D. Jiang, R. Yang, T.J. Booth & A.K. Geim *Making graphene visible*, Appl. Phys. Lett. 91, 063124 (2007)
- [18] J. Martin, N. Akerman, G. Ulbricht, T. Lohmann, J.H. Smet, K. von Klitzing, A. Yacoby *Observation of electron-hole puddles in graphene using a scanning single-electron transistor*, Nature vol. 4, 2008
- [19] M.I. Katsnelson & A.K. Geim *Electron scattering on microscopic corrugations in graphene*, Phil. Trans. R. Soc. A vol. 366 no. 1863 195-204 (2008)
- [20] K. Nomura & A.H. MacDonald *Quantum Transport of Massless Dirac Fermions*, Phys. Rev. Lett. 98, 076602 (2007)
- [21] E.H. Hwang, S. Adam & S. Das Sarma *Carrier Transport in Two-Dimensional Graphene Layers*, PRL 98, 186806 (2007)
- [22] S. Adam, E.H. Hwang, E. Rossi & S. Das Sarma *Theory of charged impurity scattering in two dimensional graphene*, Solid State Communications 149, 1072 (2009)
- [23] J.H. Chen, C. Jang, M.S. Fuhrer, E.D. Williams, M. Ishigami *Charge impurity scattering in graphene*, Nature Physics 4, 377 - 381 (2008)
- [24] O. Leenaerts, B. Partoens & F.M. Peeters *Adsorption of H<sub>2</sub>O, NH<sub>3</sub>, CO, NO<sub>2</sub> and NO on graphene: A first-principles study*, Phys. Rev. B 77, 125416 (2008)
- [25] O. Leenaerts, B. Partoens & F.M. Peeters *Water on graphene: Hydrophobicity and dipole moment using density functional theory*, Phys. Rev. B 79, 235440 (2009)
- [26] K. Pi, K.M. McCreary, W. Bao, Wei Han, Y.F. Chiang, Yan Li, S.-W. Tsai, C.N. Lau, R.K. Kawakami *Electronic Doping and Scattering by Transition Metals on Graphene*, arXiv:cond-mat.mes-hall/0903.2837v1 (2009)
- [27] T.O. Wehling, K.S. Novoselov, S.V. Morozov, E.E. Vdovin, M.I. Katsnelson, A.K. Geim & A.I. Lichtenstein *Molecular Doping of Graphene*, Nano Lett., 8 (1), pp 173-177, (2008)

- [28] A. Veligura *Graphene-based sensors: the road to single molecule detection*, Master Thesis at Physics of Nanodevices Group, Rijksuniversitat Groningen, (2008)
- [29] S. Cho & M.S. Fuhrer *Charge transport and inhomogeneity near the minimum conductivity point in graphene*, Phys. Rev. B 77, 081402(R) (2008)
- [30] K.S. Novoselov, A.K. Geim, S.V. Morozov, D. Jiang, M.I. Katsnelson, I.V. Grigorieva, S.V. Dubonos & A.A. Firsov *Two-dimensional gas of massless Dirac fermions in graphene*, Nature 438, 197-200 (2005)
- [31] F.V. Tikhonenko, A.A. Kozikov, A.K. Savchenko & R.V. Gorbachev *Transition between electron localisation and antilocalisation in graphene*, arXiv:cond-mat.mes-hall/0903.4489v1 (2009)
- [32] T. Fang, A. Konar, H. Xing & D. Jena *Carrier statistics and quantum capacitance of graphene sheets and ribbons*, App. Phys. Lett. 91, 092109 (2007)
- [33] E.H. Hwang, S. Adam, S.Das Sarma *Transport in chemically doped graphene in the presence of adsorbed molecules*, arXiv:cond-mat/0610834v2 (2006)
- [34] S. Adam, E.H. Hwang, V.M. Galitski & S. Das Sarma *A self-consistent theory for graphene transport*, Proc. Natl. Acad. Sci. USA 104, 18392 (2007)
- [35] R.P. Tiwari, D.Stroud *Model for the magnetoresistance and Hall coefficient of inhomogeneous graphene*, arXiv:cond-mat.mes-hall/0812.1577v1 (2008)
- [36] K. Nagashio, T. Nishimura, K. Kita & A. Toriumi *Mobility variations in mono- and multi-layer graphene films*, arXiv:cond-mat.mes-hall/0812.2107v1 (2008)
- [37] P. Esquinazi, A. Setzer, R. Höhne & C. Semmelhack *Ferromagnetism in oriented graphite samples*, Phys. Rev. B 66, 024429 (2002)
- [38] P.J. Zomer *Spin transport and relaxation in etched graphene strips*, Master Thesis at Physics of Nanodevices Group, Rijksuniversitat Groningen, (2009)
- [39] P. Nemes-Incze, Z. Osvath, K. Kamaras, L.P. Biro *Anomalies in thickness measurements of graphene and few layer graphite crystals by tapping mode atomic force microscopy*, Carbon, vol. 46, no 11, pp 1435-1442 (2008)
- [40] Y.-W. Tan, Y. Zhang, K. Bolotin, Y. Zhao, S. Adam, E.H. Hwang, S. Das Sarma, H.L. Stormer & P. Kim *Measurement of Scattering Rate and Minimum Conductivity in Graphene*, Phys. Rev. Lett. 99, 246803 (2007)
- [41] X. Du, I. Skachko, A. Barker & E.Y. Andrei *Approaching ballistic transport in suspended graphene*, Nature Nanotechnology 3, 491 - 495 (2008)